

DIFFUSION TENSOR MAGNETIC RESONANCE ELECTRICAL IMPEDANCE
TOMOGRAPHY (DT-MREIT) AND ITS EXPANSION TO MULTI-PHYSICS
MULTI-CONTRAST MAGNETIC RESONANCE IMAGING

A THESIS SUBMITTED TO
THE GRADUATE SCHOOL OF NATURAL AND APPLIED SCIENCES
OF
MIDDLE EAST TECHNICAL UNIVERSITY

BY

MEHDI SADIGHI

IN PARTIAL FULFILLMENT OF THE REQUIREMENTS
FOR
THE DEGREE OF DOCTOR OF PHILOSOPHY
IN
ELECTRICAL AND ELECTRONICS ENGINEERING

JUNE 2021

Approval of the thesis:

**DIFFUSION TENSOR MAGNETIC RESONANCE ELECTRICAL
IMPEDANCE TOMOGRAPHY (DT-MREIT) AND ITS EXPANSION TO
MULTI-PHYSICS MULTI-CONTRAST MAGNETIC RESONANCE
IMAGING**

submitted by **MEHDI SADIGHI** in partial fulfillment of the requirements for the degree of **Doctor of Philosophy in Electrical and Electronics Engineering Department, Middle East Technical University** by,

Prof. Dr. Halil Kalipçılar
Dean, Graduate School of **Natural and Applied Sciences** _____

Prof. Dr. İlkay Ulusoy
Head of Department, **Electrical and Electronics Engineering** _____

Prof. Dr. B. Murat Eyüboğlu
Supervisor, **Electrical and Electronics Engineering, METU** _____

Examining Committee Members:

Prof. Dr. Nevzat Güneri Gençer
Electrical and Electronics Engineering, METU _____

Prof. Dr. B. Murat Eyüboğlu
Electrical and Electronics Engineering, METU _____

Assoc. Prof. Dr. Sevinç Figen Öktem
Electrical and Electronics Engineering, METU _____

Prof. Dr. Ergin Atalar
Electrical and Electronics Engineering, Bilkent University _____

Assist. Prof. Dr. Evren Değirmenci
Electrical and Electronics Engineering, Mersin University _____

Date: 01.06.2021

I hereby declare that all information in this document has been obtained and presented in accordance with academic rules and ethical conduct. I also declare that, as required by these rules and conduct, I have fully cited and referenced all material and results that are not original to this work.

Name, Surname: Mehdi Sadighi

Signature :

ABSTRACT

DIFFUSION TENSOR MAGNETIC RESONANCE ELECTRICAL IMPEDANCE TOMOGRAPHY (DT-MREIT) AND ITS EXPANSION TO MULTI-PHYSICS MULTI-CONTRAST MAGNETIC RESONANCE IMAGING

Sadighi, Mehdi

Ph.D., Department of Electrical and Electronics Engineering

Supervisor: Prof. Dr. B. Murat Eyüboğlu

June 2021, 135 pages

Diffusion tensor magnetic resonance electrical impedance tomography (DT-MREIT) is one of the emerging imaging modalities to obtain low-frequency anisotropic conductivity distribution employing diffusion tensor imaging (DTI) and magnetic resonance electrical impedance tomography (MREIT) techniques. DT-MREIT is based on the linear relationship between the conductivity and water self-diffusion tensors ($\overline{\overline{C}}$ and $\overline{\overline{D}}$) in a porous medium.

On the other hand, knowledge of the current density ($\overline{\overline{J}}$) distribution is used in many medical applications to optimize and plan treatments like transcranial direct and alternating current stimulations (tDCS and tACS) and deep brain stimulation (DBS). Magnetic resonance current density imaging (MRCDI) is used to acquire cross-sectional current-induced magnetic flux density (B_z) and $\overline{\overline{J}}$ distributions of the externally injected currents. The clinical applicability of DT-MREIT and MRCDI is highly dependent on the sensitivity of the acquired noisy B_z (\tilde{B}_z) and the estimated $\overline{\overline{J}}$ distributions.

In this thesis, a novel pulse sequence, namely the injected current nonlinear encoding -multi-echo-FLASH (ICNE-ME-FLASH), is implemented for MRCDI to acquire qualified (high SNR) \tilde{B}_z and \bar{J} distributions in a clinically acceptable scan time. Also, an analysis is developed to investigate the combined effect of relevant sequence parameters on the SNR level and the total acquisition time of the acquired \tilde{B}_z images. The minimum total acquisition time for the desired SNR level or the highest SNR achievable in a given time can be estimated using the proposed analysis. Also, the analysis provides different sets of sequence parameters (i.e., T_R , N_{EX} , α) to achieve the desired SNR level in almost the same acquisition time that can be used in different experimental situations. Using the proposed ICNE-ME-FLASH pulse sequence, the \tilde{B}_z distributions with the estimated SNR of 13 dB associated with $I = 200$ and $400 \mu\text{A}$ current injection can be measured in the total scan time less than 19 and 5 minutes, respectively. Also, the effects of magnetohydrodynamic (MHD) flow velocity (\bar{v}) and the intensive utilization of the gradients in the MRCDI experiments using ICNE-ME-FLASH are investigated for the first time.

A novel reconstruction algorithm is devised for DT-MREIT to reconstruct the conductivity tensor images using a single current injection. Therefore, the clinical applicability of DT-MREIT can be improved by reducing the total acquisition time, the number of current injection cables, and contact electrodes to half by decreasing the number of current injection patterns to one. The conductivity tensor distributions of two imaging phantoms with $I = 3 \text{ mA}$ current injection are reconstructed using the proposed single current DT-MREIT. The total data acquisition time for DTI and \tilde{B}_z imaging is 21 and 30 minutes. The same MRCDI procedure with two current injections lasts twice as much. The SNR of the measured \tilde{B}_z using ICNE-ME-FLASH pulse sequence is estimated as 36 dB and 32 dB for the two phantoms.

Furthermore, a multi-physics multi-contrast pulse sequence is proposed and implemented to acquire \bar{D} , \tilde{B}_z and \bar{v} data simultaneously instead of acquiring these multiple data individually using three different pulse sequences.

The proposed pulse sequences, the SNR and total acquisition time analysis, and the reconstruction algorithms are evaluated using simulated measurements and physical experiments. All these improvements and the proposed methods could increase the

clinical potential of the current density and conductivity tensor imaging.

Keywords: current density imaging, conductivity tensor imaging, SNR analysis, multi contrast imaging, reconstruction algorithm, FLASH, pulse sequence parameter optimization

ÖZ

DİFÜZYON TENSÖRÜ MANYETİK REZONANS ELEKTRİKSEL EMPEDANS TOMOGRAFİSİ (DT-MREET) VE ÇOK FİZİKLİ ÇOK KONTRASTLI MANYETİK REZONANS GÖRÜNTÜLEMESİNE GENİŞLETMESİ

Sadighi, Mehdi

Doktora, Elektrik ve Elektronik Mühendisliği Bölümü

Tez Yöneticisi: Prof. Dr. B. Murat Eyüboğlu

Haziran 2021 , 135 sayfa

Difüzyon tensörü manyetik rezonans elektriksel empedans tomografisi (DT-MREET), difüzyon tensör görüntüleme (DTG) ve manyetik rezonans elektriksel empedans tomografisi (MREET) tekniklerini kullanarak düşük frekanslı yön bağımlı iletkenlik dağılımı elde etmek için önerilen yeni görüntüleme yöntemlerinden biridir. DT-MREET, gözenekli bir ortamda iletkenlik ve su kendinden difüzyon tensörleri (\overline{C} ve \overline{D}) arasındaki doğrusal ilişkiye dayanır. Öte yandan, akım yoğunluğu dağılımı (\overline{J}) bilgisi, transkraniyal doğru ve alternatif akım stimülasyonları (tDAS ve tAAS) ve derin beyin stimülasyonu (DBS) gibi birçok tıbbi uygulamada tedavileri optimize etmek ve planlamak için kullanılır. Manyetik rezonans akım yoğunluğu görüntüleme (MRAYG), harici olarak uygulanan akımlar tarafından indüklenen kesitsel manyetik akı yoğunluğu (B_z) ve \overline{J} dağılımlarını elde etmek için kullanılır. DT-MREET ve MRAYG'nin klinik uygulanabilirliği, büyük ölçüde elde edilen gürültülü B_z (\tilde{B}_z) ve tahmini \overline{J} dağılımlarının hassasiyetine bağlıdır.

Bu tezde, MRAYG ile klinik olarak kabul edilebilir bir görüntüleme süresinde, nitelikli (yüksek SGO seviyesine sahip) \tilde{B}_z ve \bar{J} dağılımları elde etmek için uygulanan akım doğrusal olmayan kodlama-çoklu eko-FLASH (ICNE-ME-FLASH) adlı yeni bir darbe dizisi kullanılmıştır. Ayrıca, ilgili darbe dizisi parametrelerinin elde edilen \tilde{B}_z görüntülerinin SGO seviyesi ve toplam görüntüleme süresi üzerindeki birleşik etkisini araştırmak için bir analiz geliştirilmiştir. İstenen SGO seviyesi için minimum toplam görüntüleme süresi veya belirli bir zamanda ulaşılabilen en yüksek SGO seviyesi, önerilen analiz kullanılarak tahmin edilebilir. Ayrıca yapılan analiz, farklı deneysel durumlarda kullanılacak, istenen SGO seviyesini yaklaşık aynı görüntüleme süresinde sağlayan farklı dizi parametre setleri (T_R , N_{EX} , α) elde etmekte kullanılabilir. Önerilen ICNE-ME-FLASH darbe dizisini kullanarak, $I = 200$ ve $400 \mu A$ akım uygulaması ile 13 dB tahmini SGO'ya sahip \tilde{B}_z dağılımları, sırasıyla, 19 ve 5 dakikadan daha kısa toplam görüntüleme süresinde ölçülebilir.

Ayrıca, ICNE-ME-FLASH kullanılarak yapılan MRAYG deneylerinde manyetohidrodinamik (MHD) akış hızının (\bar{v}) ve gradyanların yoğun kullanımının etkileri ilk kez araştırılmıştır.

DT-MREET ile tek bir yönde akım uygulaması ile iletkenlik tensör görüntülerini geri çözmek amacıyla yeni bir geri çözüme algoritması tasarlanmıştır. Akım uygulama yönlerinin sayısının bire düşmesi ile toplam görüntüleme süresinin, akım uygulama kablolarının ve kontak elektrotlarının sayılarının da yarıya inmesi sayesinde DT-MREET'nin klinik uygulanabilirliği artırılmıştır. $I = 3$ mA akım uygulaması ile iki görüntüleme fantomunun iletkenlik tensör dağılımları, önerilen tek akımlı DT-MREET metodu kullanılarak geri çözülmüştür. DTG ve \tilde{B}_z görüntüleme için toplam görüntüleme süreleri 21 ve 30 dakikadır. İki akım uygulaması ile aynı MRAYG prosedürü iki kat daha uzun sürer. ICNE-ME-FLASH darbe dizisi kullanılarak ölçülen \tilde{B}_z dağılımlarının SGO seviyesi, iki fantom için 36 dB ve 32 dB olarak tahmin edilmiştir. Ayrıca, üç farklı darbe dizisi kullanarak bu çoklu verileri ayrı ayrı elde etmek yerine \bar{D} , \tilde{B}_z ve \bar{v} verilerini aynı anda elde etmek için bir çoklu fizik çoklu kontrast darbe dizisi önerilmiş ve uygulanmıştır. Önerilen darbe dizileri, SGO ve toplam görüntüleme süresi analizi ve geri çözüme algoritmaları, simüle edilmiş ölçümler ve fiziksel deneyler kullanılarak değerlendirilmiştir. Tüm bu gelişmeler ve önerilen yöntemler, klinik uygulamada akım yoğunluğu ve iletkenlik tensör görüntüleme yöntemlerinin

rutin kullanımının önünü açma potansiyeline sahiptir.

Anahtar Kelimeler: akım yoğunluğu görüntüleme, iletkenlik tensör görüntüleme, SGO analizi, çoklu kontrast görüntüleme, geri çatma algoritması, FLASH, darbe dizisi parametre optimizasyonu

If you have knowledge, let others light their candles with it.

"Margaret Fuller"

ACKNOWLEDGMENTS

I would like to express my sincerest gratitude to my supervisor, Prof. Dr. B. Murat Eyübođlu, for his continuous support, guidance, patience, and contributions throughout my graduate education and thesis study.

I express my gratitude to Thesis Monitoring Committee (TMC) members, Prof. Dr. Ergin Atalar and Assoc. Prof. Dr. Sevinç Figen Öktem for their valuable comments and recommendations during my thesis study.

I express my gratitude to Prof. Dr. Nevzat Güneri Gençer and Assist. Prof. Dr. Evren Deđirmenci for their attendance on my thesis defense committee and for evaluating my thesis.

I express my gratitude to my colleague Mert Şişman, for his continuous support, friendship, and help in the last two years of my thesis study. Thanks to his invaluable help and support, this thesis achieved all its objectives.

I express my gratitude to Dr. Hasan Hüseyin Erođlu for his contributions by designing and implementing the MR-compatible current source for experimental data acquisition and joining the experiments in the early stage of this thesis study.

I wish to express my gratitude to Assist. Prof. Dr. Evren Deđirmenci for his valuable support, friendship, and kindness during my graduate studies.

I express my gratitude to administrative staff and lab members of National Magnetic Resonance Research Center (UMRAM) for their understanding and help during this thesis study. The experimental data were acquired using the facilities of UMRAM, Bilkent University, Ankara, Turkey.

I would like to express my gratitude to The Scientific and Technological Research Council of Turkey (TÜBİTAK) for funding this study partially under the Research Grant 116E157. I have been supported as a scholarship researcher in Research Grant

116E157 between the years 2017-2020. Also, I am truly grateful to be granted as a scholarship researcher between the years 2014-2016 under the research grant 113E979.

Finally, my deep and sincere gratitude to my family for their continuous and unparalleled love, help, and support. I am grateful to my sister for always being there for me as a friend. I am forever indebted to my parents for giving me the opportunities and experiences that have made me who I am.

TABLE OF CONTENTS

ABSTRACT	v
ÖZ	viii
ACKNOWLEDGMENTS	xii
TABLE OF CONTENTS	xiv
LIST OF TABLES	xviii
LIST OF FIGURES	xx
LIST OF ABBREVIATIONS	xxix
CHAPTERS	
1 INTRODUCTION	1
1.1 Motivation	1
1.2 Current Density Imaging	3
1.3 Diffusion Tensor Imaging	5
1.4 Electrical Conductivity Imaging	11
1.4.1 Magnetic Resonance Electrical Impedance Tomography	11
1.4.2 Magnetic Resonance Conductivity Tensor Imaging	13
1.4.3 Diffusion Tensor - Magnetic Resonance Electrical Impedance Tomography	13
1.5 Multi-Physics Multi-Contrast Magnetic Resonance Imaging	16

1.6	The Outline of the Thesis	16
2	THEORY AND THE MATHEMATICAL DERIVATIONS OF THE PROPOSED PULSE SEQUENCES AND THE RECONSTRUCTION ALGORITHMS FOR MRCDI, DT-MREIT, AND MULTI-CONTRAST IMAGING	19
2.1	SNR Analysis of the Acquired \tilde{B}_z	19
2.1.1	Spoiled Gradient Echo Pulse Sequences	20
2.1.2	SNR Analysis of the Acquired \tilde{B}_z Using ICNE-FLASH Pulse Sequence	21
2.1.3	SNR Analysis of the Measured Multiple \tilde{B}_z Using ICNE-ME-FLASH Pulse Sequence	23
2.1.4	Noise Estimation of the Measured \tilde{B}_z	25
2.1.5	Effect of Intensive Utilization of Gradients on the Measured \tilde{B}_z	26
2.1.6	Effects of the B_0 and BW on SNR of the Measured \tilde{B}_z	28
2.1.6.1	Readout (frequency encoding) Bandwidth	29
2.1.6.2	Phase Encoding Bandwidth	30
2.1.7	Imaging Phantom for Experimental Evaluation of the Proposed SNR and Total Acquisition Time Analysis of ICNE-ME-FLASH	30
2.2	Reconstruction of the Projected Current Density Distribution (\bar{J}_p) from the Measured \tilde{B}_z	31
2.3	Diffusion Tensor Imaging	32
2.3.1	Geometric Distortion of the DW Images Acquired Using SS-SE-EPI Pulse Sequence and the Correction Methods	34
2.4	The Proposed Reconstruction Algorithms for Diffusion Tensor-Magnetic Resonance Electrical Impedance Tomography	35
2.4.1	A single current injection pattern	37
2.4.2	Two current injection patterns	39
2.4.3	Adaptive regularization based on the current density distribution	40

2.4.4	The Simulation Model for the Numerical Evaluation of the Proposed Dual and Single Current DT-MREIT	41
2.4.5	Imaging Phantoms and Pulse Sequence Parameters for Experimental Evaluation of the Proposed Dual and Single Current DT-MREIT	41
2.5	MHD Flow Imaging	46
2.6	The Proposed Multi-Contrast Imaging Pulse Sequence	49
2.6.1	Imaging Phantom and Pulse Sequence Parameters for Experimental Evaluation of the Proposed Multi-Contrast Imaging	51
3	THE RESULTS OF THE PROPOSED METHODS USING ANALYTICAL MODELINGS, NUMERICAL SIMULATIONS AND PHANTOM EXPERIMENTS	53
3.1	SNR and the Total Data Acquisition Time Analysis of the measured \tilde{B}_z	53
3.1.1	The Analytical Modeling Results	54
3.1.1.1	The Analytical Modelling Results for ICNE-FLASH Pulse Sequence	54
3.1.1.2	The Analytical Modelling Results for ICNE-ME-FLASH Pulse Sequence	58
3.1.2	Experimental Results of the ICNE-ME-FLASH Pulse Sequence	60
3.1.2.1	The Current-Induced \tilde{B}_z Imaging	60
3.1.3	The Effect of Intensive Utilization of Gradients on the Measured \tilde{B}_z	63
3.1.4	The Effect of MHD Flow on the Acquired \tilde{B}_z images in MRCDI	64
3.2	The Results of the Proposed Dual and Single Current DT-MREIT	67
3.2.1	Results of Simulation Model	68
3.2.1.1	Noise-Free Simulation	68
3.2.1.2	Noise Analysis	69

3.2.2	Practical Realization of DT-MREIT by Using Experimental Measurements	73
3.2.2.1	DTI of the Experimental Phantoms	73
3.2.2.2	CDI of the Experimental Phantoms	74
3.2.2.3	Conductivity Tensor Reconstruction of the Ph 1	77
3.2.2.4	Conductivity Tensor Reconstruction of the Ph 2	80
3.3	The Experimental Results of the Multi-Contrast Imaging Pulse Sequence	83
3.3.1	Multi-Contrast Data Acquisition of the Experimental Phantom	83
3.3.1.1	The Reconstructed Diffusion Tensor Distribution	83
3.3.1.2	The Measured MHD Flow Velocity Distribution	86
3.3.1.3	Current-Induced \tilde{B}_z and the Estimated Current Density Distributions	86
3.3.1.4	The Reconstructed Conductivity Tensor Distribution	89
4	DISCUSSIONS OF THE RESULTS	91
4.1	SNR and Total Scan Time Analysis of the ICNE-ME-FLASH Pulse Sequence	91
4.2	The Dual and a Single Current DT-MREIT Methods	97
4.3	Multi Physics Multi-Contrast Imaging	103
5	CONCLUSION	109
	REFERENCES	113
	CURRICULUM VITAE	131

LIST OF TABLES

TABLES

Table 2.1 ICNE-ME-FLASH pulse sequence parameters.	32
Table 2.2 Parameters of the FE model in the background and in the left and right inhomogeneities. σ_{xx} , σ_{yy} , σ_{zz} and d_{xx} , d_{yy} , d_{zz} are the main diagonal components of $\overline{\overline{C}}$ and $\overline{\overline{D}}$, respectively.	43
Table 2.3 SS-SE-EPI pulse sequence parameters for DTI data acquisition of the Ph 1 and Ph 2.	46
Table 2.4 ICNE-ME-FLASH pulse sequence parameters for MRCDI data acquisition of the Ph 1 and Ph 2.	47
Table 2.5 Multi-contrast imaging pulse sequence parameters.	52
Table 3.1 The approximate relaxation times and the proton density for several biological tissues at 3 T.	54
Table 3.2 The estimated noise standard deviation of the measured \tilde{B}_z^4 ($s_{\tilde{n}^4}$) ($T_C^4 = T_2^* = 50$ ms), the estimated $s_{\tilde{n}_w}$ and the T_{Total} (for $N_{PE} = 64$) of the parameter sets in Figure 3.2.	62
Table 3.3 The mean values of the reconstructed ECDR distributions in different regions of the simulations model using dual and a single current methods for noiseless case. The true values of the ECDR distribution is 1 S s mm^{-3} and 2 S s mm^{-3} for the background and the inhomogeneities, respectively.	71

Table 3.4 The mean values of the reconstructed σ_{xx} , σ_{yy} and σ_{zz} in different regions of Ph 1 for dual, vertical and horizontal current injections. The $\overline{\overline{C}}$ distributions are reconstructed using the proposed methods in (2.66) and (2.68) for a single and dual current injections. The AR for the left and right muscle pieces are calculated as $\frac{\sigma_{xx}}{\sigma_{yy}}$ and $\frac{\sigma_{yy}}{\sigma_{xx}}$, respectively. 79

Table 3.5 The mean values of the reconstructed $\overline{\overline{C}}$ (σ_{xx} , σ_{yy} and σ_{zz}) in different regions of Ph 2 for dual, vertical and horizontal current injections. The $\overline{\overline{C}}$ distributions are reconstructed using the proposed methods in (2.66) and (2.68) for a single and dual current injection DT-MREIT methods. The AR of the muscle piece is calculated as the ratio of conductivity in the direction parallel to the muscle fibers and the conductivity in the perpendicular direction ($\frac{\sigma_{xx}}{\sigma_{yy}}$). 82

Table 3.6 The mean values of the reconstructed $\overline{\overline{D}}$ and $\overline{\overline{C}}$ in different regions of the experimental phantom in Figure 2.9 using the proposed multi-contrast imaging method. 90

LIST OF FIGURES

FIGURES

<p>Figure 1.1 Diagram of the ICNE-ME-FLASH pulse sequence. G_z, G_p and G_f are the slice selection, phase encoding, and frequency encoding gradients, respectively. Two k-space data sets $S^\pm(k_x, k_y)$ for each echo are acquired by injecting current with opposite polarities (I^\pm) to remove the systematic phase artifacts from the acquired phase images. Φ_n is the phase of the RF excitation pulse.</p>	5
<p>Figure 1.2 Diagram of a diffusion-weighted SE pulse sequence. A pair of diffusion gradients straddling the RF refocusing pulse. δ is the time between the first rise of the trapezoidal gradient pulse and the end of its plateau, and ε is the rise time of the pulse. Δ is the time between the starting points of the first and second diffusion encoding gradient pulses. G_z, G_p and G_f are the slice selection, phase encoding, and frequency encoding gradients, respectively.</p>	7
<p>Figure 1.3 Representation of DT in a voxel as an ellipsoid with three orthogonal unit eigenvectors $\bar{e}_1, \bar{e}_2, \bar{e}_3$ and the corresponding lengths (eigenvalues) $\lambda_1, \lambda_2, \lambda_3$.</p>	10
<p>Figure 2.1 (a) The photograph of the experimental phantom and its (b) Transversal (x-y) plane. The phantom is filled with a saline solution with 2.75 g/L of NaCl and 0.034 g/L of $MnCl_2$ dissolved in pure water to mimic the mean conductivity and relaxation times of the human brain WM.</p>	31

Figure 2.2 Diagram of a DW SS-SE-EPI pulse sequence. Diffusion encoding gradients can be applied in the three orthogonal directions. G_z , G_p and G_f are the slice selection, phase encoding, and frequency encoding gradients, respectively. The diffusion can be imaged in any arbitrary direction by changing the relative components throughout the three orthogonal gradient directions. 33

Figure 2.3 (a) The cubic FE model, and (b) its mesh structure. The FE model is composed of a cube with the dimensions of $80 \times 80 \times 80 \text{ mm}^3$ and four recessed structures, each with the dimensions of $20 \times 20 \times 20 \text{ mm}^3$ for placement of the current injection electrodes. Two inhomogeneities with the dimensions of $20 \times 20 \times 20 \text{ mm}^3$ are placed at the middle slice of the model. The FE model is composed of 122838 domain, 7772 boundary, and 583 edge elements, and it is solved for 965805 degrees of freedom. 42

Figure 2.4 The true ECDR distribution in the mid-slice of the simulation model in Figure 2.3 considering the \overline{C} and \overline{D} values in Table 2.2. 42

Figure 2.5 Ph 1 is filled with a saline solution and two chicken breast pieces are placed inside the phantom with the help of the holder apparatus to mimic anisotropy. (a) The imaging slice in the transversal (x-y) plane. The red and green arrows show the patterns of the injected currents. (b) The colored FA map of the imaging slice is obtained from the DT images of the experimental phantom. The red and green colors show that the main direction of diffusion for the left and right muscle pieces is in the x- and y- directions, respectively. (c) MD of the imaging slice. The relaxation parameters of the chicken muscle pieces measured as: $T_1 = 1200 \text{ ms}$ and $T_2^* = 20 \text{ ms}$ 44

Figure 2.6 Ph 2 filled with a saline solution and a piece of bovine muscle is placed inside the container to mimic anisotropy. The red mesh structure is used to hold the muscle piece in the center of phantom. (a) The imaging slice in the transversal (x-y) plane. (b) Top view (x-z plane). (c) The colored FA map of the imaging slice. The red color shows that the main direction of diffusion (muscle fibers) is in the x- direction. (d) The MD of the imaging slice. The relaxation parameters of the muscle piece measured as: $T_1 = 1412$ ms and $T_2^* = 37$ ms. 45

Figure 2.7 The FE model of the experimental phantom with the dimensions of $80 \times 80 \times 80$ and four recessed structures with the dimensions of $20 \times 20 \times 20$. The FE model is composed of 10906 tetrahedral, 3472 prism, 1624 triangular, and 240 edge elements. The open boundary condition is applied for the phantom’s top surface, and the no-slip boundary condition is applied for the remaining surfaces. The laminar flow model is solved for a maximum step size of 1 ms. 48

Figure 2.8 The schematic diagram of the DW-SE multi-contrast pulse sequence with simultaneous current injection. g_d ’s are the magnitudes of the diffusion encoding gradients. I and T_C are the amplitude and the duration of the injected current, respectively. Δ , δ and ε are defined in Section 1.3. G_z , G_p and G_f are the slice selection, phase encoding, and frequency encoding gradients, respectively. 49

Figure 2.9 The experimental phantom for multi-contrast data acquisition filled with a saline solution and two pieces of bovine muscle are placed inside the saline solution with the help of a holder apparatus to mimic anisotropy. 52

Figure 3.1 Contour plot of the calculated $\xi_{\bar{B}_z}$ for different T_R and α values of ICNE-FLASH pulse sequence considering the relaxation parameters of the WM and $T_C = T_2^*$ 55

Figure 3.2 Different sets of T_R , N_{EX} and α to acquire \tilde{B}_z images with the SNR level of (a) $\xi_{\tilde{B}_z^{max}}$ ($K = 1$), (b) $0.5\xi_{\tilde{B}_z^{max}}$ ($K = 0.5$), (c) $2\xi_{\tilde{B}_z^{max}}$ ($K = 2$) using ICNE-FLASH pulse sequence. The regions inside the dashed lines have almost the same total acquisition time per each phase encoding step T_{Total}/N_{PE} . $T_C = T_2^* = 50$ ms to maximize the SNR level of the acquired \tilde{B}_z and the condition $T_R \geq T_C$ holds for all calculations. The green region in (b) shows the parameter sets with $T_R < T_C$. The points (I) – (VII) are used in experimental data acquisition for $K = 0.5, 1, 2$ 56

Figure 3.3 (a) T_{Total}/N_{PE} versus N_{EX} for different K values. (b) The α_t versus N_{EX} for $K = 0.5, 1, 2$. Each α_t gives the flip angle providing the shortest T_{Total} to achieve $K\xi_{\tilde{B}_z^{max}}$ for a specific N_{EX} . (c) The minimum total time per phase encoding ($\min T_{Total}/N_{PE}$) versus K for three different N_{EX}^{max} 57

Figure 3.4 Flowcharts of the proposed parameter search algorithms. (a) The algorithm that finds the minimum data acquisition time T_{min} with optimal parameters α^{opt} , N_{EX}^{opt} and T_R^{opt} . (b) The algorithm that finds the suboptimal data acquisition time T_{sub} with suboptimal parameters α^{sub} , N_{EX}^{sub} and T_R^{sub} . Both parameter sets (optimal and suboptimal) will provide the same SNR level, determined by the chosen K value. However, the data acquisition time provided by the optimal parameter set will be lower than the suboptimal parameter set with an amount depending on the chosen margin. 59

Figure 3.5 Relative $s_{\tilde{n}_w}$ of the \tilde{B}_z^{comb} for $N_E = 6, 9, 12$ and a range of T_C , where $\Delta T = 5.3$ ms, $T_2^* = 50$ ms and $f(\rho_0, \alpha, T_R) = 1$ in (2.22). $s_{\tilde{n}_w}$ is minimized when $T_C = 65, 75$ and 86 ms for $N_E = 6, 9$ and 12 , respectively. 60

Figure 3.6 The $s_{\tilde{n}_i}$ of the ICNE-ME-FLASH pulse sequence for the parameter sets (a) (I) – (III) ($K = 1$), and (b) (IV) – (VI) ($K = 0.5$) of Figure 3.2. 61

Figure 3.7	The calculated \tilde{B}_z^{comb} distributions of the imaging phantom using ICNE-ME-FLASH pulse sequence with parameter sets $T_R(\text{ms})/N_{EX}/\alpha$: (a) 555/4/53 ($K = 1$) (b) 272/2/40 ($K = 0.5$) and (c) 590/15/55 ($K = 2$). The $s_{\tilde{n}_w} \approx 0.42, 0.85,$ and, 0.20 nT for (a), (b) and (c), respectively.	62
Figure 3.8	(a) The estimated noise distribution of $N = 50$ acquisitions of the ninth (last) echo, $D_i^9(x, y)$. The unit of the noise (x-axis) is nT. (b) The estimated $s_{\tilde{n}^9}$ of $N = 50$ acquisitions (blue stars) and their mean value ($\hat{s}_{\tilde{n}^9}$) (red line)	65
Figure 3.9	(a) The estimated noise means of the acquired \tilde{B}_z^j and (b) the calculated ΔB_0 for $N = 50$ acquisitions of the entire nine echoes. . . .	66
Figure 3.10	(a) The estimated $D_i^9(x, y)$ distributions for $N = 50$ acquisitions after ΔB_0 cancellation.	66
Figure 3.11	The simulated \bar{v} distributions in the x- and y- directions v_x and v_y for $T_R(\text{ms}) = 86, 155$ and 555 . (a)-(c) v_x and (d)-(f) v_y distributions, respectively.	67
Figure 3.12	(a) The B_z distribution of the FE model for $I = 2$ mA current injection. The calculated $\varepsilon_{MHD B_z}$ distributions due MHD flow velocity \bar{v} for T_R (ms) (b) 86, (c) 155, and (d) 555.	68
Figure 3.13	The simulated B_z distribution of the vertical current injection, B_{z_V} , and the corresponding (b) J_{px_V} and (c) J_{py_V} . (d) The simulated B_z distribution of the horizontal current injection, B_{z_H} , and the corresponding (e) J_{px_H} and (f) J_{py_H} distributions.	69
Figure 3.14	(a-d) The reconstructed ECDR for different SNR levels using the method proposed in [73] for dual current injection patterns. The reconstructed ECDR using the proposed methods with (e-h) dual current and a single current injection (i-l) vertical and (m-p) horizontal for different SNR levels.	70

Figure 3.15	The RMSE values of the reconstructed $\overline{\overline{C}}$ for different SNR levels in different regions of the simulation model using the proposed method with dual current injections: (a) left inhomogeneity, (b) right inhomogeneity, and (c) background, with vertical current injection: (d) left inhomogeneity, (e) right inhomogeneity and (f) background and horizontal current injection: (g) left inhomogeneity, (h) right inhomogeneity and (i) background.	72
Figure 3.16	\tilde{B}_z^{comb} and \overline{J}_p distributions of the experimental Ph 1. (a) \tilde{B}_z^{comb} for vertical current injection, \tilde{B}_{zV}^{comb} , and the corresponding estimated (b) J_{pxV} and (c) J_{pyV} . (d) \tilde{B}_{zH}^{comb} and the corresponding estimated (e) J_{pxH} and (f) J_{pyH} distributions.	74
Figure 3.17	\tilde{B}_z^{comb} and \overline{J}_p distributions of the experimental Ph 2. (a) \tilde{B}_z^{comb} and the corresponding (b) J_{pxV} and (c) J_{pyV} . (d) \tilde{B}_{zH}^{comb} and the corresponding (e) J_{pxH} and (f) J_{pyH} distributions.	75
Figure 3.18	The reconstructed ECDR distributions of Ph1 using the proposed method with (a) dual, (b) vertical, and (c) horizontal current injection patterns.	77
Figure 3.19	The diagonal components of the reconstructed $\overline{\overline{C}}$ (σ_{xx} , σ_{yy} and σ_{zz}) of the experimental phantom Ph 1 using the proposed method with (a-c) dual, (d-f) vertical and (g-i) horizontal current injections. The effect of overestimation of ECDR distribution is barely visible in the reconstructed σ_{xx} , σ_{yy} and σ_{zz} of the horizontal current injection.	78
Figure 3.20	The ellipsoid plot of the reconstructed $\overline{\overline{C}}$ distribution of Ph 1. The conductivity of the left and right muscle pieces are higher in the x- and y- directions, respectively. Due to a low amount of AR in both muscle pieces the ellipsoids have more spheroidal shape than the elliptical, as shown in the magnified regions of the left and right muscle pieces. The background with isotropic isotropic distribution is presented using white ellipsoids. The main direction of conductivity at each voxel can be determined using the given color map.	79

Figure 3.21 The reconstructed ECDR distribution of Ph 2 using the method with (a) dual (η_{Dual}) and single: (b) vertical (η_{Vertical}), and (c) horizontal ($\eta_{\text{Horizontal}}$) current injection patterns. The effect of ECDR overestimation is barely visible in the regions near to the current injection electrodes in the reconstructed η_{Vertical} and $\eta_{\text{Horizontal}}$ 80

Figure 3.22 The diagonal components of the reconstructed $\overline{\overline{C}}$ (σ_{xx} , σ_{yy} and σ_{zz}) of the experimental phantom Ph 2 using the proposed DT-MREIT method with (a)-(c): Dual, (d)-(f): vertical, and (g)-(i): horizontal current injections. 81

Figure 3.23 The ellipsoid plot of the reconstructed $\overline{\overline{C}}$ distribution of Ph 2. The conductivity of the muscle piece is higher in the x- direction than the other two perpendicular directions. A higher anisotropy in the bovine muscle piece cause more prolated ellipsoids. Two regions of the muscle with the high and relatively low AR are magnified in the left and right side of the figure, respectively. The background with isotropic distribution is presented using white spheres. The main direction of conductivity at each voxel can be determined using the given color map. 82

Figure 3.24 The reconstructed $\overline{\overline{D}}$ of the experimental phantom without current injection: (a) d_{xx} , (b) d_{yy} , (c) d_{zz} ; with vertical current injection (I_{V}^+): (d) d_{xx} , (e) d_{yy} , (f) d_{zz} ; with horizontal current injection (I_{H}^+): (g) d_{xx} , (h) d_{yy} , (i) d_{zz} . Minor artifacts nearside the muscle pieces in the diffusion tensor distributions obtained with I_{V}^+ are indicated with red circles. 85

Figure 3.25 The coloured FA map of the experimental phantom calculated from the reconstructed $\overline{\overline{D}}$ for no current case. The red and blue colours in the left and right muscle pieces show that the diffusion is higher in the x- and z-directions, respectively. 86

Figure 3.26 The MHD flow velocity distributions of the experimental phantom with the vertical current injection (\bar{v}_V): (a) v_{xV} , (b) v_{yV} , (c) v_{zV} . The MHD flow velocity distributions of the experimental phantom with the horizontal current injection (\bar{v}_H): (d) v_{xH} , (e) v_{yH} , (f) v_{zH} 87

Figure 3.27 2D arrow plot of the reconstructed MHD flow velocity, \bar{v} , distribution for the vertical and the horizontal current injection patterns. (a) \bar{v}_V (b) \bar{v}_H 87

Figure 3.28 (a) The measured \tilde{B}_z distribution of the experimental phantom for vertical current injection in synchrony with the proposed pulse sequence, \tilde{B}_{zV} , and the corresponding estimated (b) J_{pxV} and (c) J_{pyV} . (d) The measured \tilde{B}_z distribution for horizontal current injection, \tilde{B}_{zH} , and the corresponding estimated (e) J_{pxH} (f) J_{pyH} 88

Figure 3.29 2D arrow plot of the estimated \bar{J}_p for the vertical and the horizontal current injection patterns. (a) \bar{J}_{pV} (b) \bar{J}_{pH} 88

Figure 3.30 (a) The reconstructed ECDR distribution using the proposed dual current DT-MREIT in (2.68). The diagonal components of the reconstructed $\bar{\bar{C}}$ (b) σ_{xx} , (c) σ_{yy} and (d) σ_{zz} of the experimental phantom. 89

Figure 4.1 Equi-magnetic field contours of the simulated \hat{B}_z of the FE model in Figure 2.7. The conductivity of the liquid material filled in the model is $\sigma = 0.35 \text{ S m}^{-1}$ similar to the experimental phantom in Figure 2.1. $I = 2 \text{ mA}$ current is injected in the horizontal direction. The number on each contour line show the amplitude of the \hat{B}_z in nT. 94

Figure 4.2 (a) The percentage area of the \hat{B}_z distribution below the estimated noise level ($\hat{B}_z \leq s_{\tilde{n}_w}$) for $K = 0.5, 1, 2$ and $I = 0.1 - 2 \text{ mA}$ interval. (b) $|\hat{B}_z|$ distribution of $I = 0.2 \text{ mA}$ current injection (mesh plot) and the estimated $s_{\tilde{n}_w}$ for $K = 2$ (red plane). 95

Figure 4.3 (a) The true $\|\nabla\eta\|$ distribution of the simulated ECDR in Figure 2.4. The $\|\nabla\eta\|$ distribution of the reconstructed ECDR using the proposed DT-MREIT method with (b) dual, (c) vertical, and (d) horizontal current injection patterns. 98

Figure 4.4 The schematic diagram of the multi-contrast imaging pulse sequence with a dual current injection scheme. g_d 's are the magnitudes of the diffusion encoding gradients. I and T_C are the amplitude and the duration of the injected current, respectively. Δ , δ and ε are defined in Section 1.3. G_z , G_p and G_f are the slice selection, phase encoding, and frequency encoding gradients, respectively. 107

Figure 4.5 The schematic diagram of the EPI based multi-contrast imaging pulse sequence. 108

LIST OF ABBREVIATIONS

2D	2 Dimensional
3D	3 Dimensional
ADC	Apparent Diffusion Coefficient
BW	Band Width
BVP	Boundary Value Problem
CDI	Current Density Imaging
CTI	Conductivity Tensor Imaging
CSF	Cerebrospinal Fluid
DBS	Deep Brain Stimulation
DT	Diffusion Tensor
DTI	Diffusion Tensor Imaging
DW	Diffusion Weighted
ECDR	Extra-cellular Conductivity and Diffusivity Ratio
ECG	Electrocardiogram
EPI	Echo Planar Imaging
FA	Fractional Anisotropy
FE	Finite Element
FLASH	Fast Low Angle Shot
FOV	Field of View
GE	Gradient Echo
GM	Gray Matter
ICNE	Injection Current Nonlinear Encoding
i.i.d.	Independent and Identically Distributed
MD	Mean Diffusivity

MHD	Magnetohydrodynamic
MRCDI	Magnetic Resonance Current Density Imaging
MRCTI	Magnetic Resonance Conductivity Tensor Imaging
MREIT	Magnetic Resonance Electrical Impedance Tomography
MREPT	Magnetic Resonance Electrical Property Imaging
RF	Radio Frequency
RMS	Root Mean Square
RMSE	Root Mean Square Error
SE	Spin Echo
SMF	Stray Magnetic Field
SNR	Signal to Noise Ratio
SPGE	Spoiled Gradient Echo
SPMGE	Spoiled Multi Gradient Echo
SR	Slew Rate
SSD	Some of Squared Differences
SSFP	Steady State Free Precession
SS-SE-EPI	Single Shot Spin Echo Echo Planar Imaging
tACS	Transcranial Alternative Current Stimulation
tDCS	Transcranial Direct Current Stimulation
TV	Total Variation
WM	White Matter

CHAPTER 1

INTRODUCTION

1.1 Motivation

The electrical properties of biological tissues vary with the tissue's physiological activity and pathological state, providing a unique contrast for medical purposes. Pathologies such as tumors and traumatic brain injury lesions or the brain ischemia cause an alteration in the conductivity of the affected region [1–4]. The alteration of the tissue conductivity can be used to distinguish diseased tissues from nearby healthy tissues. The anisotropic conductivity distribution of the biological tissues can be acquired non-invasively using Magnetic Resonance Imaging (MRI) by means of conductivity tensor imaging methods such as diffusion tensor magnetic resonance electrical impedance tomography (DT-MREIT).

On the other hand, the current density (\bar{J}) distribution data of the externally injected currents is widely used to optimize and plan treatments like transcranial Direct Current Stimulation (tDCS), transcranial alternating current stimulation (tACS), deep brain stimulation (DBS), and many other medical applications [5–11]. Also, the knowledge of \bar{J} distribution is essential in conductivity tensor imaging methods like DT-MREIT.

Magnetic resonance current density imaging (MRCDI) is an imaging modality providing cross-sectional \bar{J} distributions of impressed currents inside the body. Since the amplitude and the duration of the externally injected current are limited by the safety concerns and the tissue-related properties acquiring high-quality \bar{J} and conductivity tensor (\bar{C}) images in a clinically acceptable scan time is an ongoing challenge of MRCDI and DT-MREIT. For instance, the amplitude of the injected current

is limited to $I \leq 2$ mA in low frequency range (< 1 kHz) for brain imaging [12]. Therefore, optimized MRI pulse sequences are needed to increase the MRCDI and DT-MREIT methods' clinical practicality. For this purpose, fast gradient echo (GE) pulse sequences are efficient pulse sequences to acquire high signal to noise ratio (SNR) images per acquisition time.

In this study, an RF spoiled GE pulse sequence with simultaneous current injection (ICNE-FLASH) and its multi echo modification (ICNE-ME-FLASH) are implemented for MRCDI data acquisitions. A novel SNR and total acquisition time analysis is proposed for these pulse sequences to investigate the combined effect of relevant sequence parameters on the acquired noisy current-induced magnetic flux density (\tilde{B}_z) and consequently the estimated \bar{J} distributions. Also, the effect the intensive utilization of multiple gradients in MRCDI experiments using the ICNE-ME-FLASH pulse sequence is studied.

To reduce the total scan time of conductivity tensor imaging, a novel reconstruction algorithm is proposed for DT-MREIT to reconstruct anisotropic conductivity images using only a single current injection. Therefore, the clinical applicability of DT-MREIT can be improved by reducing the total acquisition time, the number of current injection cables, and contact electrodes to half by decreasing the number of current injection patterns to one.

Furthermore, a novel pulse sequence is designed and implemented to combine the DTI and MRCDI data acquisitions to provide the diffusion tensor ($\bar{\bar{D}}$), \tilde{B}_z , \bar{J} , and consequently, $\bar{\bar{C}}$ distributions simultaneously.

The interaction between the static magnetic field of the MR scanner (B_0) and the injected current causes the formation of a Lorentz force, which consequently results in the magnetohydrodynamic (MHD) flow of solution molecules inside the medium. MHD flow can be encoded into the MR signal in the presence of flow encoding gradients. Therefore, a multi-contrast pulse sequence is proposed in this study based on different physical properties.

1.2 Current Density Imaging

The electrical properties of biological tissues determine the pathways of current flow through tissues. These properties may vary depending on the anatomical structure or physiological state of the tissue [1, 2, 13]. In many medical applications, knowledge of the electrical properties is essential [13]. For instance, to obtain electromagnetic field distribution inside tissues during electromagnetic stimulation [14]. Electromagnetic stimulation is used for treatment in medical applications such as transcranial magnetic stimulation [15], and radiofrequency ablation to remove arrhythmic genesis foci [16]. Knowledge of \bar{J} , distribution of the externally injected currents in the mA range inside the tissue is used to optimize and plan treatments like tDCS, tACS or DBS [5–11]. Besides, \bar{J} is a key parameter to reconstruct conductivity distributions of the biological tissues using MREIT and DT-MREIT. Cross-sectional \bar{J} distributions of impressed currents can be acquired inside the body using MRCDI technique. The current is injected to or induced in the imaging region in synchrony with an MRI pulse sequence [17, 18]. The injected current with the amplitude of I^\pm and the duration of T_C produces a local magnetic flux density, $B_z(x, y)$, distribution, which introduces a phase shift to the MR k-space signal $S^\pm(k_x, k_y)$ as:

$$S^\pm(k_x, k_y) = \int_{\Omega} \rho(x, y) e^{j\phi_0(x, y)} e^{\pm j\gamma B_z(x, y) T_C} e^{j2\pi(k_x x + k_y y)} d_x d_y \quad (1.1)$$

where $\rho(x, y)$ is the T_2 (or T_2^*) weighted spin density, $\phi_0(x, y)$ is the systematic phase artifact, and γ is the gyromagnetic constant of the Hydrogen proton. Various spin-echo (SE) and gradient-echo (GE) based pulse sequences have been developed to image B_z distribution inside the body [17, 19–26]. The SE based sequences are less sensitive to the main magnetic field inhomogeneities (ΔB_0) due to the refocusing pulse(s) and thus, have a higher signal to noise ratio (SNR). The GE based sequences are more vulnerable to ΔB_0 which causes a faster signal decay and thus lower SNR in comparison with the SE based sequences. However, the scan time of the GE based sequences is generally shorter in comparison with the SE based pulse sequences.

In the clinical application of MRCDI, I is limited to a few mA in the low-frequency range due to safety limits [27, 28]. On the other hand T_C is limited by the signal decay, which is related to the tissue properties. Due to the short T_2 (or T_2^*) value and the low proton density of biological tissues such as liver, muscle, and brain, it is difficult

to obtain a qualified (high SNR) \tilde{B}_z in these tissues within a reasonable imaging time. Therefore, optimized MRI pulse sequences are needed to increase the clinical applicability of the MRCDI method. Injected current nonlinear encoding (ICNE) technique has been developed to extend T_C until the end of the readout gradient(s) of the pulse sequence [20].

A current-controlled alternating steady-state free precession (SSFP) method is proposed to estimate \tilde{B}_z and conductivity distribution to provide a rapid imaging strategy for quantitative conductivity imaging [23].

A multi gradient echo pulse sequence with a constant gradient spoiling (SPMGE) is proposed to acquire \tilde{B}_z distribution for MREIT data acquisition, and the noise level of to be measured \tilde{B}_z for arbitrary repetition time is estimated [26].

On the other hand, the RF spoiled gradient echo (FLASH) is an efficient pulse sequence to acquire high SNR images per measurement time [29]. The effect of averaging multiple gradient echo signals on the SNR level of the human brain MR magnitude images using 3D FLASH (Fast Low Angle Shot) pulse sequence is investigated [30].

In this study, the combination of the ICNE technique with the FLASH pulse sequence is utilized to acquire the noisy B_z (\tilde{B}_z) distribution using MRCDI. Then, the \bar{J} distribution can be estimated from the measured \tilde{B}_z . Moreover, by combining ICNE with a multi-echo FLASH (ME-FLASH), as shown in Figure 1.1, the current is injected along with several acquisitions (echoes). Therefore, multiple \tilde{B}_z distributions are acquired, which can be combined using proper weights to minimize the noise level of the combined current-induced magnetic flux density (\tilde{B}_z^{comb}).

The ICNE-ME-FLASH sequence also can be utilized in DT-MREIT data acquisition to reconstruct conductivity tensor images of the biological tissues [31]. Therefore, obtaining \tilde{B}_z images with high SNR levels in a clinically reasonable time also could provide a noteworthy reference for clinical applications of conductivity imaging methods.

As a part of this thesis study, a novel analysis is performed to investigate the combined effect of relevant parameters of ICNE-ME-FLASH sequence such as the pulse

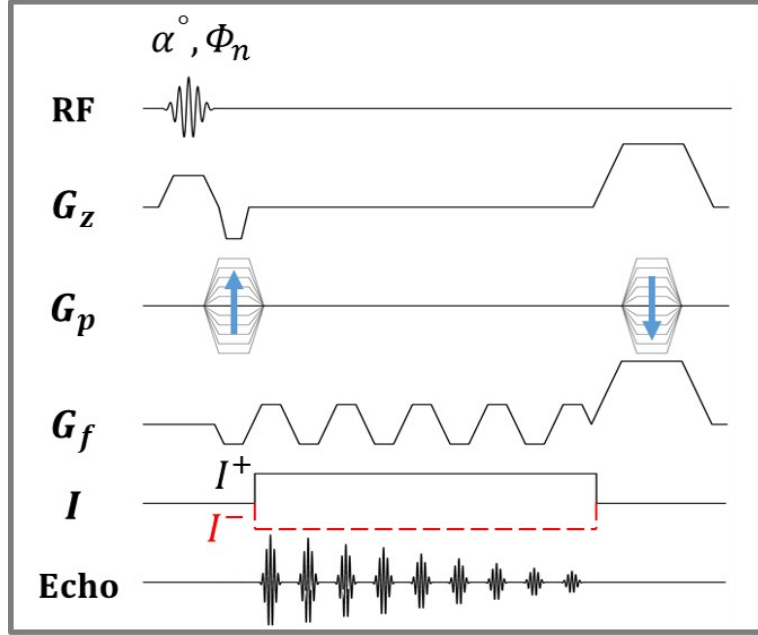


Figure 1.1: Diagram of the ICNE-ME-FLASH pulse sequence. G_z , G_p and G_f are the slice selection, phase encoding, and frequency encoding gradients, respectively. Two k-space data sets $S^\pm(k_x, k_y)$ for each echo are acquired by injecting current with opposite polarities (I^\pm) to remove the systematic phase artifacts from the acquired phase images. Φ_n is the phase of the RF excitation pulse.

repetition time (T_R), echo time(s) (T_E), flip angle (α), current injection duration(s) (T_C), and the number of excitation (N_{EX}), on the SNR level and total acquisition time of the measured \tilde{B}_z . Also, the effects of intensive utilization of multiple gradients using ICNE-ME-FLASH pulse sequence and the Magnetohydrodynamic (MHD) flow velocity in MRCDI experiments are studied.

1.3 Diffusion Tensor Imaging

Molecular diffusion is an intrinsic physical process and refers to the random translational motion of molecules due to their thermal energy. During their random motion, molecules probe tissue structure at a microscopic scale [32]. The MR signal is sensitive to motion. In the presence of diffusion encoding gradients, the random motion of water molecules (protons) due to their thermal energy causes a phase shift in the transverse magnetization. The phase shifts of protons are widely dispersed, interfere

with each other, and finally attenuate the MR signal amplitude [33]. The amount of this attenuation depends on the amplitude of molecular displacement and the amplitude and the duration of the applied diffusion encoding gradient. Therefore, the degree of diffusion weighting can be set by regulating the applied diffusion encoding gradients.

In diffusion-weighted (DW) images, regions with higher diffusion appear darker due to greater signal attenuation than regions with lower diffusion, which appear brighter. Self-diffusion of water molecules is a 3D process. In a porous medium like the tissue structure, the diffusion is not the same in all directions. The diffusion is hindered in some directions due to obstacles that limit molecular movement producing diffusion anisotropy. For instance, the diffusion anisotropy in the human brain white matter originates from the architecture of the axons. The axons in parallel bundles and their myelin shield facilitate the diffusion of the water molecules, and diffusion is faster in the direction of fiber than the perpendicular direction. The reason is that the water molecules are enclosed in the axonal spaces, and the myelin sheath prevents water diffusion outside the axons.

To encode the water molecules self-diffusion to the MR signal in a specific direction, a diffusion encoding gradient must be applied in the same direction. To fully determine the diffusion anisotropy in a voxel, diffusion encoding gradients must be applied in at least six linearly independent directions. Therefore, it is possible to estimate a diffusion tensor that describes the diffusion anisotropy at each voxel. A diffusion-weighted Spin Echo (SE) pulse sequence is shown in Figure 1.2.

In the absence of diffusion-encoding gradients, the MR signal amplitude (most often a spin-echo signal) from a voxel, S_0 , can be expressed as:

$$S_0 = \rho_0(1 - e^{-\frac{T_R}{T_1}})e^{-\frac{T_E}{T_2}} \quad (1.2)$$

where ρ_0 is the voxel spin density. T_1 and T_2 are the longitudinal and transversal relaxation times for that voxel, respectively. In the presence of diffusion-encoding gradients, molecular diffusion attenuates the MR signal exponentially as:

$$S_j = S_0 e^{-4\pi^2 \int \bar{k}_j \bar{D} \bar{k}_j^T dt} \quad j = 1 \dots N_D \quad (1.3)$$

where \bar{k}_j is:

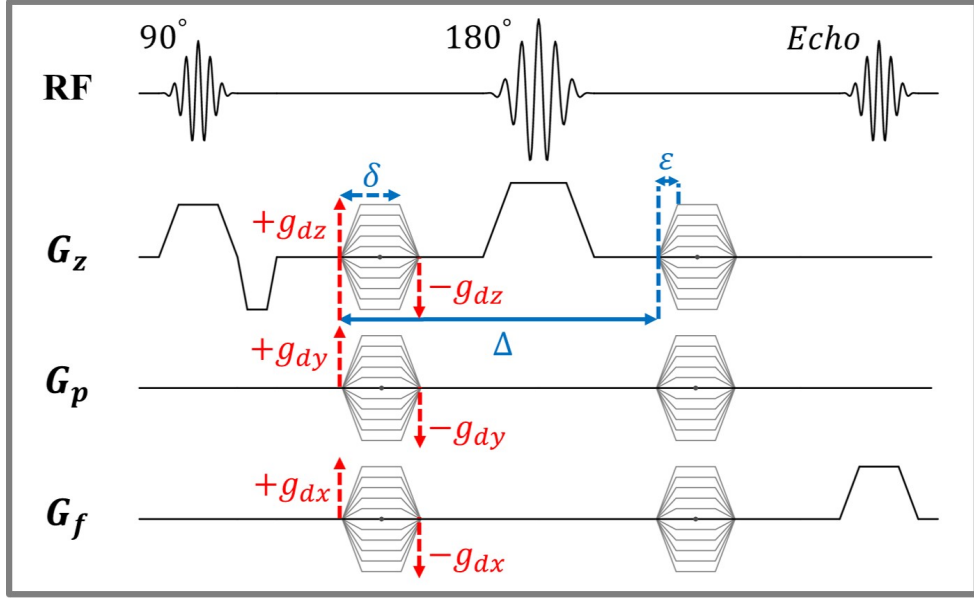


Figure 1.2: Diagram of a diffusion-weighted SE pulse sequence. A pair of diffusion gradients straddling the RF refocusing pulse. δ is the time between the first rise of the trapezoidal gradient pulse and the end of its plateau, and ε is the rise time of the pulse. Δ is the time between the starting points of the first and second diffusion encoding gradient pulses. G_z , G_p and G_f are the slice selection, phase encoding, and frequency encoding gradients, respectively.

$$\bar{k}_j = \frac{\gamma}{2\pi} \int_0^t \bar{g}_{dj}(t') dt'. \quad (1.4)$$

Here, S_j is the amplitude of the diffusion-attenuated MR signal by applying the diffusion encoding gradient \bar{g}_{dj} and N_D is the total number of diffusion encoding directions. γ is the gyromagnetic constant of Hydrogen proton and \bar{D} is the diffusion tensor. The spatial dependence of \bar{D} , S , and S_0 is not explicitly expressed in (1.3) to simplify the notation.

The parameter that controls the degree of diffusion weighting is called b -value which can be defined as:

$$b = \gamma^2 g_{dj}^2 \left[\delta^2 \left(\Delta - \frac{\delta}{3} \right) + \frac{\varepsilon^3}{30} - \frac{\delta \varepsilon^2}{6} \right]. \quad (1.5)$$

Here, δ is the time between the first rise of the trapezoidal gradient pulse and the end of its plateau, and ε is the rise time of the pulse. Δ is the time between the starting points of the first and second diffusion encoding gradient pulses, as shown in Figure 1.2. g_{dj} is the amplitude of the trapezoidal diffusion-encoding gradient pulses applied on either side of the 180° refocusing radio frequency (RF) pulse. Equation (1.3) can be written in terms of b -value as:

$$S_j = S_0 e^{-b [u_j \ v_j \ w_j] \begin{bmatrix} d_{xx} & d_{xy} & d_{xz} \\ d_{yx} & d_{yy} & d_{yz} \\ d_{zx} & d_{zy} & d_{zz} \end{bmatrix} \begin{bmatrix} u_j \\ v_j \\ w_j \end{bmatrix}} = S_0 e^{-bQ_j} \quad j = 1 \dots N_D \quad (1.6)$$

where u_j , v_j and w_j are the direction cosines of the diffusion encoding gradient vector $\bar{g}_{dj}(t')$ [34].

$$\bar{g}_{dj}(t') = g_{dj} [u_j \ v_j \ w_j] \quad (1.7)$$

In (1.6) Q_j is known as the quadratic form of the $\bar{\bar{D}}$ which only takes on positive values. The diffusion tensor matrix in (1.6) is a symmetric and positive definite matrix. Therefore, to calculate $\bar{\bar{D}}$ at least seven images must be acquired: six DW images in six linearly independent directions with any b -value and an image with $b = 0$ to yield S_0 . Using this data set and the known diffusion-encoding gradient directions and b -value, $\bar{\bar{D}}$ can be reconstructed as [34]:

$$\ln \frac{S_0}{S_j} = b [u_j \ v_j \ w_j] \begin{bmatrix} d_{xx} & d_{xy} & d_{xz} \\ d_{yx} & d_{yy} & d_{yz} \\ d_{zx} & d_{zy} & d_{zz} \end{bmatrix} \begin{bmatrix} u_j \\ v_j \\ w_j \end{bmatrix} = bQ_j \quad j = 1 \dots N_D \quad (1.8)$$

For exactly six diffusion encoding directions, (1.8) can be written for each voxel as:

$$\bar{\bar{G}} \bar{\bar{d}} = \bar{\bar{S}} \quad \equiv \quad \begin{bmatrix} u_1^2 & v_1^2 & w_1^2 & 2u_1v_1 & 2u_1w_1 & 2v_1w_1 \\ u_2^2 & v_2^2 & w_2^2 & 2u_2v_2 & 2u_2w_2 & 2v_2w_2 \\ \vdots & \vdots & \vdots & \vdots & \vdots & \vdots \\ u_6^2 & v_6^2 & w_6^2 & 2u_6v_6 & 2u_6w_6 & 2v_6w_6 \end{bmatrix} \begin{bmatrix} d_{xx} \\ d_{yy} \\ d_{zz} \\ d_{xy} \\ d_{xz} \\ d_{yz} \end{bmatrix} = \frac{1}{b} \begin{bmatrix} \ln(\frac{S_0}{S_1}) \\ \ln(\frac{S_0}{S_2}) \\ \ln(\frac{S_0}{S_3}) \\ \ln(\frac{S_0}{S_4}) \\ \ln(\frac{S_0}{S_5}) \\ \ln(\frac{S_0}{S_6}) \end{bmatrix} \quad (1.9)$$

The six elements of $\bar{\bar{D}}$ can be evaluated by solving the linear system of equations in (1.9). The diffusion-weighted measurements are typically characterized by relatively small SNR. Therefore, the accuracy and precision of the acquired $\bar{\bar{D}}$ can be optimized

when SNR is maximized at the expense of N_D [35, 36]. For $N_D > 6$ the matrix $\overline{\overline{G}}$ is no longer square and the unique tensor elements (\overline{d}) can be obtained using multivariate linear regression method [37]. As stated above, mathematically, DW images in only six linearly independent directions are necessary to reconstruct diffusion tensor. However, in practice, acquiring DW images in more directions improves the accuracy of tensor estimation at the expense of longer scan time. It is shown that for anisotropy measurement, 20 unique sampling directions provide robust measurements [38].

DT data provides information on tissue microstructure and architecture for each voxel, which can be analyzed and visualized in different ways. Since $\overline{\overline{D}}$ is symmetric and positive definite matrix, its eigenvectors are orthogonal. By eigendecomposition of matrix $\overline{\overline{D}}$ we have:

$$\overline{\overline{D}} \overline{\overline{E}} = \overline{\overline{E}} \overline{\overline{\Lambda}} \quad \ni \quad \overline{\overline{E}} = [\overline{e}_1 \ \overline{e}_2 \ \overline{e}_3], \quad \overline{\overline{\Lambda}} = \begin{bmatrix} \lambda_1 & 0 & 0 \\ 0 & \lambda_2 & 0 \\ 0 & 0 & \lambda_3 \end{bmatrix} \quad (1.10)$$

where $\overline{e}_1, \overline{e}_2, \overline{e}_3$ are the three orthogonal eigenvectors of $\overline{\overline{D}}$ and $\lambda_1, \lambda_2, \lambda_3$ are the corresponding eigenvalues. The eigenvector corresponding to the largest eigenvalue defines the main diffusion direction and the two remaining eigenvectors provide information about the degree of diffusion anisotropy and its symmetry in a voxel.

Several visualization methods and scalar indices proposed to characterize and analyze the diffusion anisotropy [39–41]. Diffusion anisotropy in a voxel can be represented by a 3D ellipsoid with three orthogonal unit eigenvectors of $\overline{\overline{D}}$ and the corresponding eigenvalues as lengths (Figure 1.3). One of the most common indices to show the amount of diffusion asymmetry in a voxel is the Fractional Anisotropy (FA), defined in terms of $\overline{\overline{D}}$ eigenvalues as [42]:

$$\text{FA} = \sqrt{\frac{(\lambda_1 - \lambda_2)^2 + (\lambda_2 - \lambda_3)^2 + (\lambda_1 - \lambda_3)^2}{2(\lambda_1^2 + \lambda_2^2 + \lambda_3^2)}} \quad (1.11)$$

The FA value varies between 0 and 1. In voxels with perfect isotropic diffusion $\lambda_1 = \lambda_2 = \lambda_3$. Thus, $\text{FA} = 0$ and $\overline{\overline{D}}$ can be represented as a sphere. However, low SNR ratios correspond to high eigenvalue discrepancies even in the perfectly isotropic voxels that cause a noise-induced bias in measured anisotropy [38]. When diffusion anisotropy increases in a voxel, eigenvalues of $\overline{\overline{D}}$ become more and more unequal,

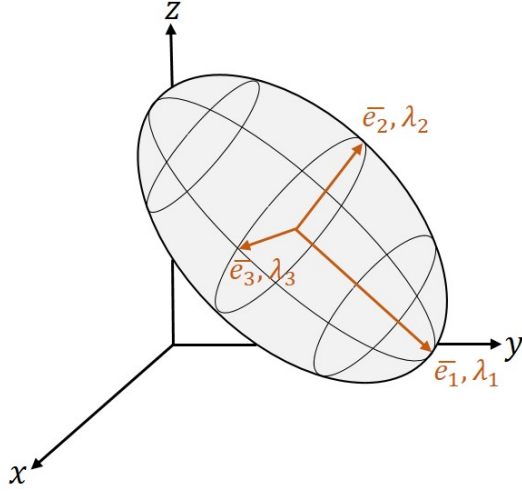


Figure 1.3: Representation of DT in a voxel as an ellipsoid with three orthogonal unit eigenvectors $\bar{e}_1, \bar{e}_2, \bar{e}_3$ and the corresponding lengths (eigenvalues) $\lambda_1, \lambda_2, \lambda_3$.

and the FA $\rightarrow 1$. With progressive diffusion anisotropy, $\overline{\overline{D}}$ ellipsoid becomes more prolated in one direction (along the main direction of diffusion).

FA map reveals differences in tissue anisotropy across space. However, it does not reflect any direction information. Color direction maps could visualize direction information of diffusion by color-coding direction information from the eigenvectors. For instance, a colored FA map assigns colors to voxels based on a combination of anisotropy and direction. In a colored FA map, the orientation of the eigenvector corresponding to the largest eigenvalue (\bar{e}_1 in Figure 1.3) controls the hue, and FA controls the brightness. The color scheme at each voxel can be obtained as:

$$\text{Red} = \text{FA} \cos \alpha, \quad \text{Green} = \text{FA} \cos \beta, \quad \text{Blue} = \text{FA} \cos \gamma \quad (1.12)$$

where α, β and γ are the angles that \bar{e}_1 makes with respect to laboratory x-, y- and z-axes, respectively.

Mean diffusivity (MD) or apparent diffusion coefficient (ADC) is another measure obtained from $\overline{\overline{D}}$, which describes the rotationally invariant magnitude of diffusion within a voxel [42].

$$\text{MD} = \frac{\lambda_1 + \lambda_2 + \lambda_3}{3} \quad (1.13)$$

The colored FA map and the MD of the experimental phantoms with anisotropic

distribution are shown in Figures 2.5 and 2.6.

1.4 Electrical Conductivity Imaging

Biological tissues have distinct electrical properties. These properties may vary with physiological activity and pathological state of the tissue providing a unique contrast for medical imaging. For instance, pathologies such as carcinoma cause regional changes in tissue composition leading to variation of the tissue conductivity, allowing diseased tissues to be distinguished from nearby healthy tissues [1, 2]. Imaging the conductivity distribution can be an effective method for differentiating brain ischemia and hemorrhagic stroke. When brain ischemia occurs, the conductivity of the affected region may decrease by 40%, but no such effect is observed in the case of hemorrhagic stroke [3,4]. Spatial information on tissue conductivity is also useful for non-invasive estimation of electric current and electromagnetic power distributions within the body [10, 43, 44].

1.4.1 Magnetic Resonance Electrical Impedance Tomography

MREIT is an imaging method providing cross-sectional isotropic electrical conductivity distribution at low frequency inside the human body using measurements of current-induced \bar{B} of the externally injected currents [45].

Let Ω be a domain in \mathbb{R}^3 with isotropic and time independent electrical conductivity σ and boundary $\partial\Omega$. Injecting a low-frequency current between two electrodes ε_1 and ε_2 on $\partial\Omega$ induces a scalar electrical potential ϕ in Ω which satisfy the boundary value problem (BVP) with the Neumann boundary condition as:

$$\begin{cases} \nabla \cdot (\sigma(\bar{r})\nabla\phi(\bar{r})) = 0 & \text{in } \Omega \\ -\sigma\nabla\phi \cdot \bar{n} = g & \text{in } \partial\Omega \end{cases} \quad (1.14)$$

where \bar{r} is the position vector in \mathbb{R}^3 , \bar{n} and g are the outward unit normal vector and a normal component of the current density on $\partial\Omega$ due to injecting I , respectively [46, 47]. On the current injection electrodes ε_1 and ε_2 :

$$\int_{\varepsilon_i} g ds = \pm I \quad \text{for } i = 1, 2 \quad (1.15)$$

where the sign of I is dependent on the current injection direction.

A unique solution ϕ of (1.14) can be obtained by setting a reference scalar electrical potential $\phi(\bar{r}_0) = 0$ for $\bar{r}_0 \in \Omega$ [46]. For a known ϕ distribution, \bar{J} in Ω can be given as:

$$\bar{J}(\bar{r}) = -\sigma(\bar{r})\nabla\phi(\bar{r}) = \sigma(\bar{r})\bar{E}(\bar{r}) \quad (1.16)$$

where \bar{E} is the electric field intensity. The \bar{B} in Ω can be expressed as:

$$\bar{B}(\bar{r}) = \bar{B}_J(\bar{r}) + \bar{B}_{SMF}(\bar{r}) \quad (1.17)$$

where $\bar{B}_J(\bar{r})$ is the magnetic flux density due to \bar{J} in Ω and $\bar{B}_{SMF}(\bar{r})$ is the stray magnetic field (SMF) induced in Ω due to currents in the current injection cables [48, 49]. The relation between \bar{B}_J and \bar{J} in Ω is given by the Biot-Savart law as:

$$\bar{B}_J = \frac{\mu_0}{4\pi} \int_{\Omega} J(\bar{r}') \frac{\bar{r} - \bar{r}'}{|\bar{r} - \bar{r}'|^3} d\bar{r}' \quad (1.18)$$

where μ_0 is the permeability of free space and $|\bar{r} - \bar{r}'|$ is the vector pointing from the source point \bar{r}' to the field point \bar{r} . The sources, influences and the correction method of SMF is given in [49]. In this study, it is assumed that $\bar{B} = \bar{B}_J$ for simplicity. From the differential form of Ampere's Circuital Law, \bar{J} in (1.16) can be expressed in Ω as:

$$\bar{J}(\bar{r}) = \frac{1}{\mu_0} \nabla \times \bar{B}(\bar{r}) \quad (1.19)$$

Equation (1.19) indicates that the volume current density at any point in space is proportional to the spatial rate of change of the magnetic field and is perpendicular to it at that point. Since MREIT deals with the externally injected currents with no internal source or sink of the same kind in Ω :

$$\nabla \cdot \bar{J}(\bar{r}) = \frac{1}{\mu_0} \nabla \cdot \nabla \times \bar{B}(\bar{r}) = 0 \quad (1.20)$$

The inverse problem of MREIT is to determine the unique σ distribution inside the body based on the measured \bar{B} or \bar{J} distributions and at least one peripheral voltage measurement [45]. Therefore, there are two types of reconstruction algorithms for MREIT: the algorithms using \bar{B} directly or B -based [28,47,50,51] and the algorithms using the current density distribution \bar{J} calculated based on the measured \bar{B} or J -based [52–54].

Almost all of the MREIT reconstruction algorithms assume isotropic conductivity distribution [28, 47, 50–64] which is not a realistic assumption for several types of biological tissues. Most of the biological tissues, such as skeletal muscle, cardiac muscle, and brain white matter, have anisotropic conductivities [65]. Hence, the isotropic conductivity assumption may lead to erroneous conductivity reconstructions.

1.4.2 Magnetic Resonance Conductivity Tensor Imaging

To overcome the drawback of MREIT in reconstructing anisotropic conductivity distributions MRCTI was proposed [66–68]. Substituting the isotropic conductivity σ with the conductivity tensor ($\overline{\overline{C}}$) in BVP of (1.14) we have:

$$\begin{cases} \nabla \cdot (\overline{\overline{C}}(\vec{r}) \nabla \phi(\vec{r})) = 0 & \text{in } \Omega \\ -\overline{\overline{C}} \nabla \phi \cdot \vec{n} = g & \text{in } \partial\Omega \end{cases} \quad (1.21)$$

where $\overline{\overline{C}} = \begin{bmatrix} c_{xx} & c_{xy} & c_{xz} \\ c_{yx} & c_{yy} & c_{yz} \\ c_{zx} & c_{zy} & c_{zz} \end{bmatrix}$ is a symmetric positive definite matrix of anisotropic conductivity. Similar to (1.16), for the i^{th} current injection pattern in Ω the corresponding \overline{J} at each voxel can be given as:

$$\overline{J}_i = -\overline{\overline{C}} \nabla \phi_i \quad \text{for } i = 1, 2. \quad (1.22)$$

The B -based and J -based reconstruction algorithms of MRCTI are proposed and implemented in [67, 68]. However, the inverse problem of MRCTI is highly ill-posed, and reconstruction of conductivity tensor images from measurements with low SNR is an ongoing challenge.

1.4.3 Diffusion Tensor - Magnetic Resonance Electrical Impedance Tomography

DT-MREIT is proposed to reconstruct the anisotropic conductivity and current density distribution of biological tissues [69, 70]. DT-MREIT is a combination of DTI and MREIT and is based on the linear relationship between the $\overline{\overline{C}}$ and $\overline{\overline{D}}$ in a porous medium as [71]:

$$\overline{\overline{C}} = \eta \overline{\overline{D}} \quad (1.23)$$

where η is the extracellular conductivity and diffusivity ratio (ECDR). Equation (1.23) can be derived from the nonlinear relation between the eigenvalues of the conductivity and diffusion tensors [33, 71] as:

$$\lambda_{c_i} = \frac{\sigma_{ext}}{d_{ext}} \left[\lambda_{d_i} \left(\frac{d_{int}}{3d_{ext}} + 1 \right) + \frac{\lambda_{d_i}^2 d_{int}}{3d_{ext}^2} + \frac{2}{3}d_{int} \right] + O(d_{int}^2), \quad i = 1, 2, 3 \quad (1.24)$$

where σ_{ext} is the extracellular conductivity, d_{int} and d_{ext} are the intracellular and extracellular diffusion coefficients, respectively. λ_{c_i} and λ_{d_i} are the eigenvalues of the conductivity and diffusion tensors and $O(d_{int}^2)$ is bounded as d_{int}^2 tends to infinity. At low frequencies, cell membranes block the flow of charge carriers across the membrane, and most of the electrical current flows through the extracellular fluid. For small intracellular diffusion $d_{int} \approx 0$, and (1.24) reduces to:

$$\lambda_{c_i} = \frac{\sigma_{ext}}{d_{ext}} \lambda_{d_i}, \quad i = 1, 2, 3 \quad (1.25)$$

which results in

$$\overline{\overline{C}} = \frac{\sigma_{ext}}{d_{ext}} \overline{\overline{E}}_D \overline{\overline{\Lambda}}_D \overline{\overline{E}}_D^T = \frac{\sigma_{ext}}{d_{ext}} \overline{\overline{D}} = \eta \overline{\overline{D}}. \quad (1.26)$$

Here, $\overline{\overline{E}}_D$ is the eigenvector matrix of the water self-diffusion tensor $\overline{\overline{D}}$, $\overline{\overline{\Lambda}}_D$ is the diagonalized eigenvalues of the diffusion tensor. The scale between the extracellular conductivity and diffusion (η) is also derived with an approach based on the Stokes-Einstein equation as [72]:

$$\eta = \frac{r_w q^2 N}{r_i k T} \quad (1.27)$$

where, r_w and r_i are the Stokes radii of the water molecule and the ion in the medium, respectively. q is the charge of the electron, N is the ion density, k is the Boltzman constant, and T is the absolute temperature in K.

The primary concern of DT-MREIT is to reconstruct anisotropic electrical conductivity at frequencies below 1 kHz due to the relatively slow nature of the most electrophysiological currents. The frequencies observed for action potentials in a neuron is about 200-300 Hz. The absolute refractory period can last between 1-2 ms. Therefore, the maximum frequency response is in the range of 500-1000 Hz. As mentioned above, the cell membrane blocks the movement of the charge carriers at low frequencies, which results in an anisotropic tissue conductivity [73].

In general, CTI reconstruction algorithms can be grouped into two:

1. The algorithms using the measured \tilde{B}_z directly or B-based,
2. The algorithms using the estimated \bar{J} from the measured \tilde{B}_z or J-based.

In J-based algorithms, the \bar{J} distribution is calculated from the measured \tilde{B}_z distribution using numerical differentiation techniques. These derivative methods cause a reduction in the structural information of the estimated current density and, consequently, the reconstructed conductivity images [45]. DT-MREIT can be thought of as a J-based algorithm. However, in DT-MREIT, the diffusion tensor data also provides structural information of the imaging slice. The ECDR distribution is a function of $\bar{D}^{-1}\bar{J}$ and the conductivity tensor is obtained as $\bar{C} = \eta\bar{D}$. Therefore, the effect of the structural information loss in DT-MREIT is expected to be less than the other conductivity imaging methods, which only use the \bar{J} information to reconstruct conductivity distribution.

In the literature, ECDR distribution is obtained by utilizing two linearly independent current injections applied via two pairs of surface electrodes [69, 73, 74]. The performance of the DT-MREIT method has been demonstrated in canines [73] and the human brain [74]. One of the primary goals of this Thesis study was to reconstruct the conductivity tensor of an anisotropic medium using DT-MREIT by a single current injection. By utilization of a single current injection instead of two, the total scan time of MRCDI, the number of current injection cables, and surface electrodes are halved. Besides, using a single current injection improves patient comfort while reducing the artefacts related to patient motion [75].

A method of producing low-frequency conductivity tensor images of biological tissues using a combination of high-frequency conductivity and multiple b -value DW images has been proposed recently [76]. Nevertheless, uniform B1 field assumption in the phase-based magnetic resonance electrical property tomography (MREPT), also, the piecewise constant conductivity assumption are not valid in practice and produce artifacts in the reconstructed images. Besides, acquiring multiple b -value diffusion images increases the total scan time considerably.

1.5 Multi-Physics Multi-Contrast Magnetic Resonance Imaging

The importance of DTI in providing unique information on the integrity of white matter structures (anisotropy) and connectivity (fiber tracking) in the human brain has generated a tremendous amount of interest in the clinical and laboratory domains. Also, the microscopic length scale and orientation information render DTI very powerful and have helped propagate the application of it in various pathologies [77, 78]. On the other hand, as it is mentioned in Section 1.2, the knowledge of the current density distribution has been used widely in many medical applications [5–11, 14–16]. Also, the electrical properties of tissues, like the conductivity distribution, could provide unique contrasts for medical imaging [1–4].

In this study, for the first time, a pulse sequence is designed and implemented to combine the DTI and MRCDI data acquisitions to provide \overline{D} , B_z , \overline{J} , and consequently \overline{C} distributions, simultaneously. Furthermore, the interaction between the static magnetic field of the MR scanner (B_0) and the injected current causes the formation of a Lorentz force, which consequently results in the magnetohydrodynamic (MHD) flow of solution molecules inside the medium [79]. For instance, during an electrocardiogram (ECG) triggered MR scan, the interaction between the conductive blood and the B_0 induces a voltage perpendicular to the blood flow and B_0 directions and distorts the measured ECG signal [80–82]. The MHD flow can be encoded into the MR signal in the presence of diffusion encoding gradients of DTI. Imaging the velocity distribution of MHD flow using MRI techniques is a recent interest of research [83–85].

1.6 The Outline of the Thesis

In this thesis study, pulse sequences and reconstruction algorithms are proposed and implemented for magnetic resonance current density, conductivity and diffusion tensor imaging. The proposed methods are examined using analytical modeling and simulation data also validated experimentally using biological tissue phantoms. This study can be divided into three main topics considering the relevance of the concepts:

1. A FLASH pulse sequence with a synchronous current application (ICNE-FLASH)

is proposed to image the B_z and \bar{J} distributions using MRCDI. The proposed pulse sequence is further developed to acquire a multi gradient echo sequence (ICNE-ME-FLASH) to take the advantages of combining the multiple echoes to achieve \tilde{B}_z^{comb} distribution with a higher SNR than the one achievable with a single echo acquisition. Furthermore, an SNR and total acquisition time analysis is proposed for the implemented pulse sequences to meet the clinical requirements of MRCDI and DT-MREIT. Also, the effects of magnetohydrodynamic flow velocity and the intensive utilization of gradients in the MRCDI experiments are studied. The theory, the mathematical derivations, analytical modeling and the methods developed for this topic are given in Chapter 2: Section 2.1. The results of the proposed methods in Section 2.1 using the simulated and experimental data are given in Chapter 3: Section 3.1.

2. A novel reconstruction algorithm is proposed to solve the inverse problem of DT-MREIT using a single and dual current injections. Reconstructing the conductivity tensor distribution by only a single current injection may increase the clinical practicality of DT-MREIT by reducing the total acquisition time, the number of cables, and contact electrodes. The DTI pulse sequences and the associated data acquisition procedures to be used in the reconstruction process of DT-MREIT are presented in Chapter 2: Section 2.3. The proposed dual and single current DT-MREIT are explained in Chapter 2: Section 2.4. The acquired $\bar{\bar{D}}$, estimated \bar{J} , and the reconstructed ECDC (η), and \bar{C} distributions of the simulation models and experimental phantoms are given in Chapter 3: Section 3.2.

3. A novel pulse sequence is designed and implemented to combine DTI and MRCDI data acquisitions to increase the clinical applicability of DT-MREIT. Simultaneous DTI and MRDCI also result in emerging MHD flow distribution. The theory behind the MHD flow imaging is explained in Chapter 2: Section 2.5. The proposed pulse sequence and the reconstruction methods and imaging procedures to extract the multiple contrasts from the acquired MR signal are given in Chapter 2: Section 2.6. The experimental results of the proposed multi-contrast imaging pulse sequence are given in Chapter 3: Section 3.3.

The discussion of the results and the findings of this thesis study are discussed in Chapter 4. The Chapters 5 contains the conclusions of this thesis study.

CHAPTER 2

THEORY AND THE MATHEMATICAL DERIVATIONS OF THE PROPOSED PULSE SEQUENCES AND THE RECONSTRUCTION ALGORITHMS FOR MRCDI, DT-MREIT, AND MULTI-CONTRAST IMAGING

The materials of this chapter can be divided into three main parts. In the first part, the ICNE-FLASH and ICNE-ME-FLASH pulse sequences and the associated SNR and total acquisition time analysis are proposed for the MRCDI and DT-MREIT data acquisitions in Section 2.1. In the second part, the employed projected current density reconstruction algorithm and the DTI method for experimental data acquisitions of DT-MREIT are given in Sections 2.2 and 2.3, respectively. A novel single and dual current DT-MREIT reconstruction algorithm is proposed in Section 2.4, and the associated equations and the mathematical derivations are explained. Finally, in the third part, the theory behind and the fundamental equations of the MHD flow are given in Section 2.5. A novel multi-contrast imaging pulse sequence and the related reconstruction algorithms are proposed to acquire multi-physics multi-contrast data using a single pulse sequence in Section 2.6.

All proposed methods are validated using the data acquired from the numerical models and the experimental phantoms shown in each section of this chapter.

2.1 SNR Analysis of the Acquired \tilde{B}_z

The clinical applicability of DT-MREIT and MRCDI is highly dependent on the sensitivity of the acquired \tilde{B}_z and the estimated \bar{J} distributions. In this section, a novel SNR and total acquisition time analysis for the measured \tilde{B}_z using the ICNE-FLASH

pulse sequence (with a single echo) is derived and explained; then, the proposed analysis is expanded for the ICNE-ME-FLASH pulse sequence.

2.1.1 Spoiled Gradient Echo Pulse Sequences

In GE pulse sequences, almost all of the magnetization in the imaging slice experience a train of excitation pulses with the same flip angle α . After a sufficient number of excitations, the longitudinal magnetization (M_z) reaches a steady-state. Based on the response of the transverse magnetization (M_\perp) in the steady-state, GE pulse sequences are classified.

The GE pulse sequence is said to be spoiled if the M_\perp becomes zero before the next α pulse. The spoiling can be done by applying a spoiler gradient at the end of each T_R . To perform an effective spoiling, the area of the spoiler gradient must vary at each T_R . Since the spoiler gradients produce spatially varying fields, this method results in a spatially non-uniform spoiling [34]. Instead, the RF spoiling method can be utilized. In this method, the phase of the α pulse is incremented systematically. Also, a constant gradient is applied at the end of each T_R . In addition to more uniform results, RF spoiling reduces the eddy currents due to the application of varying spoiler gradients from T_R to T_R [29, 34, 86]. Furthermore, in the RF spoiled GE (FLASH) pulse sequence, a phase encoding rewinder must be applied since the net gradient area on any of the three logical axes must not vary from T_R to T_R .

In this study, the FLASH pulse sequence with synchronous current injection (ICNE-FLASH) is implemented to acquire the \tilde{B}_z distribution inside the body. There are many α pulse phase cycling schedules to provide RF spoiling [34]. In this study, the phase cycling procedure for the implemented FLASH is such that for every RF pulse, the phase difference for the previous pulse is incremented by an increasing multiple of $\Phi_{inc} = 50^\circ$ as:

$$\Phi_j = j\Phi_{inc} \quad j = 0, 1, 2, \dots \quad (2.1)$$

2.1.2 SNR Analysis of the Acquired \tilde{B}_z Using ICNE-FLASH Pulse Sequence

Using ICNE-FLASH pulse sequence, the \tilde{B}_z distribution can be calculated from the MRI signal as [17]:

$$\tilde{B}_z(x, y) = \frac{1}{2\gamma T_C} \arg \left(\frac{m_+(x, y)}{m_-(x, y)} \right) \quad (2.2)$$

where m_+ and m_- are the MRI signals with positive and negative current injection polarities and $\arg(\cdot)$ includes any necessary phase unwrapping. The noise standard deviation of the measured \tilde{B}_z , $s_{\tilde{n}}$, can be estimated as [17]:

$$s_{\tilde{n}} = \frac{1}{2\gamma T_C \text{SNR}_M} \quad (2.3)$$

Here, \tilde{n} represents the random noise and SNR_M is the SNR of the MR magnitude image.

When the steady-state for longitudinal magnetization is reached, assuming a perfect spoiling, the signal S_{spoil} from a voxel can be expressed as [34] [87]:

$$S_{\text{spoil}}(\alpha, T_E) = \rho_0 \sin \alpha \frac{(1 - e^{-\frac{T_R}{T_1}})}{(1 - \cos \alpha e^{-\frac{T_R}{T_1}})} e^{-\frac{T_E}{T_2^*}} \quad (2.4)$$

Here, ρ_0 is the voxel spin density and T_E is the echo time. T_1 and T_2^* represent the longitudinal and transversal relaxation times, respectively. The external current is injected at each T_R starting from the end of α pulse to the end of the readout gradient. Hence, it can be assumed that $T_E \approx T_C$ and SNR_M in (2.3) can be expressed as:

$$\text{SNR}_M \propto \rho_0 \sin \alpha \frac{(1 - e^{-\frac{T_R}{T_1}})}{(1 - \cos \alpha e^{-\frac{T_R}{T_1}})} e^{-\frac{T_C}{T_2^*}} \quad (2.5)$$

Thus, an SNR level function of the acquired \tilde{B}_z , $\xi_{\tilde{B}_z}$, can be defined as:

$$\frac{\hat{B}_z}{s_{\tilde{n}}} \propto \xi_{\tilde{B}_z} = 2\hat{B}_z \gamma T_C \rho_0 \sin \alpha \frac{(1 - e^{-\frac{T_R}{T_1}})}{(1 - \cos \alpha e^{-\frac{T_R}{T_1}})} e^{-\frac{T_C}{T_2^*}} \quad (2.6)$$

where \hat{B}_z is the estimated noise-free current-induced magnetic flux density distribution inside the tissue. The SNR level functions of the \tilde{B}_z distribution considering the relaxation parameters of the human brain white matter (WM) for a range of different sequence parameters are shown in Figure 3.1.

Considering (2.6), the SNR level curves converge to a finite value as T_R goes to infinity. Hence, for a single excitation, the maximum achievable SNR level, $\xi_{\tilde{B}_z}^{max}$, when T_R goes to the infinity and $\alpha = 90^\circ$ can be expressed as:

$$\lim_{\substack{T_R \rightarrow \infty \\ \alpha = 90^\circ}} \xi_{\tilde{B}_z} = 2\hat{B}_z \gamma T_C \rho_0 e^{-\frac{T_C}{T_2^*}} = \xi_{\tilde{B}_z}^{max} \quad (2.7)$$

On the other hand, another factor that affects the SNR level of the measured \tilde{B}_z is the N_{EX} . Therefore N_{EX} is included in (2.6) to obtain $\xi_{\tilde{B}_z}^*$ as:

$$\xi_{\tilde{B}_z}^* = 2\hat{B}_z \gamma T_C \rho_0 \sin \alpha \frac{(1 - e^{-\frac{T_R}{T_1}})}{(1 - \cos \alpha e^{-\frac{T_R}{T_1}})} e^{-\frac{T_C}{T_2^*}} \sqrt{N_{EX}} \quad (2.8)$$

Now by including the effect of N_{EX} finite T_R values to achieve $\xi_{\tilde{B}_z}^{max}$ can be obtained by matching $\xi_{\tilde{B}_z}^{max}$ and $\xi_{\tilde{B}_z}^*$ as:

$$\xi_{\tilde{B}_z}^* = \xi_{\tilde{B}_z}^{max} \Rightarrow T_R = T_1 \ln \frac{\sin \alpha \sqrt{N_{EX}} - \cos \alpha}{\sin \alpha \sqrt{N_{EX}} - 1} \quad \text{s.t.} \quad N_{EX} > \frac{1}{\sin^2 \alpha} \quad (2.9)$$

The constraint $N_{EX} > \frac{1}{\sin^2 \alpha}$ is needed to ensure the existence of a finite T_R value satisfying (2.9). Note that (2.9) provides a relation between T_R , α , and N_{EX} .

Also, by including the effect of N_{EX} in (2.8), one can obtain a higher SNR level than $\xi_{\tilde{B}_z}^{max}$ in (2.7). For instance, for $N_{EX} = 2$, $\alpha = 90^\circ$ and $T_R \rightarrow \infty$, the $\xi_{\tilde{B}_z}^*$ in (2.8) becomes $\sqrt{2} \xi_{\tilde{B}_z}^{max}$. Therefore, further combinations resulting in lower or higher SNR levels can be obtained. Hence, (2.9) can be rewritten to provide $K \xi_{\tilde{B}_z}^{max}$ SNR level as:

$$\xi_{\tilde{B}_z}^* = K \xi_{\tilde{B}_z}^{max} \Rightarrow T_R = T_1 \ln \frac{\sin \alpha \sqrt{N_{EX}} - K \cos \alpha}{\sin \alpha \sqrt{N_{EX}} - K} \quad \text{s.t.} \quad N_{EX} > \frac{K^2}{\sin^2 \alpha} \quad (2.10)$$

The results of the combined effect of changing T_R , α , and N_{EX} to acquire \tilde{B}_z with $K = 0.5, 1$ and 2 , are shown in Figure 3.2.

For a chosen N_{EX} , the α value that provides the shortest total acquisition time ($T_R \times N_{PE} \times N_{EX}$) for the same SNR level, can be calculated from (2.9) as:

$$\frac{d}{d\alpha} N_{EX} N_{PE} T_1 \ln \frac{\sin \alpha \sqrt{N_{EX}} - \cos \alpha}{\sin \alpha \sqrt{N_{EX}} - 1} = 0 \quad (2.11)$$

Equation (2.11) is equal to zero when $\alpha = \alpha_t$ (minimum time angle). Hence, for a chosen N_{EX} , α_t is calculated as:

$$\alpha_t(N_{EX}) = \cos^{-1} \left(\frac{N_{EX} - 1}{N_{EX} + 1} \right) \quad (2.12)$$

Similar to (2.9), (2.12) can be generalized with K as:

$$\alpha_t(N_{EX}) = \cos^{-1} \left(\frac{N_{EX} - K^2}{N_{EX} + K^2} \right) \quad \text{s.t.} \quad N_{EX} \geq K^2 \quad (2.13)$$

The constraint $N_{EX} \geq K^2$ must be satisfied to ensure that $\alpha_t \leq 90^\circ$. The results of the calculated α_t for different K values using (2.13) are shown in Figure 3.3(b).

2.1.3 SNR Analysis of the Measured Multiple \tilde{B}_z Using ICNE-ME-FLASH Pulse Sequence

It is possible to acquire multiple \tilde{B}_z distributions in a single T_R using ICNE-ME-FLASH pulse sequence and compute a linear combination of these multiple \tilde{B}_z distributions to achieve a higher SNR level than the one achievable with a single echo acquisition.

The SNR analysis given for a single echo is also valid for multiple gradient echoes. Besides, in the case of multiple gradient echoes, the effect of multiple T_C values on the SNR of the \tilde{B}_z^{comb} must be investigated. An optimal weight set to combine the measured multiple \tilde{B}_z to maximize the SNR can be calculated as [26]:

$$w_j = \frac{(T_c^j)^2 e^{-\frac{2T_c^j}{T_2^*}}}{\sum_{j=1}^{N_E} (T_c^j)^2 e^{-\frac{2T_c^j}{T_2^*}}} \quad j = 1 \dots N_E \quad (2.14)$$

where N_E is the total number of echoes, and superscript j indicates the echo number. The \tilde{B}_z^{comb} distribution can be obtained as:

$$\tilde{B}_z^{comb} = \sum_{j=1}^{N_E} w_j \tilde{B}_z^j \quad (2.15)$$

The \tilde{B}_z^j can be expressed as:

$$\tilde{B}_z^j = \hat{B}_z + \tilde{n}^j \quad (2.16)$$

where \tilde{n}^j is the additive i.i.d. white Gaussian noise of the j^{th} echo. Note that \hat{B}_z in (2.16) does not depend on the echo number. The magnitude of the \hat{B}_z measured from multiple echoes depends on the magnitude of the injected current and the geometry of the imaging object. Under sufficiently high system SNR, \tilde{n}^j can be assumed as the

independent and identically distributed (i.i.d.) white Gaussian noise [88, 89] with the standard deviation of $s_{\tilde{n}^j}$:

$$s_{\tilde{n}^j} \propto \frac{1}{2\gamma T_C^j \rho_0 \sin \alpha \frac{(1-e^{-\frac{T_R}{T_1}})}{(1-\cos \alpha e^{-\frac{T_R}{T_1}})} e^{-\frac{T_C^j}{T_2^*}}}. \quad (2.17)$$

Combining (2.15) and (2.16) results in:

$$\tilde{B}_z^{comb} = \sum_{j=1}^{N_E} w_j \hat{B}_z + \sum_{j=1}^{N_E} w_j \tilde{n}^j. \quad (2.18)$$

Since $\sum_{j=1}^{N_E} w_j = 1$,

$$\tilde{B}_z^{comb} = \hat{B}_z + \sum_{j=1}^{N_E} w_j \tilde{n}^j \quad (2.19)$$

Let's call $\sum_{j=1}^{N_E} w_j \tilde{n}^j$ as \tilde{n}_w . Note that \tilde{n}_w is a linear combination of i.i.d white Gaussian noise distributions. Hence, \tilde{n}_w also has zero-mean Gaussian distribution, and due to independence, its standard deviation can be estimated as:

$$s_{\tilde{n}_w} = \sqrt{\sum_{j=1}^{N_E} (w_j s_{\tilde{n}^j})^2} \quad (2.20)$$

Substituting (2.14) and (2.17) in (2.20):

$$s_{\tilde{n}_w} \propto \frac{f(\rho_0, \alpha, T_R)}{\sum_{j=1}^{N_E} (T_C^j)^2 e^{-\frac{2T_C^j}{T_2^*}}} \sqrt{\sum_{j=1}^{N_E} (T_C^j)^2 e^{-\frac{2T_C^j}{T_2^*}}} = \frac{f(\rho_0, \alpha, T_R)}{\sqrt{\sum_{j=1}^{N_E} (T_C^j)^2 e^{-\frac{2T_C^j}{T_2^*}}}} \quad (2.21)$$

where $f(\rho_0, \alpha, T_R) = \frac{1}{2\gamma \rho_0 \sin \alpha \frac{(1-e^{-\frac{T_R}{T_1}})}{(1-\cos \alpha e^{-\frac{T_R}{T_1}})}}$.

Let's call the current injection duration of the last echo as T_C . The time interval between the two consecutive echoes, ΔT , is dependent on the readout gradient bandwidth (BW). Hence, (2.21) can be rewritten in terms of these new variables as:

$$s_{\tilde{n}_w} \propto \frac{f(\rho_0, \alpha, T_R)}{\sqrt{\sum_{j=1}^{N_E} (T_C - (j-1)\Delta T)^2 e^{-\frac{2(T_C - (j-1)\Delta T)}{T_2^*}}}}. \quad (2.22)$$

To maximize the SNR of the \tilde{B}_z^{comb} with respect to T_C :

$$\frac{\partial}{\partial T_C}(s_{\tilde{n}_w}) \propto \frac{f(\rho_0, \alpha, T_R)}{\left(\sum_{j=1}^{N_E} (T_C - (j-1)\Delta T)e^{-\frac{(T_C - (j-1)\Delta T)}{T_2^*}}\right)^3}$$

$$\frac{\partial}{\partial T_C} \sum_{j=1}^{N_E} \left((T_C - (j-1)\Delta T)e^{-\frac{(T_C - (j-1)\Delta T)}{T_2^*}} \right)^2 = 0 \quad (2.23)$$

To find the solution of $\frac{\partial}{\partial T_C}(s_{\tilde{n}_w}) = 0$, it is enough to look for the solution of:

$$\frac{\partial}{\partial T_C} \sum_{j=1}^{N_E} \left((T_C - (j-1)\Delta T)e^{-\frac{(T_C - (j-1)\Delta T)}{T_2^*}} \right)^2 = 0 \quad (2.24)$$

Taking the partial derivative and expanding the summation:

$$T_C(T_2^* - T_C) \sum_{j=0}^{N_E-1} e^{\frac{2j\Delta T}{T_2^*}} + (2T_C\Delta T - \Delta T T_2^*) \sum_{j=0}^{N_E-1} j e^{\frac{2j\Delta T}{T_2^*}} - \Delta T^2 \sum_{j=0}^{N_E-1} j^2 e^{\frac{2j\Delta T}{T_2^*}} = 0 \quad (2.25)$$

For simplicity: $A = \sum_{j=0}^{N_E-1} e^{\frac{2j\Delta T}{T_2^*}}$, $B = \sum_{j=0}^{N_E-1} j e^{\frac{2j\Delta T}{T_2^*}}$ and $C = \sum_{j=0}^{N_E-1} j^2 e^{\frac{2j\Delta T}{T_2^*}}$.

Finally, the optimal T_C that minimizes (2.22) is one of the roots of the polynomial:

$$-AT_C^2 + (AT_2^* + 2B\Delta T)T_C - B\Delta T T_2^* - C\Delta T^2 = 0 \quad (2.26)$$

Using (2.26) the optimum total current injection duration for a given N_E and ΔT is calculated. Then the other T_C^j values can be calculated as:

$$T_C^j = T_C - (N_E - j)\Delta T \quad j = 1 \dots N_E - 1 \quad (2.27)$$

2.1.4 Noise Estimation of the Measured \tilde{B}_z

To estimate the $s_{\tilde{n}}$ of the experimentally measured \tilde{B}_z distributions the method in [89] is used. For a homogeneous conductivity distribution, it is shown that $\nabla^2 \hat{B}_z = 0$ [47, 60]. Therefore, for each echo (2.16) can be expressed as:

$$\nabla^2 \tilde{B}_z = \nabla^2 \tilde{n} \quad (2.28)$$

Acquiring \tilde{B}_z from at least three consecutive slices in the z-direction, (2.28) can be expressed using the finite difference approximation of the Laplacian operator as:

$$\begin{aligned} \nabla^2 \tilde{B}_z(x, y, z) = & \\ & \frac{1}{\Delta^2} [\tilde{n}(x+1, y, z) + \tilde{n}(x-1, y, z) + \tilde{n}(x, y+1, z) + \tilde{n}(x, y-1, z)] \\ & - \frac{4}{\Delta^2} \tilde{n}(x, y, z) + \frac{1}{\Delta_z^2} [\tilde{n}(x, y, z+1) + \tilde{n}(x, y, z-1)] - \frac{2}{\Delta_z^2} \tilde{n}(x, y, z), \end{aligned} \quad (2.29)$$

where Δ is the pixel size in the x-y plane and Δ_z is the slice thickness. Since \tilde{n} is i.i.d white Gaussian noise with the variance of $s_{\tilde{n}}^2$ in all pixels, the variance of $\nabla^2 \tilde{B}_z(x, y, z)$ can be expressed as:

$$\begin{aligned} s_{\nabla^2 \tilde{B}_z}^2 = & \\ 4 \left(\frac{1}{\Delta^2} s_{\tilde{n}} \right)^2 + \left(\frac{4}{\Delta^2} s_{\tilde{n}} \right)^2 + 2 \left(\frac{1}{\Delta_z^2} s_{\tilde{n}} \right)^2 + \left(\frac{2}{\Delta_z^2} s_{\tilde{n}} \right)^2 = & \left(\frac{20}{\Delta^4} + \frac{6}{\Delta_z^4} \right) s_{\tilde{n}}^2 \end{aligned} \quad (2.30)$$

Here, $s_{\nabla^2 \tilde{B}_z}$ is the standard deviation of the Gaussian random noise in $\nabla^2 \tilde{B}_z$. Since $s_{\nabla^2 \tilde{B}_z}^2$ can be estimated from the calculated $\nabla^2 \tilde{B}_z$ in (2.29), $s_{\tilde{n}}$ can be estimated experimentally from the measured \tilde{B}_z using the relation in (2.30) as:

$$s_{\tilde{n}} = \frac{1}{\sqrt{\frac{26}{\Delta^4} + \frac{6}{\Delta_z^4}}} s_{\nabla^2 \tilde{B}_z} \quad (2.31)$$

2.1.5 Effect of Intensive Utilization of Gradients on the Measured \tilde{B}_z

The intensive utilization of gradient pulses causes spatial and temporal variations of the main magnetic field, B_0 , consistent with the resistive heating of the magnet structures. Since MR phase measurements are sensitive to the errors related to the B_0 inhomogeneities, correction strategies are required [90].

The effect of intensive utilization of gradients on B_0 variation (ΔB_0), can be calculated as [90]:

$$\Delta B_0(\bar{r}, t_2 - t_1, T_E^j) = \frac{\Delta \phi(\bar{r}, t_2 - t_1, T_E^j)}{\gamma T_E^j} \quad j = 1 \dots N_E \quad (2.32)$$

where T_E^j is the echo time of the j^{th} echo, and $\Delta \phi(\bar{r}, t_2 - t_1, T_E^j)$ is the difference between the two MR phase images acquired with the same T_E^j at different time instants (t_1 and t_2).

The interaction of the rapidly switched gradient fields with other MR scanner structures, especially when an intensive number of gradient pulses are used, causes emerging high eddy currents. The emerging eddy currents generate local magnetic fields, which cause problems in the acquired MR magnitude and phase images. Also, a remarkable temperature increase occurs due to eddy current heating of the RF shield. The RF shield is a metallic structure beneath the scanner's inner plastic wall near the patient. When the patient's body becomes a part of an eddy current loop, it is necessary to prevent the patient from touching the inner wall to prevent possible burns [91, 92].

The effect of intensive gradient utilization on the temperature elevation induced around metallic hip prosthesis is predicted numerically [93]. Due to the emerging eddy currents, the implant itself is heated, and thermal conduction causes heating of the tissues nearby [94]. Heating in metallic implants is investigated in a 1.5 T whole-body unit [95]. It is shown that the heating depends on the implant's geometry and its physical properties, the distance from the isocenter, and the switched gradient field sequence.

To investigate the effect of ΔB_0 on the measured \tilde{B}_z in MRCDI experiments, a set of N measurements are acquired using the ICNE-ME-FLASH sequence with the same parameters. A single measurement without current injection is also acquired to remove systematic phase components from the MR phase measurements. Therefore, the obtained phase measurement related to j^{th} echo $\tilde{\phi}^j(x, y)$ of ICNE-ME-FLASH sequence can be given as:

$$\tilde{\phi}^j(x, y) = \hat{\phi}^j(x, y) + \tilde{n}_\phi^j(x, y) \quad j = 1 \dots N_E \quad (2.33)$$

where $\hat{\phi}^j(x, y)$ and $\tilde{n}_\phi^j(x, y)$ are the noise-free current-induced phase and the additive noise of the j^{th} echo, respectively. By scaling $\tilde{\phi}^j(x, y)$ with $\gamma = 267.513 \times 10^6 \text{ rad s}^{-1} \text{T}^{-1}$ and T_C , \tilde{B}_z distributions can be obtained.

As in (2.16), \tilde{n}^j of \tilde{B}_z^j measurements are assumed as i.i.d Gaussian random noise with zero mean. Therefore, to estimate the noise distribution, $D_i^j(x, y)$, and the noise variance, $s_{\tilde{n}^j}^2$, for each echo, the sample mean, $\hat{\mu}^j(x, y)$, of $N \tilde{B}_z$ measurements can

be estimated as:

$$\hat{\mu}^j(x, y) = \frac{1}{N} \sum_{i=1}^N \tilde{B}_{z_i}^j(x, y) \quad j = 1 \dots N_E \quad (2.34)$$

where $\tilde{B}_{z_i}^j(x, y)$ is the noisy current-induced magnetic flux density distribution of the i^{th} measurement of the j^{th} echo. Therefore, noise distributions of each echo for N measurements, can be estimated as:

$$D_i^j(x, y) = \sum_{i=1}^N \left(\tilde{B}_{z_i}^j(x, y) - \hat{\mu}^j(x, y) \right) \quad j = 1 \dots N_E. \quad (2.35)$$

Then, $s_{n_j}^2$ can be estimated as:

$$\frac{1}{NM} \sum_{m=1}^M \sum_{i=1}^N \left(\tilde{B}_{z_i}^j(x, y) - \hat{\mu}^j(x, y) \right)^2 = s_{n_j}^2 \quad j = 1 \dots N_E \quad (2.36)$$

where M is the total number of pixels in the measured \tilde{B}_z images. The results of the calculated ΔB_0 using (2.32) and the estimated $D_i^j(x, y)$ and $s_{n_j}^2$ for $N = 50$ acquisitions of an imaging phantom using ICNE-ME-FLASH pulse sequence are given in Figures 3.8-3.9.

2.1.6 Effects of the B_0 and BW on SNR of the Measured \tilde{B}_z

Including the effects of the MR main magnetic field strength (B_0) and the readout bandwidth (BW) the SNR_{M^j} in (2.5) can be expressed as [96]:

$$\text{SNR}_{M^j} \propto B_0^{\frac{3}{2}} \frac{1}{\sqrt{\text{BW}}} \rho_0 \sin \alpha \frac{(1 - e^{-\frac{T_R}{T_1}})}{(1 - \cos \alpha e^{-\frac{T_R}{T_1}})} e^{-\frac{T_C^j}{T_2^*}} \quad (2.37)$$

It is known that the tissue's T_1 and T_2^* relaxation times increase and decrease, respectively, by increasing B_0 . For the range of $B_0 = 0.2 - 7$ T, the relation between T_1 and B_0 of the soft brain tissues can be estimated as [97, 98]:

$$T_1(\text{ms}) = a(\gamma B_0)^b \quad (2.38)$$

where γ is given in Hz T^{-1} . The parameters a and b are calculated as $a = 0.71, 1.16, 3.35$ and $b = 0.382, 0.376, 0.340$ for the WM, gray matter (GM), and blood, respectively. The relation between T_2^* and B_0 can be expressed as [99]:

$$T_2^*(\text{ms}) = a e^{-b B_0} \quad (2.39)$$

with $a = 64$ ms, 90 ms, and $b = -0.132 \text{ T}^{-1}$, -0.142 T^{-1} for the WM and GM, respectively. Since the effects of BW (sampling rate) and B_0 on the SNR level of the acquired MR magnitude images are well studied in the literature [47, 52, 57–60], the effect of these parameters are neglected on the SNR of the \tilde{B}_z images by assigning $B_0^{\frac{3}{2}} \frac{1}{\sqrt{\text{BW}}}$ as unity in (2.5). Two different bandwidth definitions exist in MRI discussions: the readout bandwidth and the phase encoding bandwidth. Here, these two bandwidths are defined.

2.1.6.1 Readout (frequency encoding) Bandwidth

The readout bandwidth (BW) is the range of spin precession frequencies across the FOV in the readout (the frequency encoding) direction which depends on the FOV and the amplitude of the frequency encoding gradient [34]. The bandwidth in the frequency encoding direction (FOV_x) with the length of L_x is:

$$\text{BW} = \frac{\gamma}{2\pi} G_x L_x \quad (2.40)$$

where G_x the amplitude of the frequency encoding gradient and $\frac{\gamma}{2\pi}$ is in Hz T^{-1} . Note that, with the increased G_x , which is required to minimize T_E , the BW must be increased accordingly to maintain the same FOV, resulting in a larger number of k-space samples [34]. For a constant G_x , the interval between readout points in k-space, Δk_x , is:

$$\Delta k_x = \frac{\gamma}{2\pi} G_x \Delta t \quad (2.41)$$

where $\Delta t = \frac{1}{\text{BW}}$ is the sampling time per complex point (also known as the dwell time). Combining (2.40) and (2.41) the k-space Nyquist requirement is obtained as:

$$\Delta k_x = \frac{1}{L_x}. \quad (2.42)$$

For N_x readout points the maximum extent of the acquired k-space is:

$$N_x \Delta k_x = \frac{N_x}{L_x} = \frac{1}{\Delta x} \quad (2.43)$$

where Δx is the pixel size in the frequency encoding direction. Therefore, it can be said that, the k-space sampling interval is the inverse of the length of compact support in image space or vice versa.

2.1.6.2 Phase Encoding Bandwidth

The phase encoding bandwidth (BW_{phase}) is defined as:

$$BW_{phase} = \frac{1}{t_{esp}} \quad (2.44)$$

where t_{esp} is the effective dwell time for the phase-encoding and represents the time between k_y sample points [34]. The k-space sampling interval in the phase encoding direction (k_y) is calculated as:

$$\Delta k_y = \frac{1}{L_y}. \quad (2.45)$$

Using (2.45) the phase-encoding gradient amplitude (G_y) is calculated as:

$$G_y = \frac{2\pi}{\gamma L_y t_{esp}} \quad (2.46)$$

Since t_{esp} is much longer than Δt (the readout dwell time), G_y is generally two or three times smaller (in magnitude) than the corresponding G_x .

Other parameters, such as the system SNR and the voxel size, also affect the SNR of the measured \tilde{B}_z . However, similar to the readout gradient BW and B_0 the system SNR and the voxel size are considered the same during the analyses and, therefore, are taken as unity in (2.5).

2.1.7 Imaging Phantom for Experimental Evaluation of the Proposed SNR and Total Acquisition Time Analysis of ICNE-ME-FLASH

The proposed SNR and total acquisition time analysis is examined using analytical modelling and the experimental data acquired from an imaging phantom. The imaging phantom is a 3D Plexiglas container with the dimensions of $80 \times 80 \times 80 \text{ mm}^3$ and four recessed structures with the dimensions of $30 \times 20 \times 20 \text{ mm}^3$ for electrode placement, as shown in Figure 2.1. The phantom is filled with a saline solution having conductivity and T_2 values of 0.35 S/m and 70 ms, respectively, which are the mean conductivity (for the frequencies less than 40 Hz) and the T_2 values of the human brain WM at 3T [100, 101].

Experiments performed on a 3 T clinical MRI scanner (MAGNETOM Trio, Siemens AG, Erlangen, Germany) with 60 cm bore diameter, 45 mT/m maximum gradient

strength, and a 32 channel head coil. Multi-channel data combined using the adaptive combination. The electrical current is injected into the experimental phantom employing shielded cables and copper electrodes in the horizontal direction using a custom-designed MR conditional current source [102]. The current pulses are injected in synchrony with the ICNE-ME-FLASH pulse sequence shown in Figure 1.1. The sequence parameters except T_R , N_{EX} and α are given in Table 2.1. The cables are aligned with the direction of the main magnetic field to prevent cable induced magnetic stray fields [49].

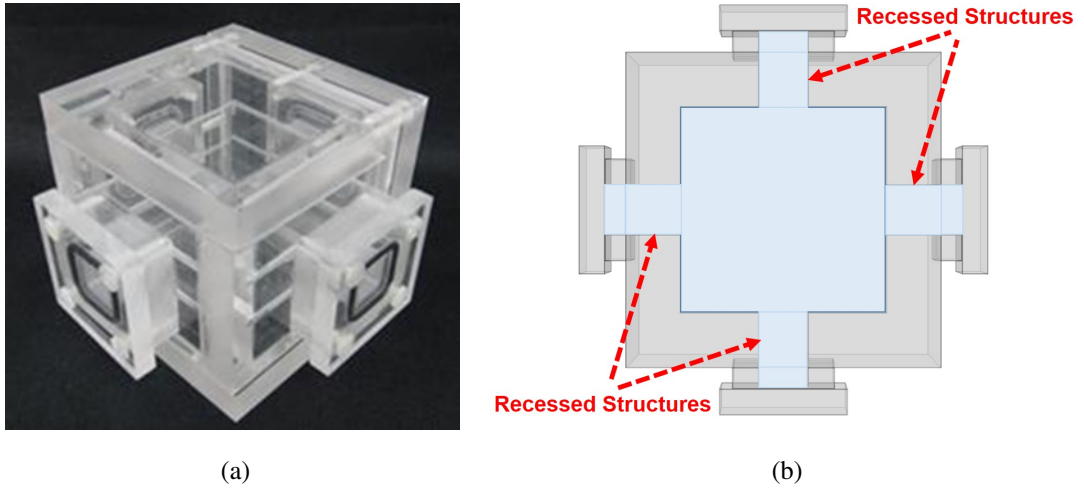


Figure 2.1: (a) The photograph of the experimental phantom and its (b) Transversal (x-y) plane. The phantom is filled with a saline solution with 2.75 g/L of NaCl and 0.034 g/L of $MnCl_2$ dissolved in pure water to mimic the mean conductivity and relaxation times of the human brain WM.

2.2 Reconstruction of the Projected Current Density Distribution (\bar{J}_p) from the Measured \tilde{B}_z

To reconstruct the \bar{J} distribution inside the human body, three components of the measured current-induced \bar{B} distribution (i.e., B_x, B_y, B_z) are required. Since the MR scanner only measures the magnetic flux density parallel to the main magnetic field direction, an object rotation is required to acquire all three components of \bar{B} . As rotating the patient inside the magnet is not possible using a conventional MR

Table 2.1: ICNE-ME-FLASH pulse sequence parameters.

Parameter	Value
Field of View (FOV)	$128 \times 128 \text{ mm}^2$
Number of Phase Encoding Steps (N_{PE})	64
Slice Thickness	5 mm
Number of Echoes (N_E)	9
T_E^1	32.5 ms
T_E^9	75 ms
ΔT	5.3 ms
I	2 mA
Current Injection Duration (T_C)	75 ms
BW	200 Hz/pixel

scanner, a method was proposed to estimate the projected current density (\bar{J}_p) from the z component of the measured magnetic flux density (\tilde{B}_z) [103].

$$\bar{J}_p = \bar{J}_0 + \frac{1}{\mu_0} \left(\frac{\partial(\tilde{B}_z - B_z^0)}{\partial y}, -\frac{\partial(\tilde{B}_z - B_z^0)}{\partial x}, 0 \right) \quad (2.47)$$

Here, \bar{J}_0 and B_z^0 , respectively, are the current density and the magnetic flux density (z-component) obtained by solving Laplace's equation for a finite element (FE) model with homogeneous conductivity distribution and the same geometry and boundary conditions as the imaging object. $\mu_0 = 4\pi \times 10^{-7} \text{ T m A}^{-1}$ is the permeability of free space. The difference between the projected and true current density distributions depends only on the difference between the z-components of the true and homogeneous current densities [103]. Hence, to minimize errors in the current density, transversal current patterns must be utilized. Consequently, J_z becomes negligible in the imaging slice.

2.3 Diffusion Tensor Imaging

One of the most prevalent pulse sequences used in the clinical application of DTI is the diffusion-weighted Single-Shot Spin-Echo EPI (SS-SE-EPI) due to its high ac-

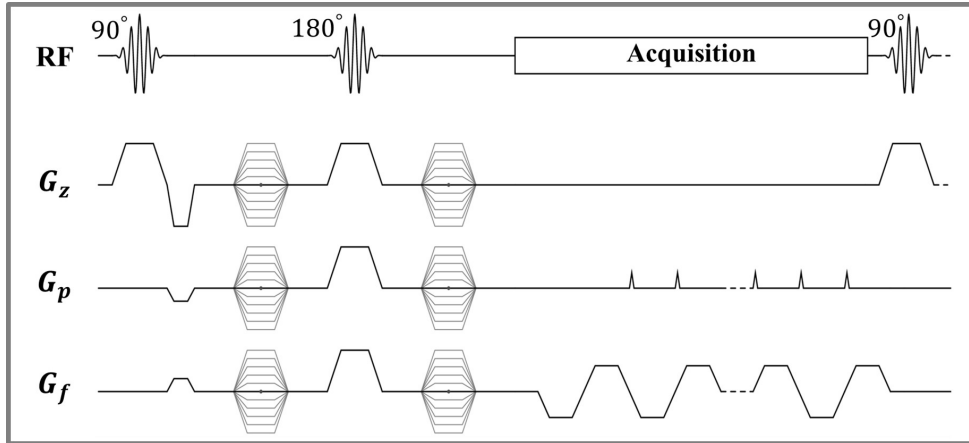


Figure 2.2: Diagram of a DW SS-SE-EPI pulse sequence. Diffusion encoding gradients can be applied in the three orthogonal directions. G_z , G_p and G_f are the slice selection, phase encoding, and frequency encoding gradients, respectively. The diffusion can be imaged in any arbitrary direction by changing the relative components throughout the three orthogonal gradient directions.

quisition speed and motion insensitivity [34]. The schematic diagram of a diffusion-weighted SS-SE-EPI pulse sequence is shown in Figure 2.2. The diffusion encoding gradients are applied on either side of the 180° RF pulse. Minimum TE values must be used to minimize the signal loss due to spin-phase dispersion. Therefore, the maximal gradient amplitude can be used to achieve the desired b -value. On the other hand, the utilization of the maximal gradient amplitude increases the slew rate (SR), which can cause the pulse sequence to exceed regulatory limits for peripheral nerve stimulation [104, 105] also cause more problems related to the eddy currents induced by the diffusion-weighting gradient [106, 107]. SR is one of the key gradient specifications measured in units of Tesla per meter per second (T/m/s) and defined as:

$$\text{SR} = \frac{\text{Peak Gradient Strength}}{\text{Rise Time}} \quad (2.48)$$

SS-SE-EPI inherits all the artifacts related to the EPI pulse sequence, such as non-linear geometric distortions due to off-resonance effects, like field inhomogeneity, magnetic susceptibility variations, and eddy currents with long time constants (e.g., > 100 ms) mainly along the phase encoding direction [34, 108]. These geometric distortions are mainly produced in the phase encoding direction, causing displacement of structures (voxel shift) [109].

Each k-space line of the single-shot EPI pulse sequence is acquired at a different time with a different T_2^* weighting, which results in a blurring in the phase encoding direction. This artifact is known as T_2^* -induced image blurring, which can be avoided effectively either by reducing the echo train length or shorten the inter echo spacing. Various artifacts and distortions related to the EPI-based pulse sequences, and the possible correction methods are explained in [34].

Generally, the SNR of images acquired using single-shot EPI is low due to wide BW and long echo training, which prolongs the T_E . Note that in single-shot EPI, a wider BW is required to reduce the chemical shift and magnetic susceptibility artifacts. On the other hand, a wide BW also reduces the effect of T_2^* -induced signal decay.

In DTI, low SNR corresponds to high eigenvalue discrepancies in the reconstructed $\overline{\overline{D}}$. Therefore, there is a noise-induced bias in anisotropy measurements, and the variance in anisotropy increases by increasing the added noise. The low SNR can be compensated by signal averaging. However, the k-space data of the DTI pulse sequence may contain inconsistent phase errors due to the high motion sensitivity of single-shot EPI. Therefore, if the signal averaging is performed in the k-space, the phase errors can cause a signal loss that varies across the image. To avoid this, the magnitude image associate with each k-space data can be calculated individually and then averaged to produce the final image or phase corrections can be applied before the averaging complex images [34]. The b -value also influences the SNR of the DW images. Low b -values provide higher SNR but at the cost of reduced angular resolution [38]. The typical b -value employed on most clinical DW imaging applications of the brain for adults is 1000 s mm^{-2} [110, 111]. However, a larger number of N_D allows a smaller b -value to be used without compromising the image quality [34].

2.3.1 Geometric Distortion of the DW Images Acquired Using SS-SE-EPI Pulse Sequence and the Correction Methods

The DW images of SS-SE-EPI are very sensitive to non-zero off-resonance fields. The sources of such fields are the susceptibility distribution of the subjects or eddy currents from the rapid switching of the diffusion encoding gradients. The former is

known as a susceptibility-induced off-resonance field, and the latter is known as an eddy current-induced off-resonance field. The effect of the field inhomogeneity on the MR k-space signal $S(k_x, k_y)$ can be given as [112]:

$$S(k_x, k_y) = \int_{-\infty}^{\infty} \int_{-\infty}^{\infty} \rho(x, y) e^{-\frac{T_E}{T_2^*(x,y)}} e^{-i\gamma\Delta B(x,y)T_E} e^{-2i\pi(k_x x + k_y y)} dx dy \quad (2.49)$$

where $\rho(x, y)$ is the proton spin density and $\Delta B(x, y)$ is the magnetic field inhomogeneity. In single-shot EPI, the geometric distortion is mainly caused by phase error accumulation over the phase encoding direction. Therefore, the spatial distortions (voxel shifts) occur particularly in the phase encoding direction [113]. The geometric distortion Δy at position (x, y) is calculated as:

$$\Delta y(x, y) = \gamma\Delta B(x, y) \frac{\text{FOV}_y}{\text{BW}_y} \quad (2.50)$$

where FOV_y and BW_y are the field of view and BW in the phase encoding direction [114]. The spatial distortions are often negligible in the frequency encoding direction due to the much larger BW.

To estimate the susceptibility induced field, the method described in [115] and implemented in FSL [116, 117] is utilized. The topup tool of FSL uses the acquired images from two acquisitions with opposing polarities of the phase encode blips. Therefore, the same field leads to distortion going in opposite directions in the two acquisitions. Using these two images and the corresponding acquisition parameters, the field is estimated such that when applied to the two volumes, it maximizes the similarity of the unwarped volumes. The similarity between the two unwarped volumes is measured by the sum of squared differences (SSD) between the unwarped images. Using SSD allows the use of Gauss-Newton for jointly finding the field and any movement that may have occurred between the two acquisitions.

2.4 The Proposed Reconstruction Algorithms for Diffusion Tensor-Magnetic Resonance Electrical Impedance Tomography

DT-MREIT is an imaging modality providing the anisotropic electrical conductivity distribution inside the body by means of DTI and MREIT techniques. This method is based on the linear relationship between the electrical conductivity and water self-

diffusion tensors ($\overline{\overline{C}}$ and $\overline{\overline{D}}$) in a porous medium. Under Neumann principle assumption, in a porous medium $\overline{\overline{C}}$ and $\overline{\overline{D}}$ share eigenvectors [69, 71]:

$$\overline{\overline{C}} = \overline{\overline{E}}_D f(\overline{\overline{\Lambda}}_D) \overline{\overline{E}}_D^T = \overline{\overline{E}}_D \overline{\overline{\Lambda}}_C \overline{\overline{E}}_D^T. \quad (2.51)$$

Here, $f(\overline{\overline{\Lambda}}_D)$ represents the diagonalized eigenvalues of $\overline{\overline{C}}$ as a function of the diagonalized eigenvalues of $\overline{\overline{D}}$.

To fully acquire the anisotropic conductivity tensor at each voxel (pixel) of a porous medium, the directional and the magnitude information of the conductivity is required. In DT-MREIT the directional information of the conductivity tensor is derived from the obtained water self-diffusion tensor data. On the other hand, the reconstructed position-dependent ECDR (1.26) provides a scale factor for each voxel regulating the relationship between the corresponding conductivity and diffusion tensors' magnitudes.

In conventional DT-MREIT to reconstruct position-dependent ECDR distribution, electrical currents are injected into the imaging region in at least two linearly independent directions in synchrony with an MRI pulse sequence. The current density distribution of the externally injected currents inside the imaging object is reconstructed using MRCDI technique. The resultant current density distribution for each pixel is given by:

$$\overline{J}_{p_i} \approx -\overline{\overline{C}} \nabla \phi_i = -\eta \overline{\overline{D}} \nabla \phi_i \quad i = 1, 2 \quad (2.52)$$

where \overline{J}_{p_i} is the estimated projected current density using (2.47) for the i^{th} current injection pattern and ϕ_i is the scalar electrical potential corresponding to \overline{J}_{p_i} . The curl-free condition of the electric field at low frequencies [73] results in:

$$\tilde{\nabla} \times (\overline{\overline{D}}^{-1} \overline{J}_{p_i}) \approx \tilde{\nabla} \ln(\eta) \times (\overline{\overline{D}}^{-1} \overline{J}_{p_i}) \quad i = 1, 2 \quad (2.53)$$

where $\tilde{\nabla} = (\frac{\partial}{\partial x}, \frac{\partial}{\partial y})$. For the two linearly independent current injection patterns, (2.53) can be expressed in the matrix form for each pixel as:

$$\begin{bmatrix} (\overline{\overline{D}}^{-1} \overline{J}_{p_1})_y & -(\overline{\overline{D}}^{-1} \overline{J}_{p_1})_x \\ (\overline{\overline{D}}^{-1} \overline{J}_{p_2})_y & -(\overline{\overline{D}}^{-1} \overline{J}_{p_2})_x \end{bmatrix}^{2 \times 2} \begin{bmatrix} \frac{\partial \ln(\eta)}{\partial x} \\ \frac{\partial \ln(\eta)}{\partial y} \end{bmatrix}^{2 \times 1} \approx \begin{bmatrix} \frac{\partial (\overline{\overline{D}}^{-1} \overline{J}_{p_1})_y}{\partial x} - \frac{\partial (\overline{\overline{D}}^{-1} \overline{J}_{p_1})_x}{\partial y} \\ \frac{\partial (\overline{\overline{D}}^{-1} \overline{J}_{p_2})_y}{\partial x} - \frac{\partial (\overline{\overline{D}}^{-1} \overline{J}_{p_2})_x}{\partial y} \end{bmatrix}^{2 \times 1} \quad (2.54)$$

By solving (2.54) as in [69, 74], $\tilde{\nabla} \ln(\eta)$ is obtained for each pixel as:

$$\begin{bmatrix} \frac{\partial \ln(\eta)}{\partial x} \\ \frac{\partial \ln(\eta)}{\partial y} \end{bmatrix}^{2 \times 1} \approx \begin{bmatrix} \left(\overline{\overline{D}}^{-1} \overline{J}_{p_1} \right)_y & \left(-\overline{\overline{D}}^{-1} \overline{J}_{p_1} \right)_x \\ \left(\overline{\overline{D}}^{-1} \overline{J}_{p_2} \right)_y & \left(-\overline{\overline{D}}^{-1} \overline{J}_{p_2} \right)_x \end{bmatrix}^{-1} \begin{bmatrix} \frac{\partial \left(\overline{\overline{D}}^{-1} \overline{J}_{p_1} \right)_y}{\partial x} - \frac{\partial \left(\overline{\overline{D}}^{-1} \overline{J}_{p_1} \right)_x}{\partial y} \\ \frac{\partial \left(\overline{\overline{D}}^{-1} \overline{J}_{p_2} \right)_y}{\partial x} - \frac{\partial \left(\overline{\overline{D}}^{-1} \overline{J}_{p_2} \right)_x}{\partial y} \end{bmatrix}^{2 \times 1} \quad (2.55)$$

To recover η , iterative methods have been proposed in [69, 73].

In this study, a new approach is proposed to recover η using the first-order discrete difference approximations of x and y gradient operators, $\overline{\overline{\delta}}_x$ and $\overline{\overline{\delta}}_y$. $\overline{\overline{\delta}}_x$ and $\overline{\overline{\delta}}_y$ are $N \times N$ (N is the total number of pixels) sparse matrices with non-zero entries 1 and -1 located according to appropriate forward and backward difference rules for the boundary pixels and central difference rule for all the other pixels [118, 119].

2.4.1 A single current injection pattern

For a single current injection, (2.54) can be expressed as:

$$\begin{bmatrix} \left(\overline{\overline{D}}^{-1} \overline{J}_{p_1} \right)_y & - \left(\overline{\overline{D}}^{-1} \overline{J}_{p_1} \right)_x \end{bmatrix}_{1 \times 2} \begin{bmatrix} \frac{\partial \ln(\eta)}{\partial x} \\ \frac{\partial \ln(\eta)}{\partial y} \end{bmatrix}_{2 \times 1} \approx \begin{bmatrix} \frac{\partial \left(\overline{\overline{D}}^{-1} \overline{J}_{p_1} \right)_y}{\partial x} - \frac{\partial \left(\overline{\overline{D}}^{-1} \overline{J}_{p_1} \right)_x}{\partial y} \end{bmatrix}_{1 \times 1} \quad (2.56)$$

Equation (2.56) can be expanded for the imaged slice, which is composed of N pixels as:

$$\overline{\overline{A}}_{N \times N} \ln(\overline{\eta})_{N \times 1} = \overline{b}_{N \times 1} \quad (2.57)$$

where

$$\overline{\overline{A}} = \text{diag}(\overline{a}_1) \overline{\overline{\delta}}_x + \text{diag}(\overline{a}_2) \overline{\overline{\delta}}_y \quad (2.58)$$

$$\begin{aligned}
\bar{a}_1 &= \begin{bmatrix} (\bar{D}^{-1} \bar{J}_{p_1})_{y,1} \\ \vdots \\ (\bar{D}^{-1} \bar{J}_{p_1})_{y,N} \end{bmatrix}_{N \times 1}, \quad \bar{a}_2 = \begin{bmatrix} (-\bar{D}^{-1} \bar{J}_{p_1})_{x,1} \\ \vdots \\ (-\bar{D}^{-1} \bar{J}_{p_1})_{x,N} \end{bmatrix}_{N \times 1}, \\
\bar{b} &= \begin{bmatrix} \left(\frac{\partial (\bar{D}^{-1} \bar{J}_{p_1})_x}{\partial y} - \frac{\partial (\bar{D}^{-1} \bar{J}_{p_1})_y}{\partial x} \right)_1 \\ \vdots \\ \left(\frac{\partial (\bar{D}^{-1} \bar{J}_{p_1})_x}{\partial y} - \frac{\partial (\bar{D}^{-1} \bar{J}_{p_1})_y}{\partial x} \right)_N \end{bmatrix}_{N \times 1} \quad (2.59)
\end{aligned}$$

and $\text{diag}(\bar{v})$ returns a square diagonal matrix with \bar{v} as the main diagonal. In (2.57), $\bar{\eta}$ is a vector composed of N scalar η values of all pixels in the imaged slice. The $\frac{1}{\Delta}$ coefficient, where Δ is the pixel size, is neglected because both sides of (2.57) have derivative terms that are computed with the same finite difference approach and the $\frac{1}{\Delta}$ coefficients of both sides cancel each other. Each entry of \bar{a}_1 , \bar{a}_2 and \bar{b} are obtained from the related pixel in the imaged slice.

The sum of each row of \bar{A} is exactly zero since both $\bar{\delta}_x$ and $\bar{\delta}_y$ have exactly two non-zero (1 and -1) entries at each row. Hence, \bar{A} has a zero eigenvalue and consequently exactly one non-zero vector in its null space, an all-one vector. Since (2.53) is a differential equation, obtaining a unique ECDR distribution is impossible unless additional information such as the absolute value of the solution in a pixel is available. In this study, a known ECDR value of a pixel in the background is utilized for this purpose. In brain imaging, for example, this prior information can be estimated utilizing the measured diffusion and approximate conductivity values of the cerebrospinal fluid (CSF) [120]. A row with only one non-zero element (equal to 1) is added to \bar{A} . The column of \bar{A} containing this non-zero element corresponds to the chosen background pixel. The natural logarithm of the known ECDR value of the chosen background pixel is inserted to the corresponding element in the right-hand-side of (2.57). Modified versions of $\bar{A}_{N \times N}$ and $\bar{b}_{N \times 1}$ are denoted as $\bar{A}'_{(N+1) \times N}$ and $\bar{b}'_{(N+1) \times 1}$. With this intervention, the new system of equations becomes full rank, and the solution gives the absolute ECDR distribution. Yet, the system of equations is still ill-posed, and regularization is needed for stable reconstructions. Hence, to solve the modified sys-

tems of equations, Total Variation (TV) regularized least-squares solution [121] is used with L-curve to choose the regularization parameter [119]:

$$\ln(\bar{\eta})_{N \times 1} = \underset{\ln(\bar{\eta})_{N \times 1}}{\operatorname{argmin}} \left\| \bar{A}'_{(N+1) \times N} \ln(\bar{\eta})_{N \times 1} - \bar{b}'_{(N+1) \times 1} \right\|_2^2 + \lambda \left\| \bar{L}_{2N \times N} \ln(\bar{\eta})_{N \times 1} \right\|_1 \quad (2.60)$$

Here, $\bar{L}_{2N \times N}$ is the discretized differential operator formed assuming periodic boundary conditions, and λ is the regularization parameter.

TV regularization also is preferred because of its edge-preserving nature. The regularization term in (2.60) is 1-norm of the gradient of the solution vector. The minimization problems where 1-norm of the solution is penalized are well known for their sparsity enforcing property. Moreover, due to having a sparse gradient, the solution becomes piecewise constant. This property acts as a denoising procedure, especially in the large constant regions, like the background of the numerical and experimental phantoms in this study [121]. Under low SNR conditions, modifying $\bar{A}_{N \times N}$ with the value of a pixel may create problems. In such a case, enforcing the mean value of a smooth region to be equal to the known ECDR value is a more stable approach if such a region with prior knowledge is available in the imaging slice [31].

2.4.2 Two current injection patterns

The systems of equations in (2.57) can be formed for each current injection pattern separately. Hence, for two independent current injection patterns, the following systems of the equations can be formed accordingly:

$$\bar{A}_{1(N \times N)} \ln(\bar{\eta})_{N \times 1} = \bar{b}_{1(N \times 1)} \quad (2.61)$$

$$\bar{A}_{2(N \times N)} \ln(\bar{\eta})_{N \times 1} = \bar{b}_{2(N \times 1)} \quad (2.62)$$

In (2.61) and (2.62), the unknown vectors are the same; therefore, the two systems of equations can be concatenated as:

$$\begin{bmatrix} \bar{A}_1 \\ \bar{A}_2 \end{bmatrix} \ln(\bar{\eta})_{N \times 1} = \begin{bmatrix} \bar{b}_1 \\ \bar{b}_2 \end{bmatrix} \quad \equiv \quad \bar{A}_{12(2N+1) \times N} \ln(\bar{\eta})_{N \times 1} = \bar{b}_{12(2N \times N)} \quad (2.63)$$

Again, $\overline{\overline{A}}_{12}$ is one less than full rank and can be modified similar to the single current injection case with the information of a known pixel in the ECDR distribution. The resulting modified system can be solved again with TV regularization as:

$$\ln(\overline{\eta})_{N \times 1} = \underset{\ln(\overline{\eta})_{N \times 1}}{\operatorname{argmin}} \left\| \overline{\overline{A}}'_{12(2N+1) \times N} \ln(\overline{\eta})_{N \times 1} - \overline{\overline{b}}'_{12(2N+1) \times 1} \right\|_2^2 + \lambda \left\| \overline{\overline{L}}_{2N \times N} \ln(\overline{\eta})_{N \times 1} \right\|_1 \quad (2.64)$$

2.4.3 Adaptive regularization based on the current density distribution

As seen from (2.53), the reconstructed ECDR distribution is a function of $\overline{\overline{D}}^{-1} \overline{\overline{J}}$ distribution. The main assumption behind this derivation is that the current density distribution is solely dependent on the conductivity distribution of the medium. Although this is true for most of the regions, due to the geometry of the medium and utilization of the current injection electrodes, current density values may become very high in regions close to the current injection electrodes. This situation results in the overestimation of the reconstructed ECDR and, consequently, the conductivity values in these regions. To compensate for this overestimation, an adaptive regularization scheme is proposed in this study. Let $\overline{\overline{J}}_{p_i}^R$ be an $N \times 1$ vector whose elements are the reciprocals of the magnitude of the projected current density at each pixel for the i^{th} current injection pattern. Hence, a diagonal weight matrix can be defined using $\overline{\overline{J}}_{p_i}^R$ as:

$$\overline{\overline{W}}_{(N+1) \times (N+1)} = \operatorname{diag} \left(\begin{bmatrix} \overline{\overline{J}}_{p_i}^R \\ 1 \end{bmatrix} \right) \quad (2.65)$$

The regularized least-squares solution in (2.60) can be rewritten as:

$$\ln(\overline{\eta})_{N \times 1} = \underset{\ln(\overline{\eta})_{N \times 1}}{\operatorname{argmin}} \left\| \overline{\overline{W}} \left(\overline{\overline{A}}'_{(N+1) \times N} \ln(\overline{\eta})_{N \times 1} - \overline{\overline{b}}'_{(N+1) \times 1} \right) \right\|_2^2 + \lambda \left\| \overline{\overline{L}}_{2N \times N} \ln(\overline{\eta})_{N \times 1} \right\|_1 \quad (2.66)$$

Similarly, $\overline{\overline{W}}_{12(2N+1) \times (2N+1)}$ can be defined as:

$$\overline{\overline{W}}_{12(2N+1) \times (2N+1)} = \operatorname{diag} \left(\begin{bmatrix} \overline{\overline{J}}_{p_1}^R \\ \overline{\overline{J}}_{p_2}^R \\ 1 \end{bmatrix} \right) \quad (2.67)$$

This results in the following regularized least-squares solution for the two current injection case:

$$\ln(\bar{\eta})_{N \times 1} = \underset{\ln(\bar{\eta})_{N \times 1}}{\operatorname{argmin}} \left\| \bar{W}_{12} \left(\bar{A}'_{12(2N+1) \times N} \ln(\bar{\eta})_{N \times 1} - \bar{b}'_{12(2N+1) \times 1} \right) \right\|_2^2 + \lambda \left\| \bar{L}_{2N \times N} \ln(\bar{\eta})_{N \times 1} \right\|_1 \quad (2.68)$$

As both sides of the linear system of equations are multiplied with the same coefficient, the equalities do not change. The main idea here is that the relative effect of each equation in the least-squares term is modified. Since a single regularization parameter is utilized, each equation is affected by the regularization differently. Strictly speaking, the pixels near the current injection electrodes are regularized stronger, which suppresses the overestimated reconstructions in the regions where the current density values are high due to current injection by the surface electrodes [31].

The proposed methods using dual and single current injections are evaluated using the simulated data and the experimental results acquired from biological tissue phantoms and the results are reported in Section 3.2.

2.4.4 The Simulation Model for the Numerical Evaluation of the Proposed Dual and Single Current DT-MREIT

In order to evaluate the performance of the proposed reconstruction methods using dual and single current injections, a FE model shown in Figure 2.3 is constructed using AC/DC Module of COMSOL Multiphysics® software [122]. Conductivity and diffusion values of different regions of the FE model are given in Table 2.2. The true ECDR distribution of the simulation model is shown in Figure 2.4.

2.4.5 Imaging Phantoms and Pulse Sequence Parameters for Experimental Evaluation of the Proposed Dual and Single Current DT-MREIT

Two biological tissue phantoms are used for the experimental data acquisition of the proposed dual and single current DT-MREIT methods. The first phantom (Ph 1) is a 3D Plexiglas container shown in Figure 2.1(a) with the dimensions same as the FE model in Figure 2.3. Ph 1 is filled with a saline solution having conductivity and T_2

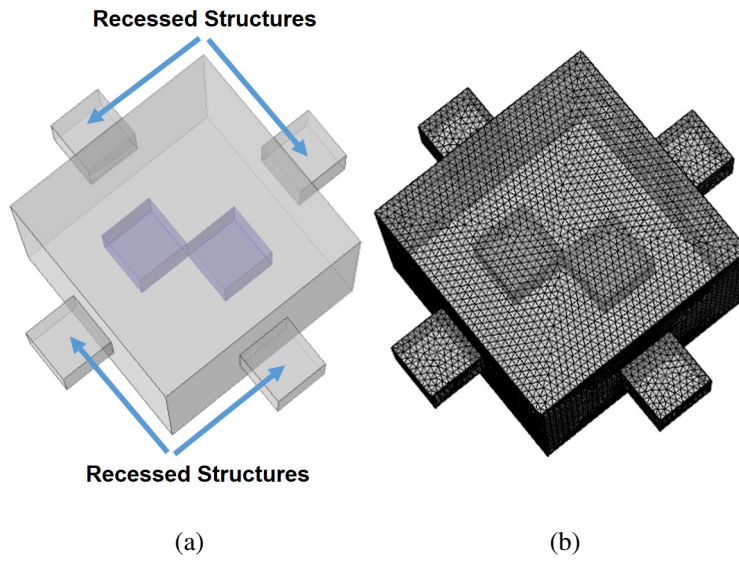


Figure 2.3: (a) The cubic FE model, and (b) its mesh structure. The FE model is composed of a cube with the dimensions of $80 \times 80 \times 80 \text{ mm}^3$ and four recessed structures, each with the dimensions of $20 \times 20 \times 20 \text{ mm}^3$ for placement of the current injection electrodes. Two inhomogeneities with the dimensions of $20 \times 20 \times 20 \text{ mm}^3$ are placed at the middle slice of the model. The FE model is composed of 122838 domain, 7772 boundary, and 583 edge elements, and it is solved for 965805 degrees of freedom.

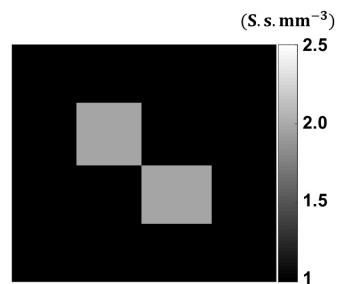


Figure 2.4: The true ECDR distribution in the mid-slice of the simulation model in Figure 2.3 considering the \bar{C} and \bar{D} values in Table 2.2.

Table 2.2: Parameters of the FE model in the background and in the left and right inhomogeneities. σ_{xx} , σ_{yy} , σ_{zz} and d_{xx} , d_{yy} , d_{zz} are the main diagonal components of \overline{C} and \overline{D} , respectively.

Parameter	Background	Left inhom.	Right inhom.
σ_{xx} (S m^{-1})	0.45	0.3	0.2
σ_{yy} (S m^{-1})	0.45	10.2	0.3
σ_{zz} (S m^{-1})	0.45	0.18	0.18
d_{xx} ($\text{mm}^2 \text{s}^{-1}$)	45	15	10
d_{yy} ($\text{mm}^2 \text{s}^{-1}$)	45	10	15
d_{zz} ($\text{mm}^2 \text{s}^{-1}$)	45	9	9

values of 0.5 S m^{-1} and $\sim 180 \text{ ms}$, respectively, which are the mean conductivity (for the frequencies less than 40 Hz) and the T_2 values of the human blood [123, 124]. Two pieces of chicken muscle, each with the dimensions of $20 \times 20 \times 20 \text{ mm}^3$ are placed inside the saline solution as anisotropic distributions using holder apparatus, as shown in Figure 2.5(a). The colored FA map and MD distributions of the Ph 1 are shown in Figure 2.5(b) and (c), respectively.

The second phantom (Ph 2), is a 3D Plexiglas container similar to Ph 1 but with the dimensions of $100 \times 100 \times 100 \text{ mm}^3$. Similar to Ph 1, Ph 2 is filled with a saline solution with the conductivity and relaxation parameters of the human blood. A piece of bovine muscle with the dimensions of $70 \times 70 \times 55 \text{ mm}^3$ is placed inside the phantom with the help of two mesh apparatus to mimic anisotropy, as shown in Figure 2.6(a)-(b).

The parameters of the SS-SE-EPI and ICNE-ME-FLASH pulse sequences are given in Tables 2.3 and 2.4, respectively.

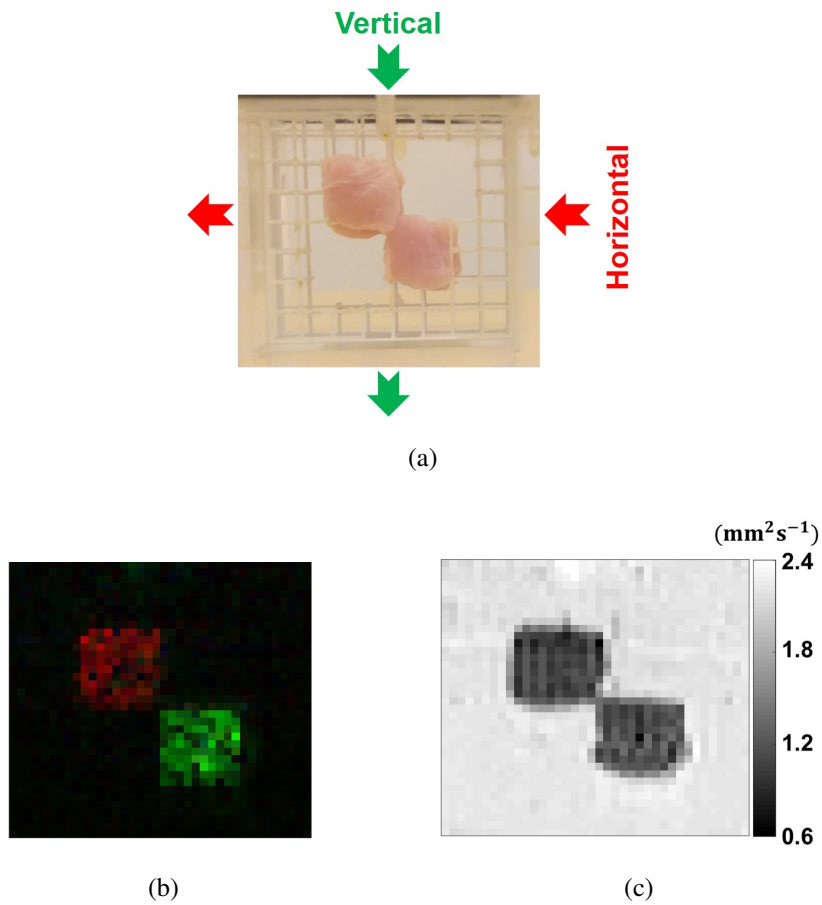


Figure 2.5: Ph 1 is filled with a saline solution and two chicken breast pieces are placed inside the phantom with the help of the holder apparatus to mimic anisotropy. (a) The imaging slice in the transversal (x-y) plane. The red and green arrows show the patterns of the injected currents. (b) The colored FA map of the imaging slice is obtained from the DT images of the experimental phantom. The red and green colors show that the main direction of diffusion for the left and right muscle pieces is in the x- and y- directions, respectively. (c) MD of the imaging slice. The relaxation parameters of the chicken muscle pieces measured as: $T_1 = 1200$ ms and $T_2^* = 20$ ms.

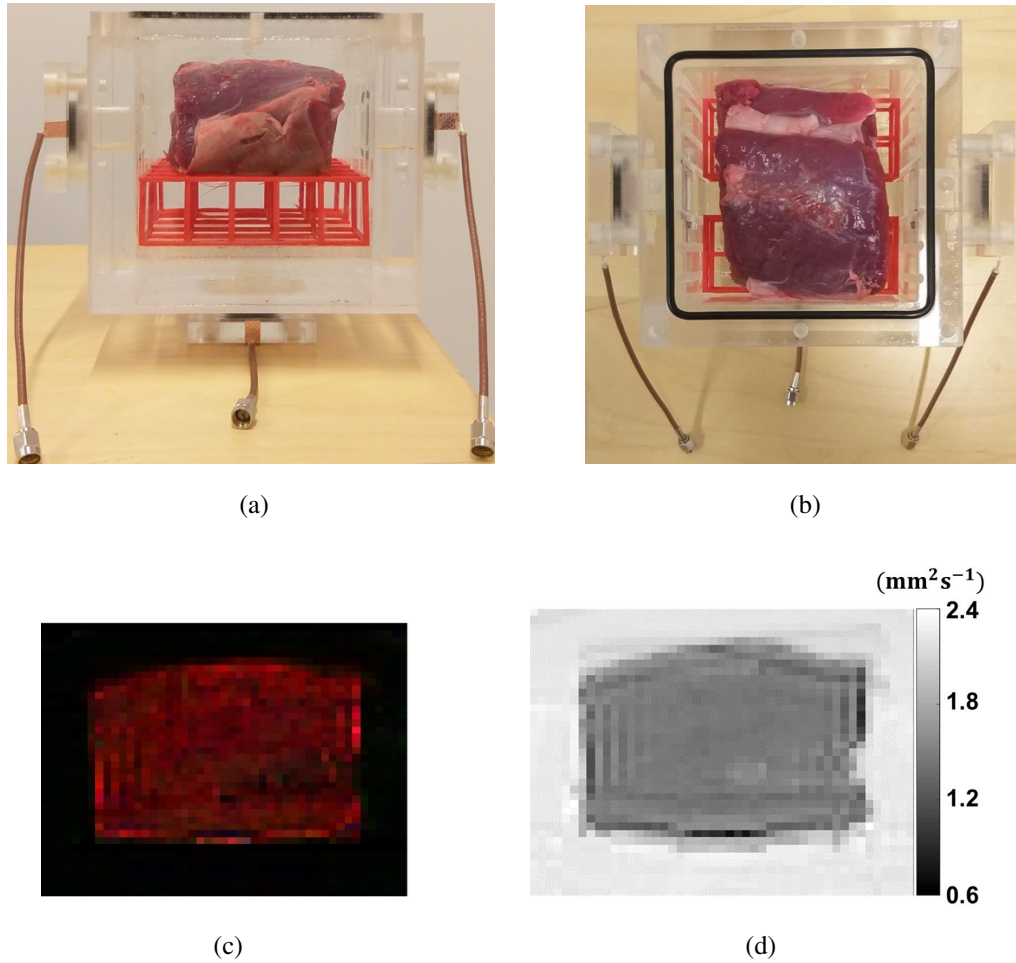


Figure 2.6: Ph 2 filled with a saline solution and a piece of bovine muscle is placed inside the container to mimic anisotropy. The red mesh structure is used to hold the muscle piece in the center of phantom. (a) The imaging slice in the transversal (x-y) plane. (b) Top view (x-z plane). (c) The colored FA map of the imaging slice. The red color shows that the main direction of diffusion (muscle fibers) is in the x-direction. (d) The MD of the imaging slice. The relaxation parameters of the muscle piece measured as: $T_1 = 1412$ ms and $T_2^* = 37$ ms.

Table 2.3: SS-SE-EPI pulse sequence parameters for DTI data acquisition of the Ph 1 and Ph 2.

Parameter	Ph 1	Ph 2
Field of View (FOV)	$128 \times 128 \text{ mm}^2$	$256 \times 256 \text{ mm}^2$
Number of Phase Encoding Steps (N_{PE})	64	128
Slice Thickness	5 mm	5 mm
Diffusion Encoding Directions (N_D)	64	32
b value	1000 s mm^{-2}	700 s mm^{-2}
T_R	3000 ms	3000 ms
T_E	86 ms	91 ms
Number of Averaging (N_{EX})	2	1
BW	1532 Hz/pixel	2170 Hz/pixel
Total Scan Time ($T_R \times N_D \times N_{EX} \times 2^*$)	768 s	192 s

* The DW data is acquired two times with opposing polarities of the phase encode blips for geometric distortion correction.

2.5 MHD Flow Imaging

MHD flow is a phenomenon that emerges inside the conductive fluids as a result of interaction between the current density and the magnetic field, which are orthogonal to each other. For instance, in MRCDI experiments, an electrical current is injected into the imaging medium. The \bar{J} distribution creates a Lorentz force density (\bar{F}) distribution by interacting with the static magnetic field of the MR scanner (B_0) as:

$$\bar{F} = \bar{J} \times B_0 \bar{k} = \sigma(\bar{E} + \bar{v} \times B_0 \bar{k}) \times B_0 \bar{k} \quad (2.69)$$

where $\bar{J} = \sigma(\bar{E} + \bar{v} \times B_0 \bar{k})$ is the current density of a moving fluid with a velocity of \bar{v} . \bar{E} is the electric field and σ is the electrical conductivity. \bar{k} is the unit vector in the z-direction. \bar{F} moves the fluid and the MHD flow velocity (\bar{v}) satisfies Navier–Stokes equation [83]:

$$\rho \left(\frac{\partial \bar{v}}{\partial t} + \bar{v} \cdot \nabla \bar{v} \right) = \nabla p + \mu \nabla^2 \bar{v} + \bar{F} \quad (2.70)$$

where ρ is the fluid density, p is the pressure field of the domain, and μ is the dynamic viscosity of the medium. For incompressible fluids, the equation of continuity can be

Table 2.4: ICNE-ME-FLASH pulse sequence parameters for MRCDI data acquisition of the Ph 1 and Ph 2.

Parameter	Ph 1	Ph 2
Field of View (FOV)	$128 \times 128 \text{ mm}^2$	$256 \times 256 \text{ mm}^2$
Number of Phase Encoding Steps (N_{PE})	64	128
Slice Thickness	5 mm	5 mm
Number of Echoes (N_E)	9	9
Current Injection Duration (T_C)	50 ms	63 ms
T_R	560 ms	540 ms
T_E^1	7.6 ms	20.5 ms
T_E^9	50 ms	63 ms
Echo Spacing	5.3 ms	5.3 ms
Flip Angle α	53°	37°
Number of Averaging (N_{EX})	16	12
BW	200 Hz/pixel	200 Hz/pixel
Total Scan Time ($T_R \times N_{PE} \times N_{EX} \times 2^*$)	1147 s	1659 s
SNR level (K)	2	1.5

* For each current pattern, the \tilde{B}_z^j are acquired with the positive and negative current injection polarities in order to remove the systematic phase artifacts.

expressed as [125]:

$$\nabla \cdot \bar{v} = 0 \quad (2.71)$$

In order to solve (2.70) and (2.71) in an enclosed body the boundary condition no-slip and open boundary conditions are used as:

$$\bar{v} = 0 \quad \text{and} \quad f_0 = 0 \quad (2.72)$$

where f_0 is the normal stress on the boundaries. In fluid mechanics, the no-slip boundary condition for viscous fluids at a solid boundary is that the fluid will have zero velocity immediately in contact with the solid boundary [126]. The no-slip boundary condition can be thought of as a Dirichlet boundary condition. The MHD flow information can be encoded in the form of phase components to the MR complex signal using flow encoding gradients. The MR complex signal in the presence of MHD

flow information is explained in Section 2.6. The principles of MHD flow imaging is explained in [83].

During MRCDI experiments of fluids with low dynamic viscosity, the interaction between the injected current with MR scanner B_0 results in MHD flow velocity inside the object. Since, in the implemented ICNE-ME-FLASH pulse sequences, there are no flow encoding gradients, MHD flow does not contribute directly to the acquired signal. However, the indirect effect of MHD flow, which causes movement of the fluid particles, must be considered on the acquired \tilde{B}_z and \bar{J} data.

To investigate the effect of MHD flow velocity (\bar{v}) on the acquired \tilde{B}_z distributions in the absence of flow encoding gradients during MRCDI experiments, a FE model with the geometry, dimensions and the boundary conditions similar to the experimental phantom in Figure 2.1 is constructed using COMSOL Multiphysics® software [122] as shown in Figure 2.7.

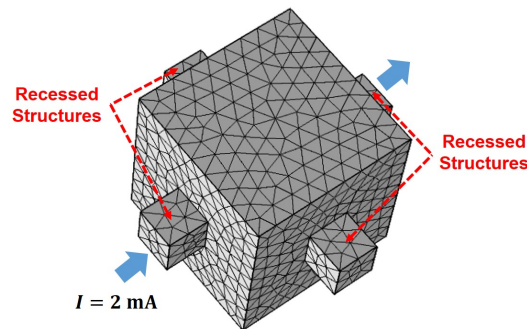


Figure 2.7: The FE model of the experimental phantom with the dimensions of $80 \times 80 \times 80$ and four recessed structures with the dimensions of $20 \times 20 \times 20$. The FE model is composed of 10906 tetrahedral, 3472 prism, 1624 triangular, and 240 edge elements. The open boundary condition is applied for the phantom's top surface, and the no-slip boundary condition is applied for the remaining surfaces. The laminar flow model is solved for a maximum step size of 1 ms.

2.6 The Proposed Multi-Contrast Imaging Pulse Sequence

A DW-SE based pulse sequence with simultaneous current injection (Figure 2.8) is proposed to combine DTI, MRCDI, and the MHD flow data acquisitions to acquire \overline{D} , B_z , \overline{J} , \overline{v} and \overline{C} , simultaneously. DW-SE pulse sequence can provide high-quality, high-resolution DW images with minimal artifacts [127] without the need for post-processing corrections required for DW-EPI pulse sequence as explained in Section 2.3.

The current is applied in the interval between the end of 90° RF pulse and the beginning of the flow encoding gradient to avoid slice distortions because of current injection during RF excitation and avoid disruption of the linearity of flow encoding gradients.

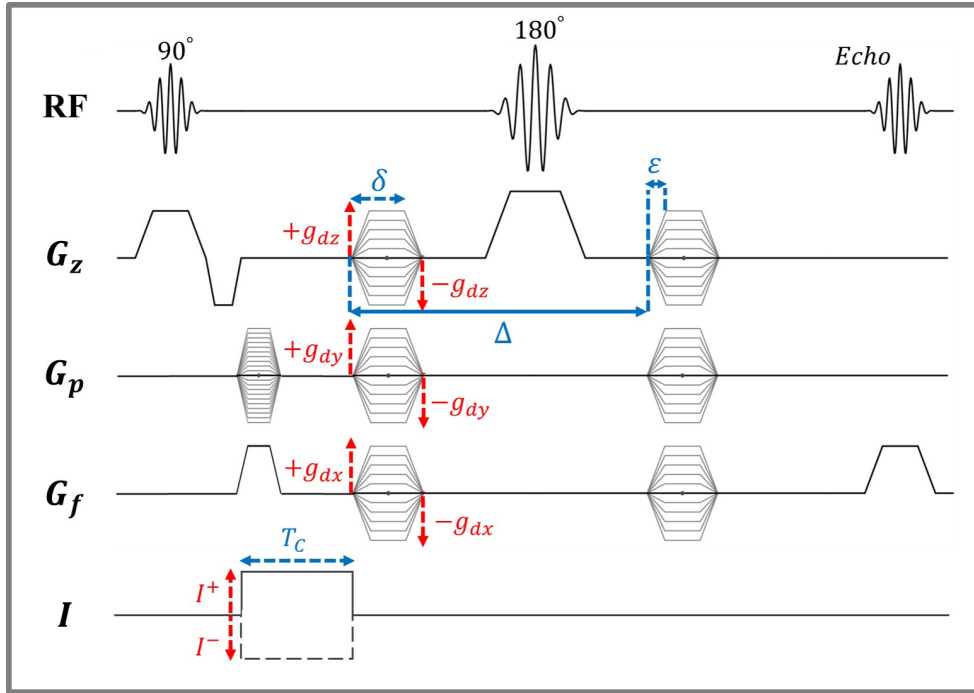


Figure 2.8: The schematic diagram of the DW-SE multi-contrast pulse sequence with simultaneous current injection. g_d 's are the magnitudes of the diffusion encoding gradients. I and T_C are the amplitude and the duration of the injected current, respectively. Δ , δ and ϵ are defined in Section 1.3. G_z , G_p and G_f are the slice selection, phase encoding, and frequency encoding gradients, respectively.

Note that the water molecules' self-diffusion is the random translational motion of molecules due to their thermal energy. This kind of random motion (also is called Brownian motion) can be classified as a zero-mean, and consequently, incoherent motion. Therefore, the diffusion information is acquired from the MR magnitude images. On the other hand, the MHD flow can be considered a coherent (zero-variance) motion that does not affect the MR magnitude images. Therefore, the effects of encoding mechanisms of coherent and incoherent motions in the MR signal are fundamentally different even though both processes are encoded with the application of the same motion-sensitizing (flow or diffusion encoding) gradients.

The MR signal of the proposed pulse sequence in Figure 2.8 can be expressed as:

$$S_k = S_0 e^{-b\bar{g}_{d_k}\bar{D}\bar{g}_{d_k}^T} e^{-j(\phi_I + \phi_{g_d} + \phi_{MHD_{g_d}} + \phi_{MHD_{g_r}} + \phi_0)} \quad \text{for } k = 1 \dots N_D \quad (2.73)$$

where S_k is the MR signal obtained by applying the diffusion encoding gradient $\bar{g}_{d_k} = g_{d_k}[u_k \ v_k \ w_k]$. u , v and w are the direction cosines of the diffusion gradient vector. ϕ_I is the accumulated phase due to the current-induced B_z and ϕ_{g_d} is the phase component due to the diffusion-encoding gradient application. $\phi_{MHD_{g_d}}$ and $\phi_{MHD_{g_r}}$ are the MHD-based phase components encoded to the MR signal by diffusion-encoding and imaging gradients, respectively. ϕ_0 is related to the systematic phase artifacts. N_D is the total number of diffusion-encoding directions and b -value is introduced in (1.5).

To successfully reconstruct \bar{D} , B_z and MHD flow from the MR signal in (2.73), the data is acquired two times with I^\pm in $k = 6$ diffusion encoding directions as:

$$\begin{bmatrix} u_k \\ v_k \\ w_k \end{bmatrix} = \begin{bmatrix} \frac{1}{\sqrt{2}} \\ 0 \\ \frac{1}{\sqrt{2}} \end{bmatrix}, \begin{bmatrix} \frac{-1}{\sqrt{2}} \\ 0 \\ \frac{1}{\sqrt{2}} \end{bmatrix}, \begin{bmatrix} \frac{1}{\sqrt{2}} \\ \frac{1}{\sqrt{2}} \\ 0 \end{bmatrix}, \begin{bmatrix} \frac{1}{\sqrt{2}} \\ \frac{-1}{\sqrt{2}} \\ 0 \end{bmatrix}, \begin{bmatrix} 0 \\ \frac{1}{\sqrt{2}} \\ \frac{1}{\sqrt{2}} \end{bmatrix}, \begin{bmatrix} 0 \\ \frac{1}{\sqrt{2}} \\ \frac{-1}{\sqrt{2}} \end{bmatrix} \quad (2.74)$$

Furthermore, two sets of data must be acquired with I^\pm and without applying diffusion-encoding gradients to be used in the reconstruction of \bar{D} and B_z . \bar{D} can be reconstructed at each voxel from the DW images of exactly six diffusion encoding directions as given in (1.9). The MHD flow distribution can be reconstructed as:

$$\phi_{MHD_{g_d}} = \frac{\arg(S_k^{I^+, \bar{g}_d^+}) - \arg(S_k^{I^-, \bar{g}_d^+}) - \arg(S_k^{I^+, \bar{g}_d^-}) + \arg(S_k^{I^-, \bar{g}_d^-})}{4} \quad (2.75)$$

where $S_k^{I^\pm, \bar{g}_d^\pm}$ denotes the signal obtained using opposing polarities of I and \bar{g}_d . $\arg(\cdot)$ includes any necessary phase unwrapping. By extracting $\phi_{MHD_{g_d}}$ from the MR complex signal the relation between $\phi_{MHD_{g_d}}$ and \bar{v} distribution can be derived as:

$$\phi_{MHD_{g_d}} = \gamma \Delta \delta (\bar{g}_{d_k} \cdot \bar{v}) \quad (2.76)$$

where Δ and δ are defined in Section 1.3. Therefore, \bar{v} information in the direction of \bar{g}_{d_k} can be computed from $\phi_{MHD_{g_d}}$.

The current-induced B_z distribution can be reconstructed from the phase images of the measurements with I^\pm but without flow encoding gradients as:

$$B_z = \frac{\arg(S^{I^+}) - \arg(S^{I^-})}{2\gamma T_C} \quad (2.77)$$

The projected current density \bar{J}_p can be estimated as explained in Section 2.2. Finally, \bar{C} can be reconstructed from the measured \bar{D} and estimated \bar{J}_p using the proposed DT-MREIT methods explained in Section 2.4.

The experimental data of the proposed multi-contrast pulse sequence in Figure 2.8 is acquired using the biological tissue phantom in Figure 2.9 with parameters given in Table 2.5 and the results are reported in Section 3.3.

2.6.1 Imaging Phantom and Pulse Sequence Parameters for Experimental Evaluation of the Proposed Multi-Contrast Imaging

The experimental phantom is the 3D Plexiglas container in Figure 2.1(a) filled with a saline solution with the conductivity and T_2 values of 0.5 S/m and ~ 200 ms, respectively. Two bovine muscle pieces with the dimensions of $30 \times 25 \times 30$ mm³ and $25 \times 25 \times 30$ mm³ are placed inside the saline solution with the help of a holder apparatus to mimic anisotropy, as shown in Figure 2.9. The solution contains 3.75 g/L NaCl and 6.3 mg/L MnCl₂ dissolved in pure water. The current is injected in vertical and horizontal directions.

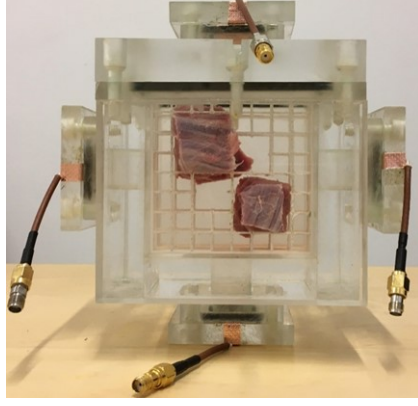


Figure 2.9: The experimental phantom for multi-contrast data acquisition filled with a saline solution and two pieces of bovine muscle are placed inside the saline solution with the help of a holder apparatus to mimic anisotropy.

Table 2.5: Multi-contrast imaging pulse sequence parameters.

Parameter	Value
Field of View (FOV)	$128 \times 128 \text{ mm}^2$
Number of Phase Encoding Steps (N_{PE})	64
Slice Thickness	5 mm
T_R	1000 ms
T_E	75 ms
Δ	34 ms
δ	14 ms
g_d	35 mT/m
b value	500 s mm^2
Current Injection Duration (T_C)	10 ms
Current Amplitude (I)	10 mA
Number of Averaging (N_{EX})	1
BW	200 Hz/pixel
Total Scan Time ($T_R \times N_{PE} \times N_{EX} \times 14^*$)	896 s

* The total of 14 data is acquired. 12 with I^\pm in the six diffusion encoding directions given in (2.74) and 2 data with I^\pm and without diffusion encoding gradients.

CHAPTER 3

THE RESULTS OF THE PROPOSED METHODS USING ANALYTICAL MODELINGS, NUMERICAL SIMULATIONS AND PHANTOM EXPERIMENTS

In this chapter, the proposed methods in Chapter 2 are validated using numerical simulations and experimentally acquired data. The results of the proposed SNR and total acquisition time analysis of the ICNE-FLASH and ICNE-ME-FLASH pulse sequences for the analytical modeling and the saline-filled experimental phantom are given in Section 3.1. Also, the effect of intensive utilization of gradients during MRCDI experiments using ICNE-ME-FLASH pulse sequence is measured using a saline-filled imaging phantom. In the second part, the ECDR and \overline{C} distributions of a numerical model and two biological tissue phantoms are reconstructed using the proposed single and dual current DT-MREIT methods, and results are reported in Section 3.2. Finally, in the last part, the experimental results of the proposed multi-contrast imaging pulse sequence using a biological tissue phantom are given in Section 3.3.

3.1 SNR and the Total Data Acquisition Time Analysis of the measured \tilde{B}_z

In this section, the proposed SNR and total acquisition time analysis in Section 2.1 for ICNE-ME-FLASH pulse sequence is evaluated using the analytical and experimental data and the acquired results are reported. The methods proposed in Section 2.1 and the results reported in this section are presented in [128, 129].

3.1.1 The Analytical Modeling Results

In all analytical modelings, the relaxation parameters of the human brain WM is used. The approximate relaxation times (T_1 , T_2 and T_2^*) and the proton density ρ_0 for several biological tissues at 3 T are given in Table 3.1 [130–133].

Table 3.1: The approximate relaxation times and the proton density for several biological tissues at 3 T.

Tissue	T_1	T_2	T_2^*	ρ_0
Brain White Matter (WM)	1080	70	50	0.61
Brain Gray Matter (GM)	1850	100	50	0.69
Skeletal Muscle	1412	50	20	0.60
Fat	250	60	35	0.10
Arterial Blood	1932	275	46	0.72
CSF	3817	1422	-	1

3.1.1.1 The Analytical Modelling Results for ICNE-FLASH Pulse Sequence

By maximizing the SNR level function in (2.6) with respect to T_C , the maximum SNR level is achieved when $T_C = T_2^*$. Clearly, for all biological tissues, the optimum T_C value providing the highest SNR level using the ICNE-FLASH sequence is equal to T_2^* of that tissue. Hence, for a single echo FLASH pulse sequence, the effect of other parameters (i.e., T_R , N_{EX} and α) is investigated assuming $T_C = T_2^*$.

The SNR level functions of the acquired \tilde{B}_z for different T_R and α values for a single excitation ($N_{EX} = 1$) are calculated using (2.6) for ICNE-FLASH and shown in Figure 3.1.

The results for the total acquisition time per each phase encoding step ($T_{Total}/N_{PE} = T_R \times N_{EX}$) obtained using (2.10) for different α , N_{EX} and $K = 0.5, 1$, and 2 are shown in Figure 3.2. All points in Figure 3.2(a) have the same SNR value of $\xi_{\tilde{B}_z}^{max}$. The three points specified as (I), (II) and (III) have the same SNR and almost same

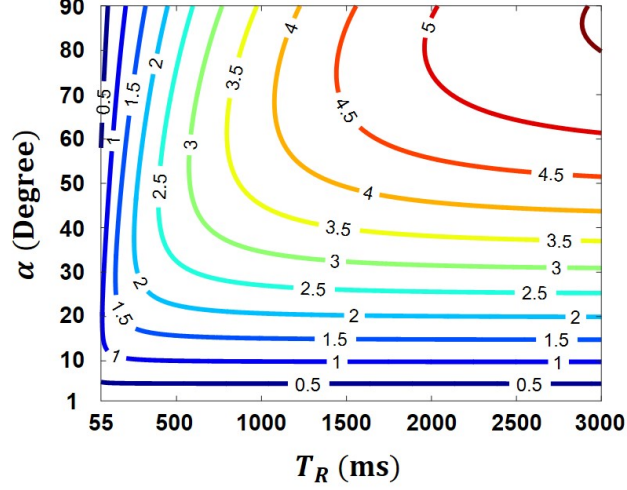


Figure 3.1: Contour plot of the calculated $\xi_{\tilde{B}_z}$ for different T_R and α values of ICNE-FLASH pulse sequence considering the relaxation parameters of the WM and $T_C = T_2^*$.

T_{Total}/N_{PE} but different T_R , N_{EX} and α values. Similarly, all the points in Figure 3.2(b) for $K = 0.5$ have the same SNR value of $0.5\xi_{\tilde{B}_z}^{max}$ and the parameter set points (IV), (V) and (VI) also have the almost same T_{Total}/N_{PE} while their T_R , N_{EX} and α values are different.

As seen in Figure 3.2(a), for $\alpha = 10^\circ$, $\xi_{\tilde{B}_z}^{max}$ cannot be achieved for $N_{EX} \leq 32$. From Figure 3.2(b) with $K = 0.5$, the SNR level of $0.5\xi_{\tilde{B}_z}^{max}$ is achievable by $\alpha = 10^\circ$ which is not the case for $K = 1$. On the other hand, for $K = 2$, the SNR level of $2\xi_{\tilde{B}_z}^{max}$ is not achievable even by $\alpha = 20^\circ$ for $N_{EX} \leq 32$.

T_{Total}/N_{PE} versus N_{EX} for different K values is given in Figure 3.3(a). In this plot, the values of T_R and α are estimated using (2.10) and (2.13), respectively. As seen in Figure 3.3(a), the minimum acquisition time is achieved when $N_{EX} = N_{EX}^{max}$. However, excessive number of averaging can cause spatial and temporal variations of the main magnetic field, a remarkable temperature increase due to eddy current heating of the RF shield, and temperature elevation in the metallic prosthesis, as mentioned in Section 2.1.5. Particularly, in MRCDI experiments, using high N_{EX} results in a more electrical current exposure of the tissue which is not desirable.

The minimum time angle (α_t) calculated using (2.13) for the three K values and

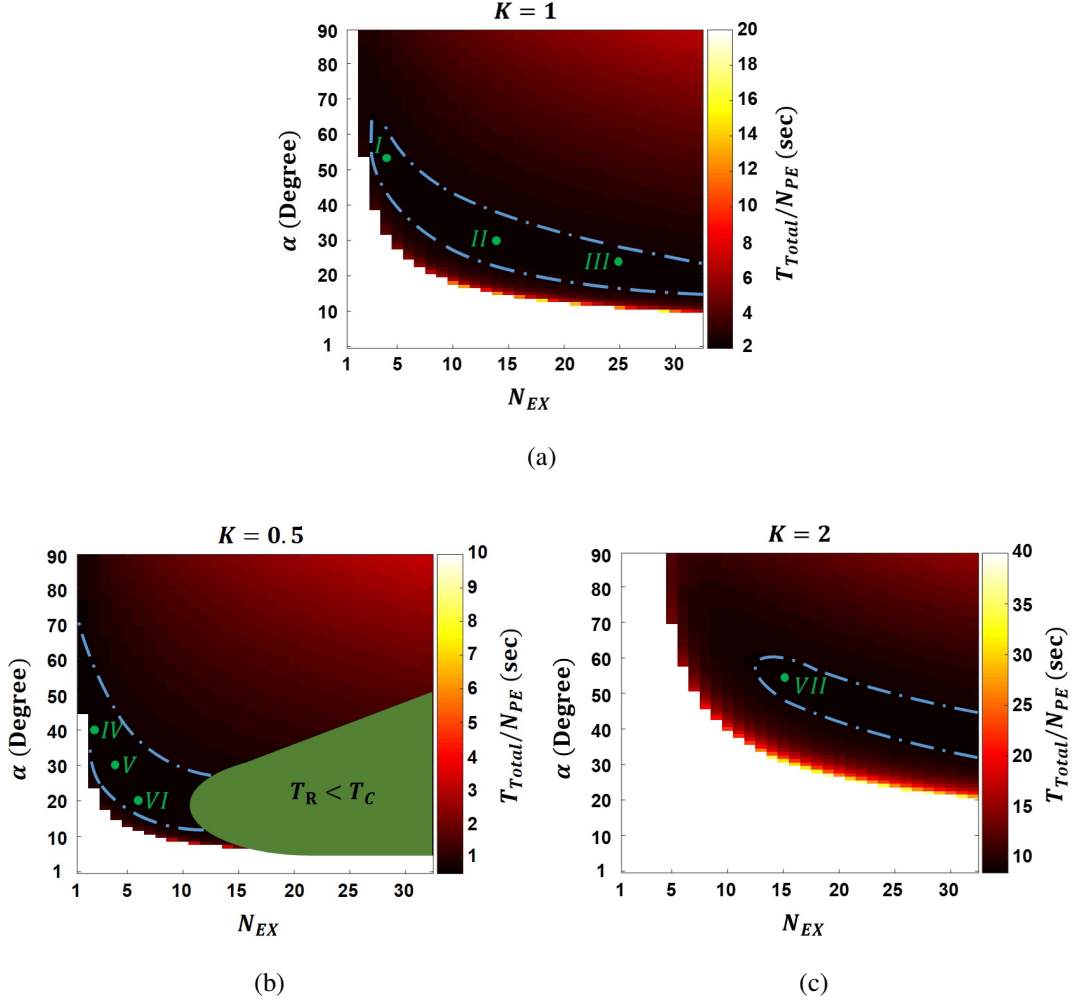


Figure 3.2: Different sets of T_R , N_{EX} and α to acquire \tilde{B}_z images with the SNR level of (a) $\xi_{\tilde{B}_z^{max}}$ ($K = 1$), (b) $0.5\xi_{\tilde{B}_z^{max}}$ ($K = 0.5$), (c) $2\xi_{\tilde{B}_z^{max}}$ ($K = 2$) using ICNE-FLASH pulse sequence. The regions inside the dashed lines have almost the same total acquisition time per each phase encoding step T_{Total}/N_{PE} . $T_C = T_2^* = 50$ ms to maximize the SNR level of the acquired \tilde{B}_z and the condition $T_R \geq T_C$ holds for all calculations. The green region in (b) shows the parameter sets with $T_R < T_C$. The points (I) – (VII) are used in experimental data acquisition for $K = 0.5, 1, 2$.

different N_{EX} are shown in Figure 3.3(b). It can be said that, for a given N_{EX} , the α_t gives the flip angle that provides the shortest T_{Total} to achieve $K\xi_{\tilde{B}_z}^{max}$. By choosing N_{EX} and calculating α_t accordingly, T_R can be calculated using (2.10). Combining (2.10) and (2.13), $\min T_{Total}/N_{PE}$ versus K is shown in Figure 3.3(c). The minimum total acquisition time for the desired SNR level or the highest SNR level that can be

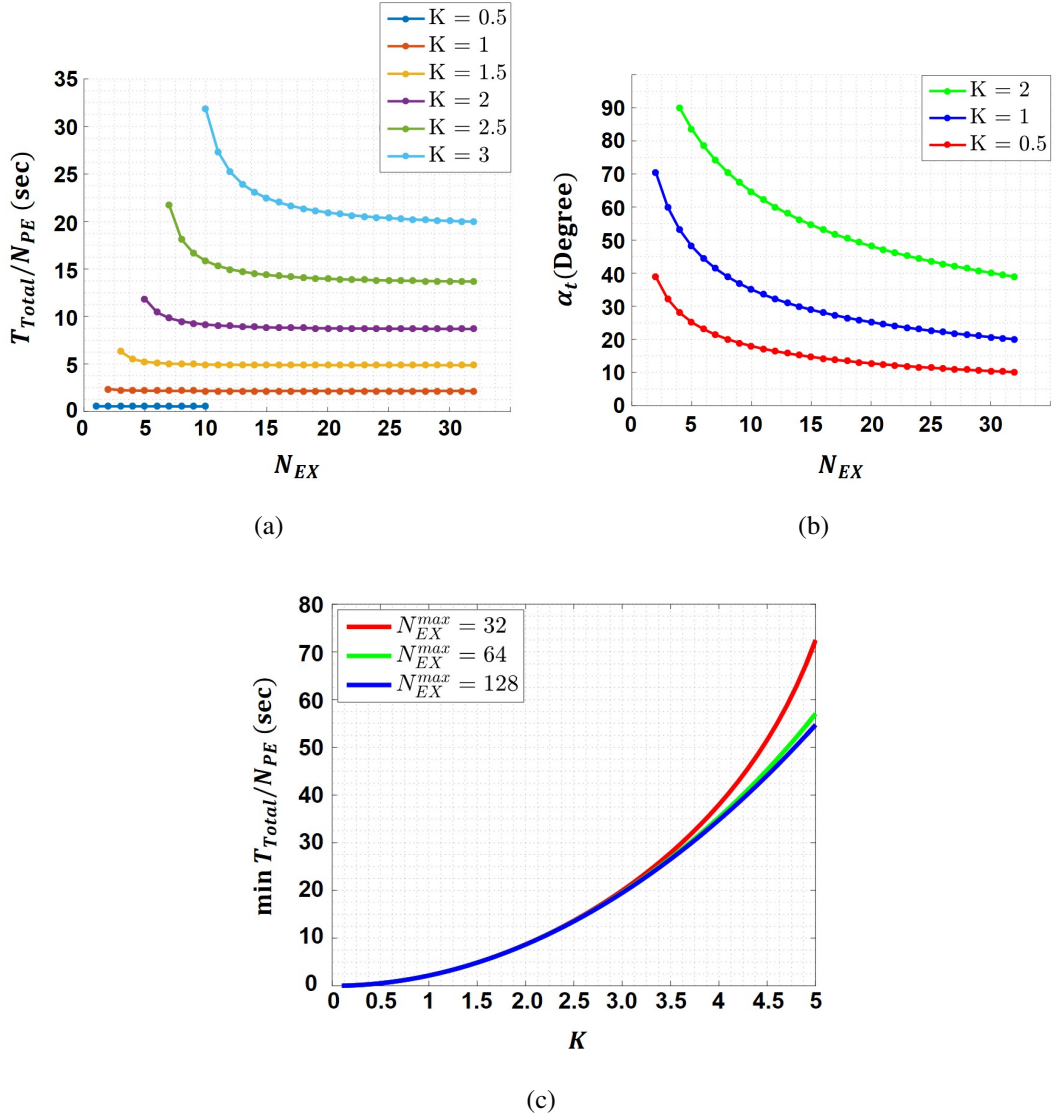


Figure 3.3: (a) T_{Total}/N_{PE} versus N_{EX} for different K values. (b) The α_t versus N_{EX} for $K = 0.5, 1, 2$. Each α_t gives the flip angle providing the shortest T_{Total} to achieve $K\xi_{\tilde{B}_z}^{max}$ for a specific N_{EX} . (c) The minimum total time per phase encoding ($\min T_{Total}/N_{PE}$) versus K for three different N_{EX}^{max} .

achieved in a given total time can be estimated using Figure 3.3(c). By estimating the $s_{\tilde{n}}$ of the measured \tilde{B}_z using (2.28)-(2.31) K in Figure 3.3(c) can be scaled by the estimated $\xi_{\tilde{B}_z}^{max}$ to estimate the absolute SNR value.

To summarize the findings in (2.10) and (2.13) and Figures 3.2-3.3, an algorithm is provided in Figure 3.4(a) to find the minimum acquisition time for an SNR level by

searching all possible N_{EX} . However, it is more convenient to look for suboptimal parameters that provide the same SNR level at almost the same acquisition time. This can be achieved by storing all the values computed using the algorithm in Figure 3.4(a) and evaluating the whole results. Another way is to define an SNR flexibility margin (e.g., 0.03 in the linear sense) and looking for the point(s) in this margin with a minimum N_{EX} value using the computed T_{min} value, as given in Figure 3.4(b). This approach especially can be used when lower N_{EX} values are preferred due to the reasons addressed above.

3.1.1.2 The Analytical Modelling Results for ICNE-ME-FLASH Pulse Sequence

The proposed SNR analysis for ICNE-FLASH is also valid for the ICNE-ME-FLASH pulse sequence except for optimal T_C . It is shown that, in the case of a single echo, the highest SNR of the \tilde{B}_z distribution is achieved when $T_C = T_2^*$. In the case of multiple echoes, the highest SNR level can be achieved by combining the multiple \tilde{B}_z distributions using the proper weights given in (2.14).

In Figure 3.5, the estimated relative noise standard deviation of the \tilde{B}_z^{comb} , $s_{\tilde{n}_w}$, for a range of total current injection duration T_C are shown for three different numbers of echos $N_E = 6, 9$ and 12 . The relative $s_{\tilde{n}_w}$'s of the \tilde{B}_z^{comb} distributions calculated for $N_E = 6, 9$ and 12 are minimized (the SNR is maximized) when the total current injection duration is $T_C = 65, 75$ and 86 ms, respectively. For a given N_E and ΔT the optimum T_C value provide the highest SNR in the \tilde{B}_z^{comb} distribution can be calculated by solving the polynomial in (2.26). Solving the polynomial in (2.26) for $N_E = 6, 9$ and 12 , and $\Delta T = 5.3$ ms gives the optimum values of $T_C = 65, 75$ and 86 ms, respectively. The other T_C^j values can be calculated as given in (2.27). Clearly, solving (2.26) for $N_E = 1$ (ICNE-FLASH), the optimum T_C gives the highest SNR for the measured \tilde{B}_z distribution is $T_C = T_2^*$.

In the experimental application of the ICNE-ME-FLASH sequence to maximize the SNR level of the acquired \tilde{B}_z images, a low readout gradient bandwidth (BW=200 Hz/pixel) is chosen considering the other imaging parameters, which results in $\Delta T = 5.3$ ms between the two consecutive echoes. Note that 0.3 ms time gaps are placed between successive echoes.

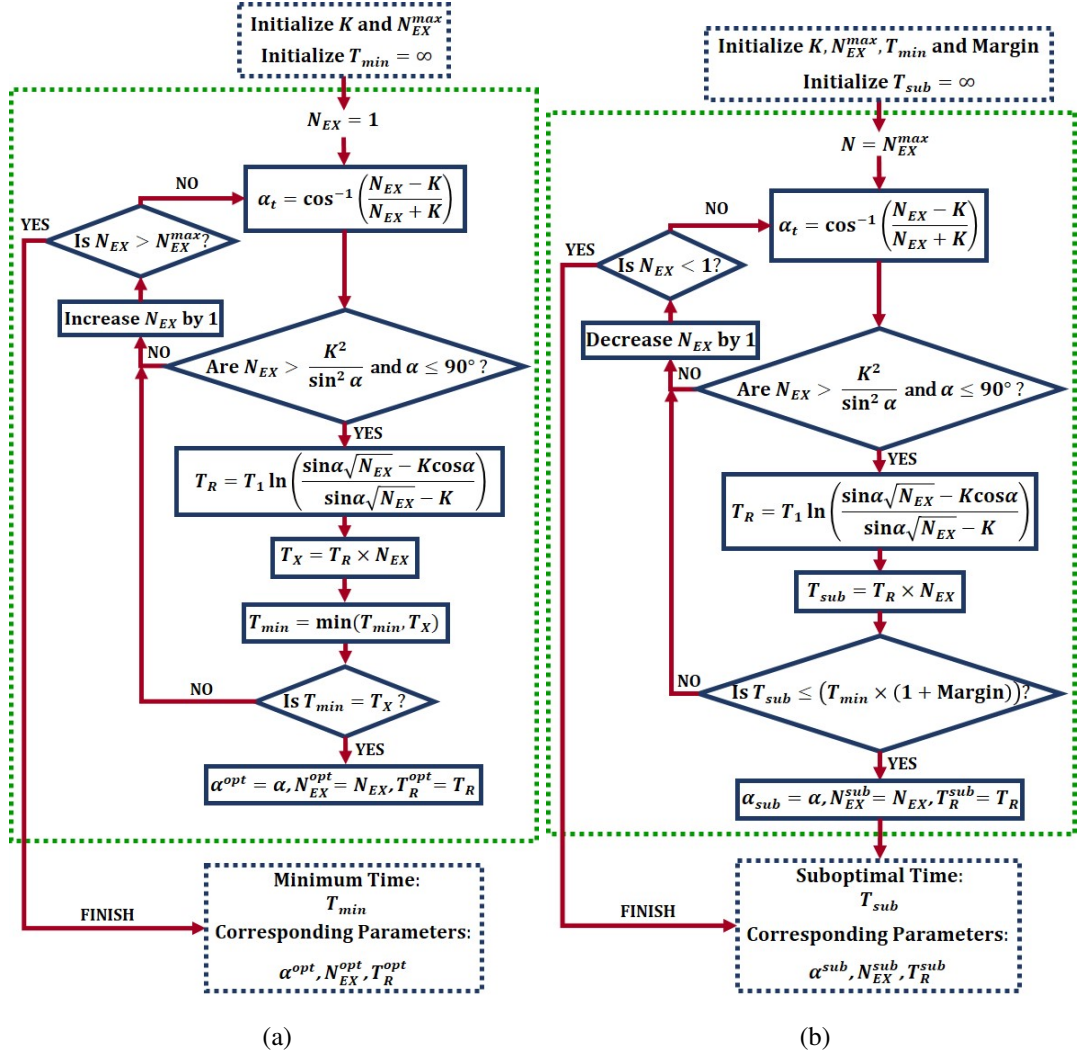
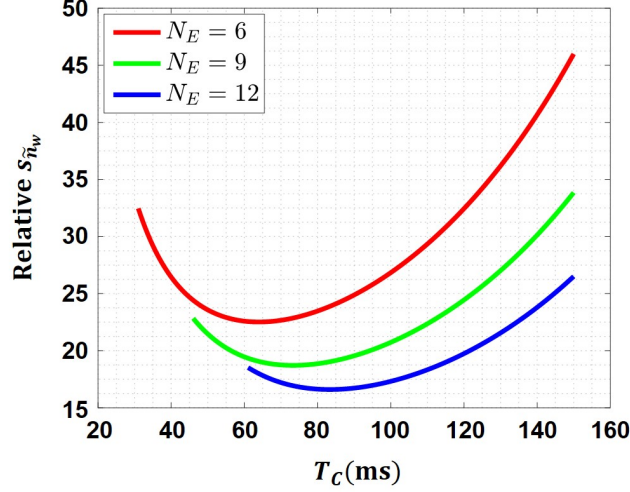


Figure 3.4: Flowcharts of the proposed parameter search algorithms. (a) The algorithm that finds the minimum data acquisition time T_{min} with optimal parameters α^{opt} , N_{EX}^{opt} and T_R^{opt} . (b) The algorithm that finds the suboptimal data acquisition time T_{sub} with suboptimal parameters α^{sub} , N_{EX}^{sub} and T_R^{sub} . Both parameter sets (optimal and suboptimal) will provide the same SNR level, determined by the chosen K value. However, the data acquisition time provided by the optimal parameter set will be lower than the suboptimal parameter set with an amount depending on the chosen margin.



(a)

Figure 3.5: Relative $s_{\tilde{n}_w}$ of the \tilde{B}_z^{comb} for $N_E = 6, 9, 12$ and a range of T_C , where $\Delta T = 5.3$ ms, $T_2^* = 50$ ms and $f(\rho_0, \alpha, T_R) = 1$ in (2.22). $s_{\tilde{n}_w}$ is minimized when $T_C = 65, 75$ and 86 ms for $N_E = 6, 9$ and 12 , respectively.

3.1.2 Experimental Results of the ICNE-ME-FLASH Pulse Sequence

The results obtained using analytical modelling are validated experimentally using the implemented ICNE-ME-FLASH pulse sequence and the imaging phantom in Figure 2.1.

3.1.2.1 The Current-Induced \tilde{B}_z Imaging

Three points with almost the same acquisition times (2200 ms/ N_{PE}) are specified in Figure 3.2(a) ($K = 1$) with T_R (ms)/ N_{EX}/α : (I) $555/4/53$ (II) $155/14/30$ and (III) $86/25/23$. Using these parameters, the \tilde{B}_z^j distributions are acquired from the MRI complex signal using (2.2). The $s_{\tilde{n}_j}$ of the measured \tilde{B}_z^j distributions of the multiple (nine) echoes are shown in Figure 3.6(a). It is seen that the estimated $s_{\tilde{n}_j}$ of the multiple echoes for these three points are close to each other in accordance with the analytical estimation using (2.17).

The minimum $s_{\tilde{n}_j}$ (≈ 1.04 nT) is at $T_C = 50$ ms, which is equal to T_2^* value of the

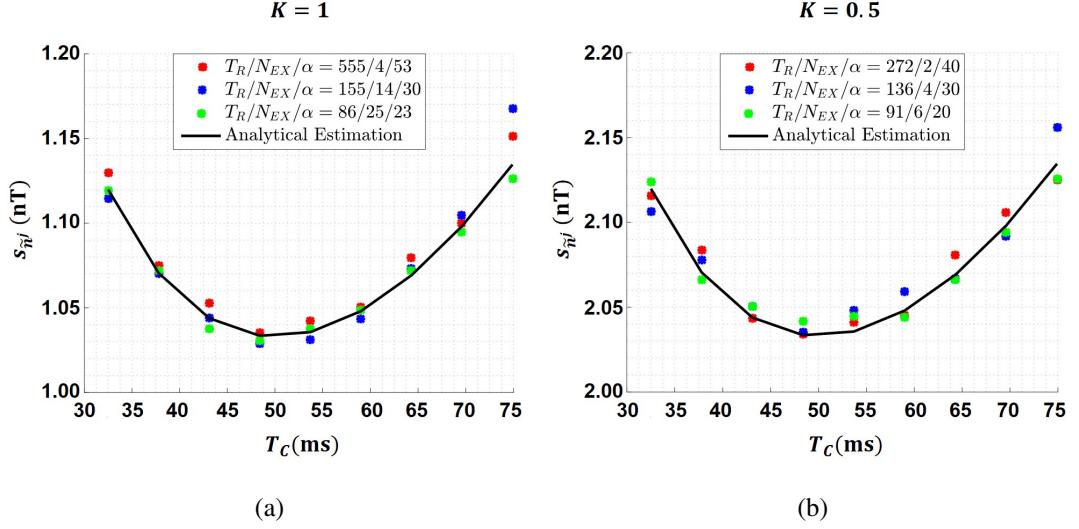


Figure 3.6: The $s_{\tilde{n}^j}$ of the ICNE-ME-FLASH pulse sequence for the parameter sets (a) (I) – (III) ($K = 1$), and (b) (IV) – (VI) ($K = 0.5$) of Figure 3.2.

saline solution. The \tilde{B}_z^{comb} distribution is calculated using the optimal weight set in (2.14). The estimated $s_{\tilde{n}_w}$ for the three points of $K = 1$ is given in Table 3.2 and \tilde{B}_z^{comb} distribution for parameter set (I) is shown in Figure 3.7(a). Similarly, for the three points of Figure 3.2(b) ($K = 0.5$) with T_R (ms)/ N_{EX}/α : (IV) 272/2/40 (V) 136/4/30 and (VI) 91/6/20 the estimated $s_{\tilde{n}^j}$ of the measured \tilde{B}_z^j distributions are shown in Figure 3.6(b). Similar to $K = 1$ the minimum estimated $s_{\tilde{n}^j}$ (≈ 2.03 nT) is at $T_C = T_2^* = 50$ ms. The estimated $s_{\tilde{n}_w}$ for the three points of $K = 0.5$ is given in Table 3.2 and \tilde{B}_z^{comb} distribution for parameter set (IV) is shown in Figure 3.7(b).

The estimated $s_{\tilde{n}^j}$'s for $K = 0.5$ are close to each other and almost twice the estimated $s_{\tilde{n}^j}$'s for the three points of $K = 1$. The amount of the estimated \hat{B}_z in (2.6) is dependent only on the geometry of the imaging phantom and the I , and this value is the same ($I = 2$ mA) for all measurement in our experiments. Hence, the SNR level estimated using the parameters in Figure 3.2(a) is almost twice the estimated SNR level using the parameters in Figure 3.2(b). The experimental results of different parameters sets specified in Figure 3.2 is summarized in Table 3.2.

Considering the results in Figures 3.6-3.7 and Table 3.2, the experimentally measured data confirm the results of the proposed methods in (2.10), (2.13) and (2.26).

Table 3.2: The estimated noise standard deviation of the measured \tilde{B}_z^4 ($s_{\tilde{n}^4}$) ($T_C^4 = T_2^* = 50$ ms), the estimated $s_{\tilde{n}_w}$ and the T_{Total} (for $N_{PE} = 64$) of the parameter sets in Figure 3.2.

K Value	T_R (ms)/ N_{EX}/α°	$s_{\tilde{n}^4}$ (nT)	$s_{\tilde{n}_w}$ (nT)	T_{Total} (sec)*
$K = 1$	555/4/53	1.04	0.42	284
	155/14/30	1.04	0.41	278
	86/25/23	1.03	0.42	276
$K = 0.5$	272/2/40	2.03	0.85	70
	136/4/30	2.04	0.81	70
	91/6/20	2.04	0.82	70
$K = 2$	590/15/55	0.50	0.21	1112

* For each parameter set, the \tilde{B}_z^j are acquired with the positive and negative current injection polarities in order to remove the systematic phase artifacts. Therefore, for each parameter set the acquisition time is $T_{Total}/2$.

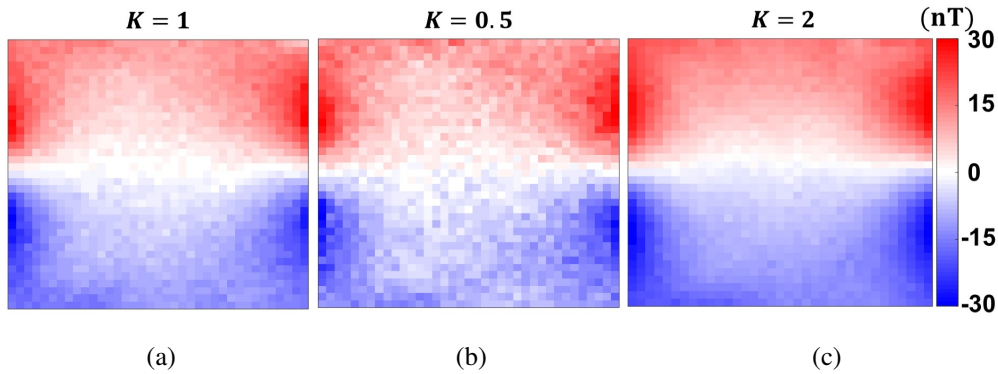


Figure 3.7: The calculated \tilde{B}_z^{comb} distributions of the imaging phantom using ICNE-ME-FLASH pulse sequence with parameter sets T_R (ms)/ N_{EX}/α : (a) 555/4/53 ($K = 1$) (b) 272/2/40 ($K = 0.5$) and (c) 590/15/55 ($K = 2$). The $s_{\tilde{n}_w} \approx 0.42, 0.85,$ and, 0.20 nT for (a), (b) and (c), respectively.

By injecting $I = 2$ mA current into the imaging phantom, the maximum measured \tilde{B}_z is in the order of 30 nT near the electrodes and the amplitude of the readout gradient for $BW = 200$ Hz/pixel is 2.4 mT/m. Therefore, the amount of the shift per pixel due to current injection during data acquisition (readout) can be calculated as [20]:

$$\Delta x = \frac{B_z(x, y)}{G_x} = \frac{30 \text{ nT}}{2.4 \text{ mT/m}} = 12.5 \mu\text{m} \quad (3.1)$$

Since the pixel size of the measured \tilde{B}_z images is $2 \times 2 \text{ mm}^2$, this amount of shift is negligible.

3.1.3 The Effect of Intensive Utilization of Gradients on the Measured \tilde{B}_z

The ΔB_0 variation due to intensive utilization of the gradient pulses is calculated using (2.32). To investigate the effect of ΔB_0 on the MRCDI experiments using the ICNE-ME-FLASH pulse sequence, the noise distribution and the $s_{\tilde{n}_j}$ of the measured \tilde{B}_z^j from N acquisitions are estimated using (2.33)-(2.36). The saline-filled phantom shown in Figure 2.1 is used to acquire $N = 50$ acquisitions using the same sequence parameters: $T_R(\text{ms})/N_{EX}/\alpha : 136/4/30$. These are the parameters of point (V) in Figure 3.2(b) for $K = 0.5$. A single current injection (horizontal) profile is used.

The estimated noise distribution and the standard deviation of the ninth (last) echo ($D_i^9(x, y)$ and $s_{\tilde{n}_i^9}$) for $N = 50$ acquisitions are shown in Figure 3.8(a) and (b), respectively. The mean of the estimated noise distributions and the calculated ΔB_0 using (2.32) for $N = 50$ acquisitions of entire echoes are shown in Figure 3.9(a) and (b), respectively. The noise distributions are Gaussian, but their means are non-zero, as shown in Figure 3.8(a). The noise means move from the zero value of the first acquisition to the positive values of the last. This behavior is observed in the estimated mean of all echoes 3.9(a). The estimated $s_{\tilde{n}_i^9}$ of $N = 50$ acquisitions is shown in Figure 3.8(b). The mean value of the estimated noise standard deviations for $N = 50$ acquisitions $\hat{s}_{\tilde{n}_i^9}$ is about 2.09 nT, which is consistent with the estimated $s_{\tilde{n}_i^9}$ in Figure 3.6(b) for $K = 0.5$.

The estimated noise means of the measured \tilde{B}_z^j distributions and the calculated ΔB_0 for entire echoes during $N = 50$ acquisitions are similar, as shown in Figure 3.9(a) and (b). The amount of ΔB_0 shift and the noise mean slip during $N = 50$ acquisitions

of all echoes is about 10 nT.

In another experiment, the $N = 50$ acquisitions are performed by increasing the N_{EX} value to 32 and the same T_R and α values. Using this N_{EX} , the calculated ΔB_0 and the estimated noise mean slip is about 70 nT, which shows a 7 times increase in comparison with the data acquired with $N_{EX} = 4$.

The ΔB_0 shift (or the noise mean) can be removed from the \tilde{B}_z images by subtracting the noise mean of each measured \tilde{B}_z^j from the corresponding \tilde{B}_z^j image. After ΔB_0 shift cancellation, $\hat{\mu}^j(x, y)$, $D_i^j(x, y)$ and $s_{\tilde{n}^j}$ must be re-estimated using (2.33)-(2.36). The noise distribution of $N = 50$ measurements of the ninth (last) echo after correction is shown in Figure 3.10.

The results in Figures 3.8-3.10 show that the intensive utilization of the gradients in MRCDI experiments using ICNE-ME-FLASH pulse sequence results in a shift in the mean of the additive Gaussian noise on the measured \tilde{B}_z^j distributions.

3.1.4 The Effect of MHD Flow on the Acquired \tilde{B}_z images in MRCDI

In the implemented ICNE-FLASH and ICNE-ME-FLASH pulse sequences, there are no flow encoding gradients. Therefore, MHD flow does not contribute directly to the acquired MR signal. However, the effect of motion of fluid particles with the velocity of \bar{v} due to MHD flow must be considered in the MRCDI of the liquids with low viscosity.

The numerical simulation procedure to acquire the \bar{v} distributions is explained in [83]. $I = 2$ mA current pulses are injected in the horizontal direction for $T_c = 75$ ms. The conductivity of the liquid material is $\sigma = 0.35$ S m⁻¹ similar to the experimental phantom. The \bar{v} distributions are acquired for three different T_R (ms): 86, 155 and 555 in accordance with the experimental parameters for $K = 1$. The simulated \bar{v} distributions are given in Figure 3.11.

The amplitude and duration of the injected current are the same for all simulations ($I = 2$ mA and $T_C = 75$ ms). However, by assigning different T_R values, the calculated \bar{v} distributions show differences. Using a shorter T_R reduces the falling of \bar{v}

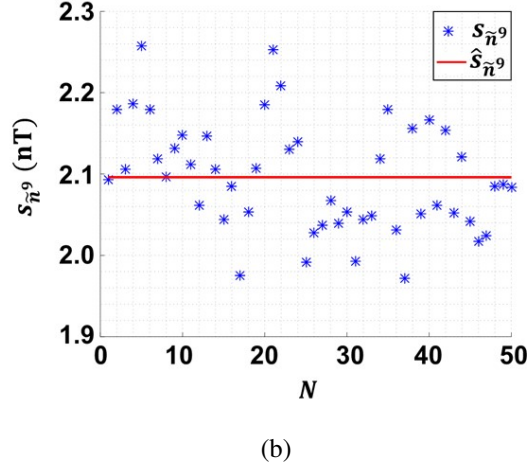
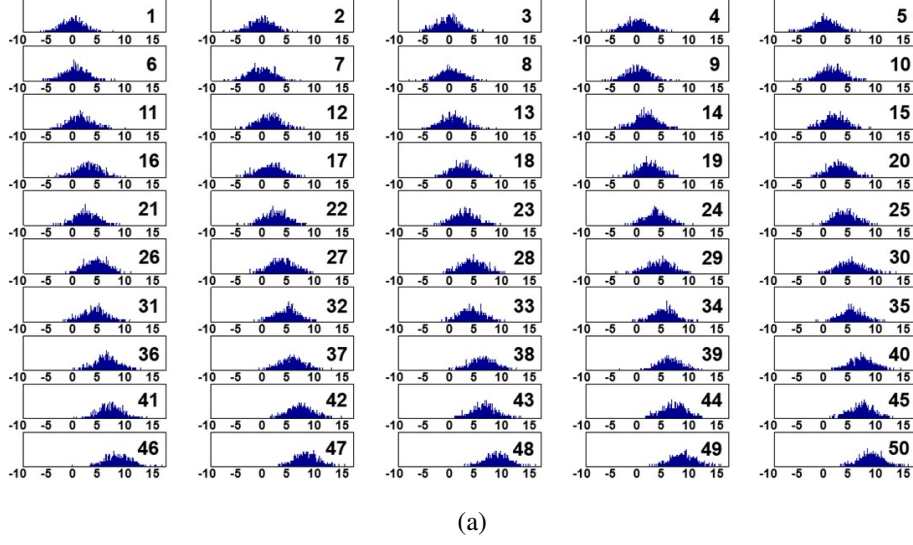


Figure 3.8: (a) The estimated noise distribution of $N = 50$ acquisitions of the ninth (last) echo, $D_i^9(x, y)$. The unit of the noise (x-axis) is nT. (b) The estimated $s_{\tilde{n}^9}$ of $N = 50$ acquisitions (blue stars) and their mean value ($\hat{s}_{\tilde{n}^9}$) (red line)

from T_R to T_R and results in a faster reach to the steady-state with a higher amplitude.

The amount of MHD-based distortion due to \bar{v} distribution in the acquired \tilde{B}_z distribution, ε_{MHDB_z} , can be calculated as:

$$\varepsilon_{MHDB_z} = \int_0^{T_C} \nabla B_z(x, y) \cdot \bar{v}(x, y, t) dt \quad (3.2)$$

Assuming a steady-state constant velocity (\bar{v}_{ss}) distribution (3.2) can be written as:

$$\varepsilon_{MHDB_z} = (\nabla B_z \cdot \bar{v}_{ss}) T_C \quad (3.3)$$

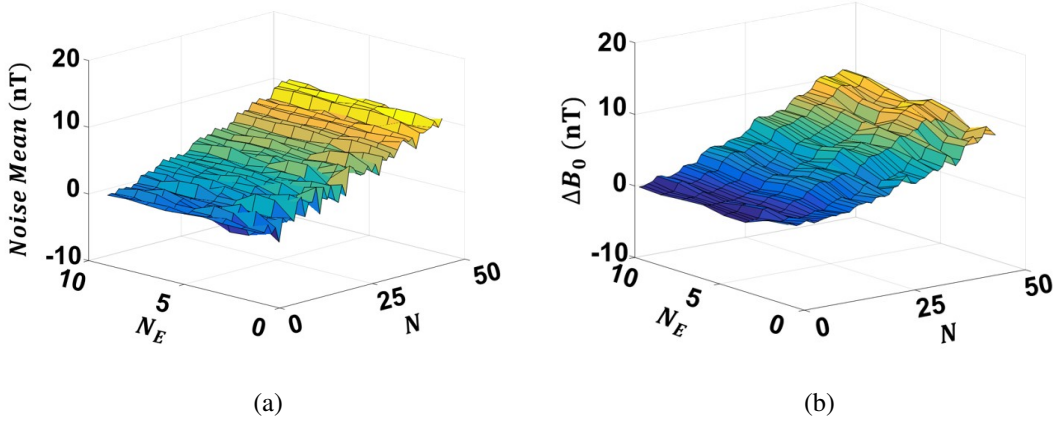


Figure 3.9: (a) The estimated noise means of the acquired \tilde{B}_z^j and (b) the calculated ΔB_0 for $N = 50$ acquisitions of the entire nine echoes.

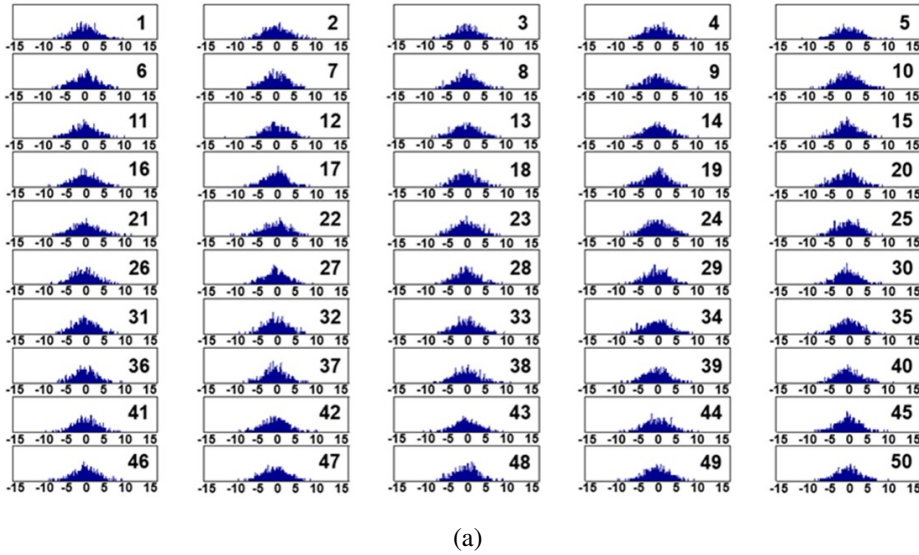


Figure 3.10: (a) The estimated $D_i^g(x, y)$ distributions for $N = 50$ acquisitions after ΔB_0 cancellation.

The B_z distribution of the FE model for $I = 2$ mA injected current in the horizontal direction is shown in Figure 3.12(a). The calculated ε_{MHDB_z} distributions for three different \bar{v} distributions in Figure 3.11 are shown in Figure 3.12(b)-(c). As seen from 3.12(b)-(c) the amplitude of the \bar{v} distribution and the MHD based B_z distortions reduce by increasing T_R . The maximum calculated ε_{MHDB_z} ($\varepsilon_{MHDB_z}^{max}$) is near the

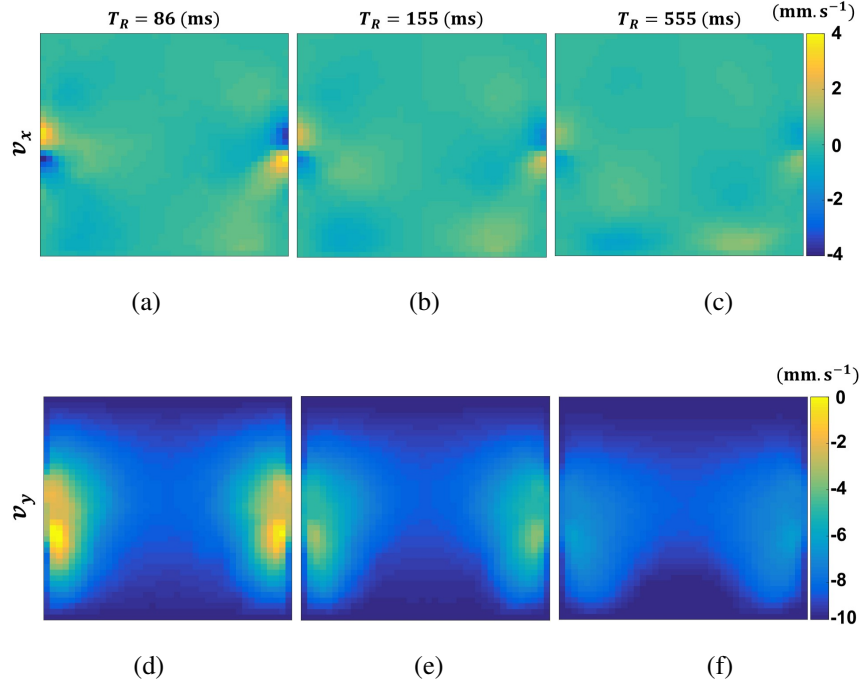


Figure 3.11: The simulated \bar{v} distributions in the x- and y- directions v_x and v_y for $T_R(\text{ms}) = 86, 155$ and 555 . (a)-(c) v_x and (d)-(f) v_y distributions, respectively.

current injection electrodes $\varepsilon_{MHD B_z}^{max} = 1.6$ nT, which is about four times the estimated $s_{\tilde{n}_w}$ for $K = 1$. The results related to the proposed ICNE-ME-FLASH pulse sequence, SNR and the total data acquisition time analysis and the effects of MHD flow and the intensive utilization of gradients on the measured \tilde{B}_z in MRCDI experiments are discussed in Chapter 4: Section 4.1.

3.2 The Results of the Proposed Dual and Single Current DT-MREIT

In this section, the proposed dual and a single current DT-MREIT methods in Section 2.4 is evaluated using the simulated data and the experimental measurements of the biological tissue phantoms. The methods proposed in Section 2.4 and the results reported in this section are published in [31] and presented in [134, 135].

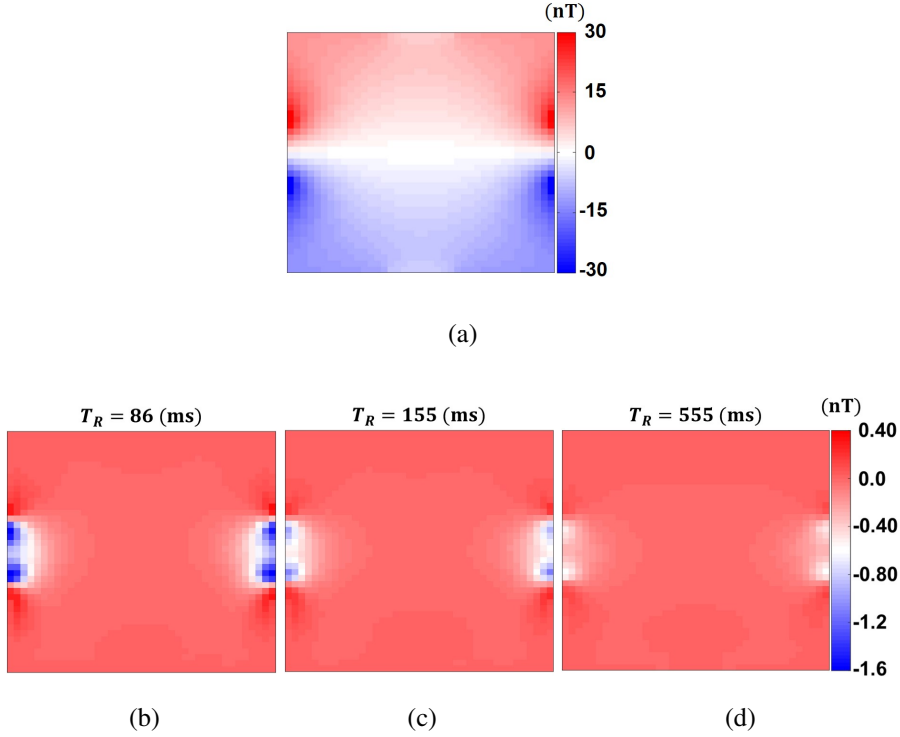


Figure 3.12: (a) The B_z distribution of the FE model for $I = 2$ mA current injection. The calculated ε_{MHDB_z} distributions due MHD flow velocity \bar{v} for T_R (ms) (b) 86, (c) 155, and (d) 555.

3.2.1 Results of Simulation Model

3.2.1.1 Noise-Free Simulation

Electrical current with the amplitude of 3 mA is injected in the horizontal (x) and vertical (y) directions to the FE model in Figure 3.10. B_z and \bar{J}_p distributions for both current injection patterns are shown in Figure 3.13. ECDR distributions are reconstructed for single (vertical and horizontal) and dual current injection patterns using (2.66) and (2.68), respectively. ECDR distribution is also reconstructed using the method proposed in [69], which is implemented in [136] in order to compare the results. The reconstructed ECDR distributions using dual and a single current methods for the noiseless case are shown in Figure 3.14 (a), (e), (i), (m). Moreover, the mean values of the reconstructed ECDR distributions in different regions of the simulation model are presented in Table 3.3.

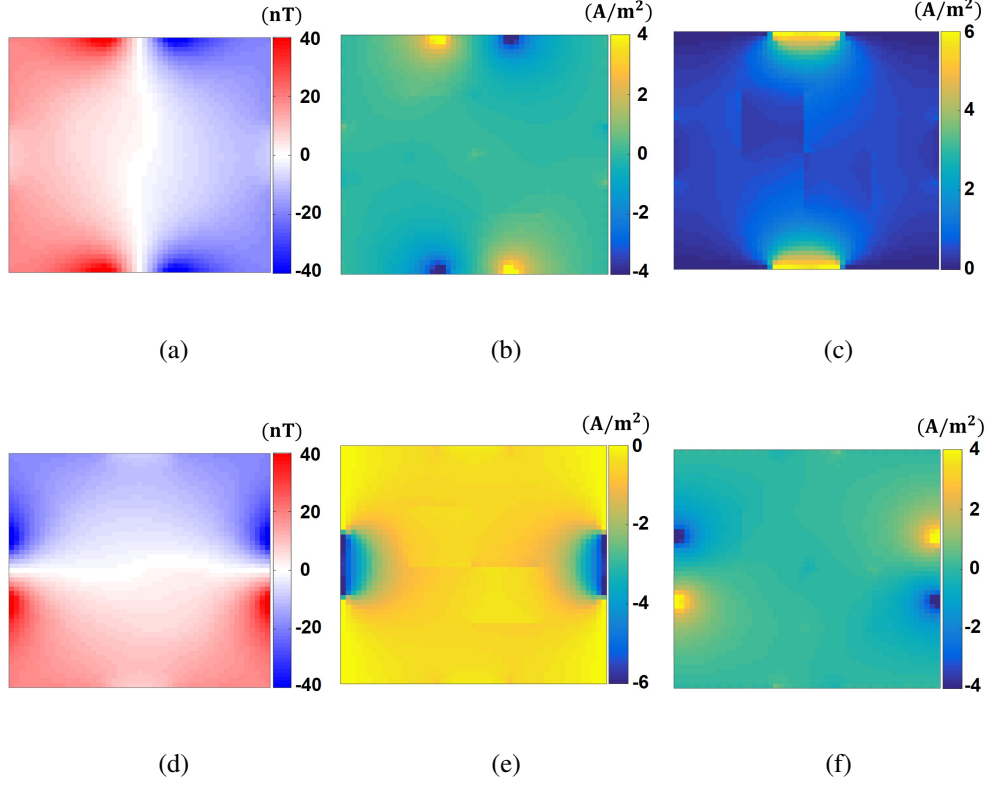


Figure 3.13: The simulated B_z distribution of the vertical current injection, B_{z_V} , and the corresponding (b) J_{px_V} and (c) J_{py_V} . (d) The simulated B_z distribution of the horizontal current injection, B_{z_H} , and the corresponding (e) J_{px_H} and (f) J_{py_H} distributions.

3.2.1.2 Noise Analysis

Noise analysis is performed by adding white Gaussian noise to simulated diffusion and B_z data to evaluate the noise performance of the proposed methods at different SNR levels. The SNR is defined as:

$$\text{SNR (dB)} = 20 \log \left(\frac{\text{RMS}(S)}{s_{\tilde{n}}} \right) \quad (3.4)$$

where $\text{RMS}(S)$ is the root mean square of the noiseless distribution, and $s_{\tilde{n}}$ is the standard deviation of the added noise. The reconstructed ECDR distributions using the method proposed in [69] for two current injections, and the methods with single and dual current injections proposed in (2.66) and (2.68) for different SNR levels are shown in Figure 3.14.

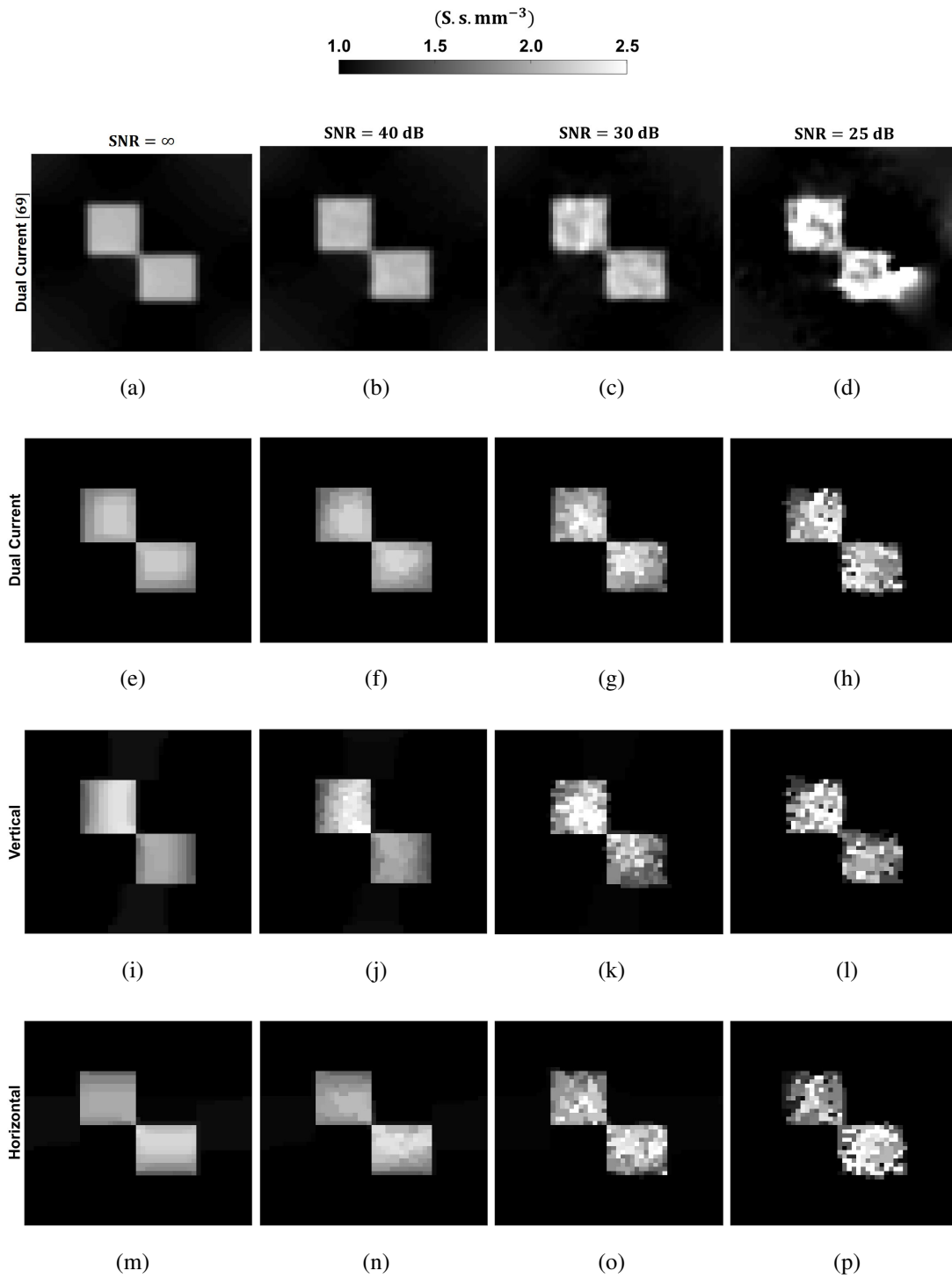


Figure 3.14: (a-d) The reconstructed ECDR for different SNR levels using the method proposed in [73] for dual current injection patterns. The reconstructed ECDR using the proposed methods with (e-h) dual current and a single current injection (i-l) vertical and (m-p) horizontal for different SNR levels.

Table 3.3: The mean values of the reconstructed ECDR distributions in different regions of the simulations model using dual and a single current methods for noiseless case. The true values of the ECDR distribution is 1 S s mm^{-3} and 2 S s mm^{-3} for the background and the inhomogeneities, respectively.

Method	Region	ECDR (S s mm^{-3})
Dual Current in [69]	Left	2.00 ± 0.06
	Right	1.99 ± 0.07
	Background	1.01 ± 0.05
Dual Current	Left	2.00 ± 0.14
	Right	2.00 ± 0.14
	Background	1.00 ± 0.01
Single Current (Vertical)	Left	2.06 ± 0.18
	Right	1.91 ± 0.10
	Background	1.01 ± 0.05
Single Current (Horizontal)	Left	1.90 ± 0.10
	Right	2.07 ± 0.16
	Background	1.01 ± 0.04

The anisotropic conductivity distributions of the simulation model are reconstructed using the ECDR distributions in Figure 3.14(e-p) and the noisy diffusion data. The Root Mean Square Error (RMSE) values of the reconstructed conductivity tensors in different regions are calculated, as given in Figure 3.15.

Note that during the acquisition of the plots in Figure 3.15, the regularization parameter for each case (vertical, horizontal, and dual currents) are kept constant for different SNR levels. The RMSE is defined as:

$$\text{RMSE (\%)} = \sqrt{\frac{1}{N} \sum_{j=1}^N \frac{(c_{\text{True}}^j - c_{\text{Rec}}^j)^2}{(c_{\text{Rec}}^j)^2}} \times 100 \quad (3.5)$$

where N is the number of pixels in the region of interest, c_{True}^j and c_{Rec}^j are the true and reconstructed values of the distribution of interest in the j^{th} pixel.

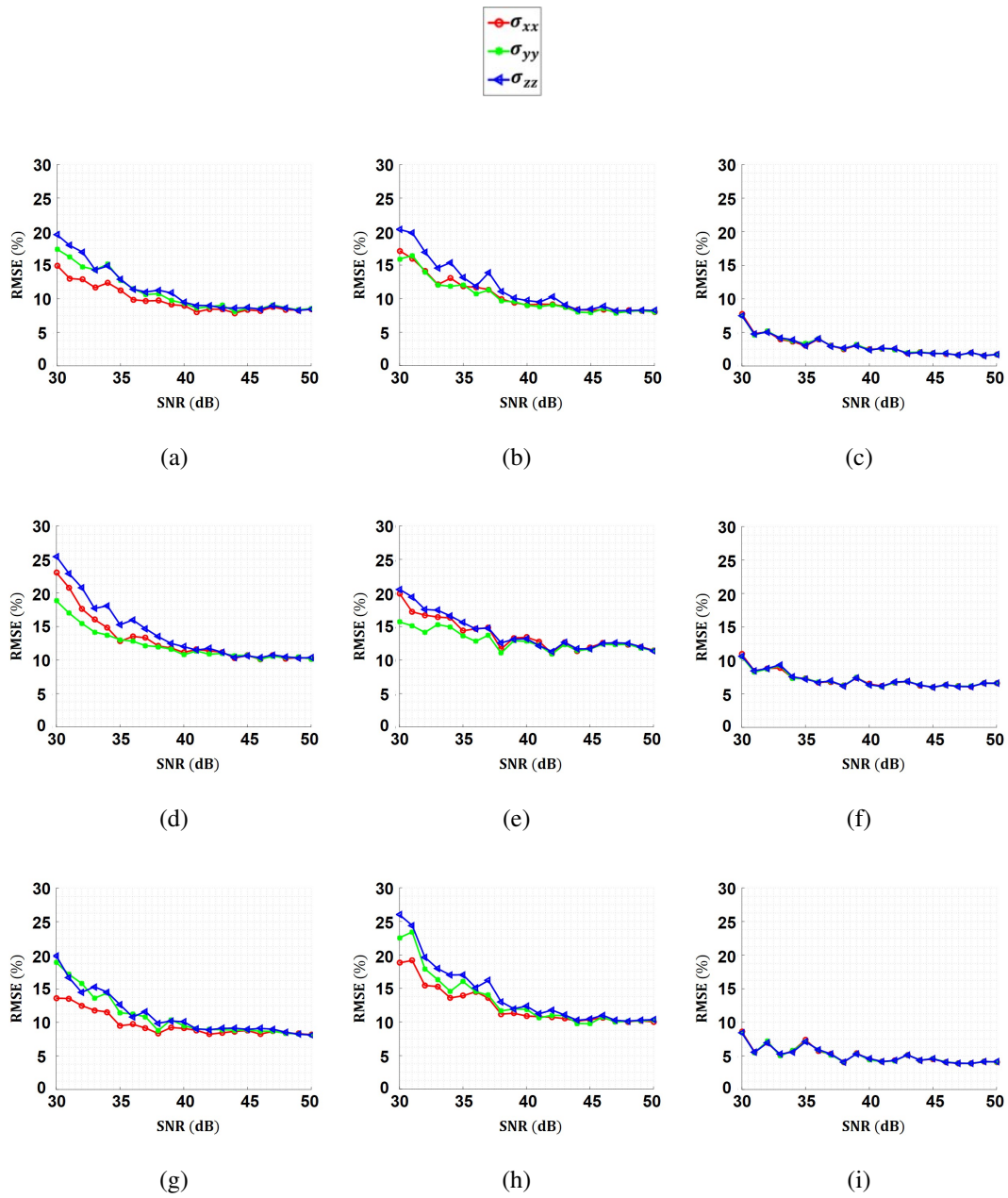


Figure 3.15: The RMSE values of the reconstructed \overline{C} for different SNR levels in different regions of the simulation model using the proposed method with dual current injections: (a) left inhomogeneity, (b) right inhomogeneity, and (c) background, with vertical current injection: (d) left inhomogeneity, (e) right inhomogeneity and (f) background and horizontal current injection: (g) left inhomogeneity, (h) right inhomogeneity and (i) background.

3.2.2 Practical Realization of DT-MREIT by Using Experimental Measurements

The proposed methods for dual and single current injections are evaluated using the two biological tissue phantoms with anisotropic conductivity and diffusion distributions shown in Figures 2.5 and 2.6.

Experiments performed at a 3 T clinical MRI scanner (MAGNETOM Trio, Siemens AG, Erlangen, Germany) with 60 cm bore diameter, 45 mT/m maximum gradient strength, and a 32 channel head coil. Multi-channel data combined using the adaptive combination. The electrical current is injected into the experimental phantom in synchrony with ICNE-ME-FLASH pulse sequence employing shielded cables and copper electrodes in the vertical and horizontal directions using a custom-designed MR conditional current source [102]. To avoid cable-induced magnetic stray field the cables were aligned with the direction of the main magnetic field.

The ICNE-ME-FLASH pulse sequence parameters are selected considering the proposed analysis in Section 2.1 to maximize the SNR of the acquired \tilde{B}_z^{comb} and the estimated \bar{J}_p in a clinically acceptable time and avoiding high N_{EX} values.

3.2.2.1 DTI of the Experimental Phantoms

DW images of both biological tissue phantoms Ph 1 and Ph 2 is acquired using the SS-SE-EPI pulse sequence shown in Figure 2.2 with the parameters given in Table 2.3. The six unique parameters of the diffusion tensor for each voxel are reconstructed using the corrected DW images and DTI-FIT command of FSL [117]. For Ph 1, the DW images are acquired with $N_{EX} = 2$. The k-space data of the DTI contain inconsistent phase errors as explained in Section 2.3. Therefore, performing averaging in the k-space cause a signal loss that varies across the image. To avoid this, the magnitude image associate with each k-space data was calculated individually and the required corrections performed on each magnitude image. Then the averaging performed using the corrected magnitude images. The colored FA map and MD of the reconstructed diffusion tensors of both phantoms are shown in Figures 2.5 and 2.6.

3.2.2.2 CDI of the Experimental Phantoms

Electrical current with the amplitude of 3 mA is injected into the experimental phantoms Ph 1 and Ph 2 in the vertical and horizontal directions. The current pulses are injected in synchrony with the ICNE-ME-FLASH pulse sequence shown in Figure 1.1 with the parameters given in Table 2.4. Considering $T_R = 560$ and 540 ms the stimulation frequency in both experiments is approximately 2 Hz. To prevent cable induced magnetic stray fields [49], the current injection cables are aligned with the direction of the B_0 . The multiple \tilde{B}_z^j distributions measured from the multiple echoes (9 echoes) are combined using (2.14) and (2.15) to obtain \tilde{B}_z^{comb} , as shown in Figures 3.16 and 3.17 for the vertical and horizontal current injection patterns.

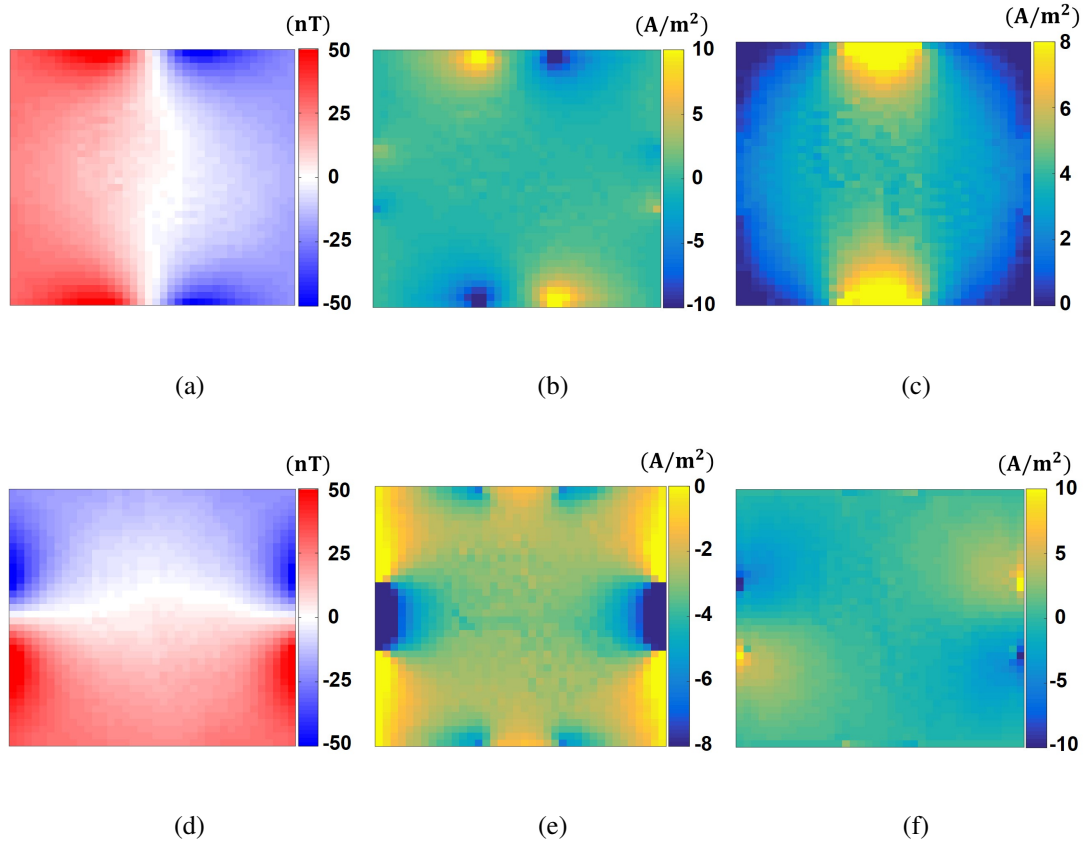


Figure 3.16: \tilde{B}_z^{comb} and \bar{J}_p distributions of the experimental Ph 1. (a) \tilde{B}_z^{comb} for vertical current injection, \tilde{B}_{zV}^{comb} , and the corresponding estimated (b) J_{pxV} and (c) J_{pyV} . (d) \tilde{B}_z^{comb} and the corresponding estimated (e) J_{pxH} and (f) J_{pyH} distributions.

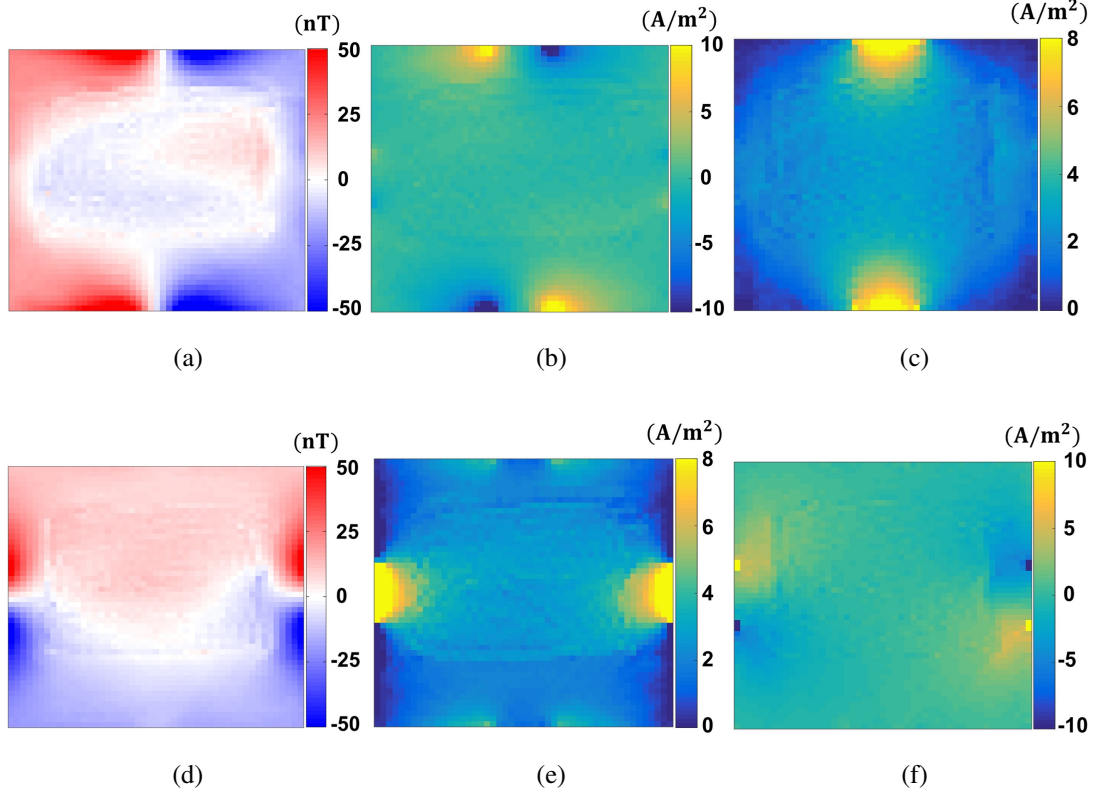


Figure 3.17: \tilde{B}_z^{comb} and \bar{J}_p distributions of the experimental Ph 2. (a) \tilde{B}_{zV}^{comb} and the corresponding (b) J_{pxV} and (c) J_{pyV} . (d) \tilde{B}_{zH}^{comb} and the corresponding (e) J_{pxH} and (f) J_{pyH} distributions.

The \bar{J}_p distributions are estimated using (2.47) for the vertical and horizontal current injection patterns of Ph 1 and Ph 2, as shown in Figures 3.16 and 3.17.

The optimum T_C value provide the highest SNR in the \tilde{B}_z^{comb} distribution of the biological tissues in Ph 1 and Ph 2 is calculated by solving the polynomial in (2.26). Solving the polynomial in (2.26) with $N_E = 9$, $\Delta T = 5.3$ ms and $T_2^* = 20$ and 37 ms for the muscle pieces in Ph 1 and Ph 2, respectively, gives the optimum values of $T_C = 50$ and 63 ms. The other T_C^j values can be calculated using (2.27), as given in Table 2.4.

Considering the T_1 values of the biological tissues in Ph 1 and Ph 2 and assigning a desired N_{EX} and K the ICNE-ME-FLASH pulse sequence parameters are calculated as given in Table 2.4.

Note that, in choosing an appropriate K value, the desired SNR and the total acquisition time are considered simultaneously. Since Ph 2 has larger dimensions than Ph 1, a larger FOV is required, as given in Table 2.4. To keep the pixel size the same for both phantoms, more phase encoding steps are required for Ph 2, which increases T_{Total} . Therefore, to keep T_{Total} clinically acceptable, a lower K ($= 1.5$) is preferred for data acquisition of Ph 2.

3.2.2.3 Conductivity Tensor Reconstruction of the Ph 1

The reconstructed ECDR distributions of the experimental phantom Ph 1 using the proposed dual and single current injection methods in (2.66) and (2.68) are shown in Figure 3.18.

The $\overline{\overline{C}}$ distributions are obtained from the reconstructed ECDR distributions and the diffusion tensor data using (1.23). The diagonal components of the reconstructed $\overline{\overline{C}}$ using the proposed dual and single current injection methods is shown in Figure 3.19. Also, the mean values of the reconstructed $\overline{\overline{C}}$ in different regions of Ph 1 and the calculated anisotropy ratio (AR) for the two muscle pieces are given in Table 3.4. To better visualize the reconstructed $\overline{\overline{C}}$ distribution in different regions of Ph 1, the ellipsoid plot of the reconstructed $\overline{\overline{C}}$ for the horizontal current injection pattern is shown in Figure 3.20. The colors of the ellipsoids show that main direction of conductivity for each pixel. Red and green colors show that the conductivity is higher in the x- and y-directions, respectively. White color in the background shows isotropic conductivity distribution of the saline solution. These observations are consistent with the calculated colored FA map of the Ph 1 in Figure 2.5(b). The amount of anisotropy at each voxel (pixel) can be understood from the shape of the ellipsoid. A prolated ellipsoid shows a higher anisotropy. In contrast, in the regions with isotropic distribution, the ellipsoid turns into a sphere (with white color) like the voxels of the background of the Ph 1, which is filled with saline solution.

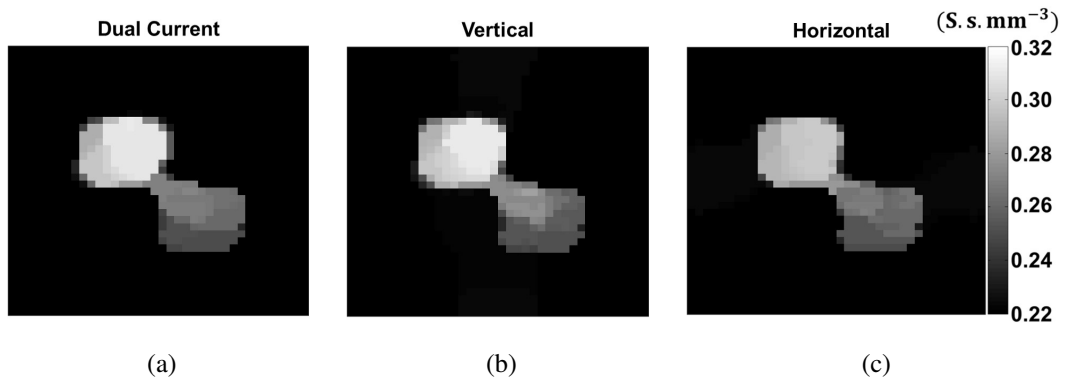


Figure 3.18: The reconstructed ECDR distributions of Ph1 using the proposed method with (a) dual, (b) vertical, and (c) horizontal current injection patterns.

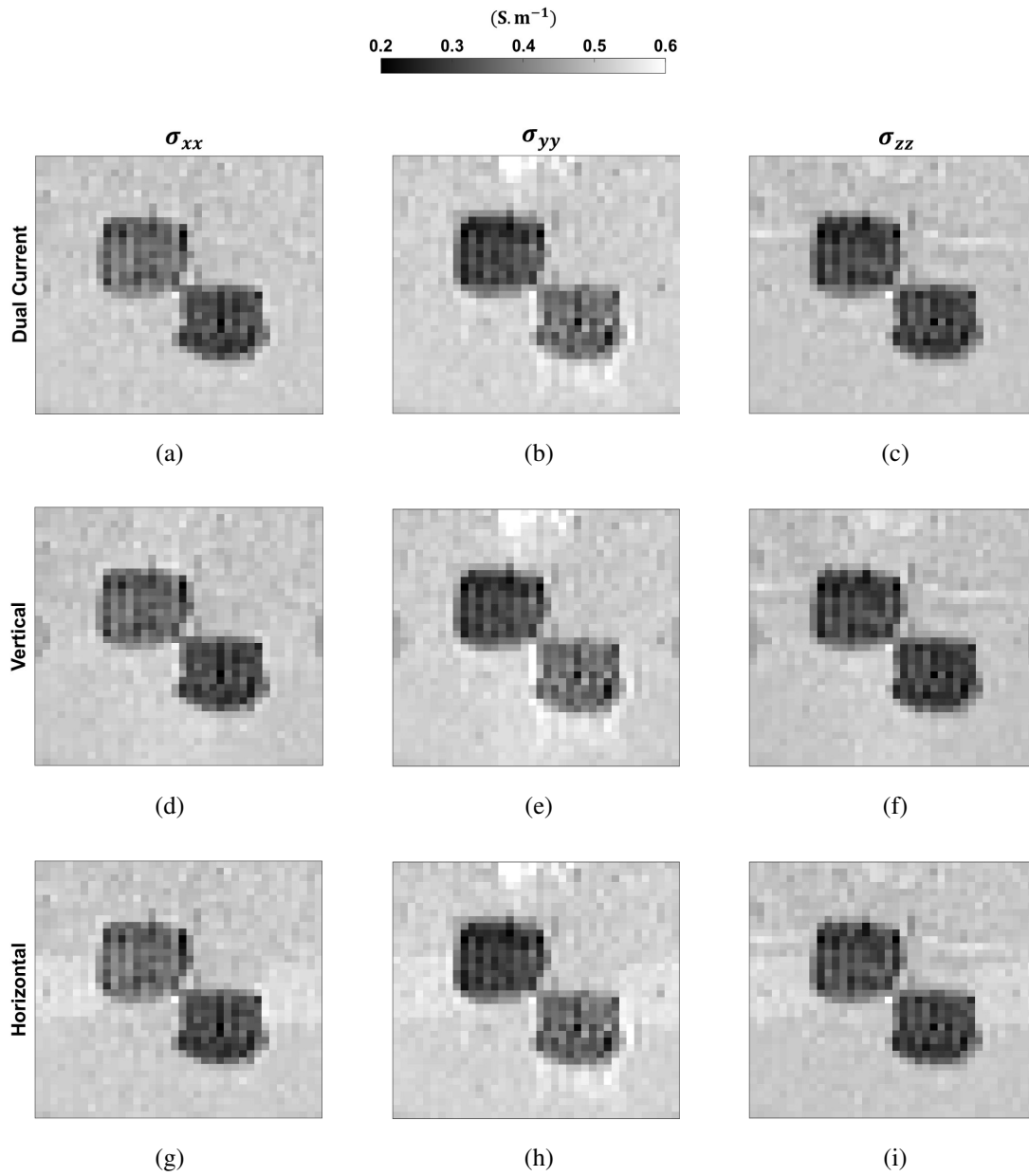


Figure 3.19: The diagonal components of the reconstructed $\overline{\overline{C}}$ (σ_{xx} , σ_{yy} and σ_{zz}) of the experimental phantom Ph 1 using the proposed method with (a-c) dual, (d-f) vertical and (g-i) horizontal current injections. The effect of overestimation of ECDR distribution is barely visible in the reconstructed σ_{xx} , σ_{yy} and σ_{zz} of the horizontal current injection.

Table 3.4: The mean values of the reconstructed σ_{xx} , σ_{yy} and σ_{zz} in different regions of Ph 1 for dual, vertical and horizontal current injections. The $\overline{\overline{C}}$ distributions are reconstructed using the proposed methods in (2.66) and (2.68) for a single and dual current injections. The AR for the left and right muscle pieces are calculated as $\frac{\sigma_{xx}}{\sigma_{yy}}$ and $\frac{\sigma_{yy}}{\sigma_{xx}}$, respectively.

Method	Region	σ_{xx} (S m ⁻¹)	σ_{yy} (S m ⁻¹)	σ_{zz} (S m ⁻¹)	AR ($\frac{\sigma_{xx}}{\sigma_{yy}}$, $\frac{\sigma_{yy}}{\sigma_{xx}}$)
Dual	Left	0.36 ± 0.01	0.33 ± 0.01	0.32 ± 0.01	1.15 ± 0.10
	Right	0.31 ± 0.01	0.38 ± 0.01	0.31 ± 0.02	1.22 ± 0.08
	Background	0.51 ± 0.02	0.52 ± 0.02	0.50 ± 0.02	-
Vertical	Left	0.35 ± 0.02	0.32 ± 0.01	0.30 ± 0.01	1.1 ± 0.10
	Right	0.32 ± 0.02	0.37 ± 0.02	0.29 ± 0.02	1.15 ± 0.10
	Background	0.54 ± 0.03	0.54 ± 0.03	0.53 ± 0.03	-
Horizontal	Left	0.37 ± 0.01	0.33 ± 0.02	0.32 ± 0.03	1.12 ± 0.09
	Right	0.31 ± 0.01	0.36 ± 0.02	0.30 ± 0.02	1.16 ± 0.08
	Background	0.55 ± 0.03	0.56 ± 0.02	0.54 ± 0.04	-

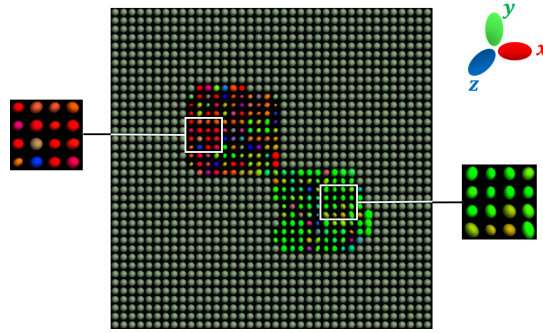


Figure 3.20: The ellipsoid plot of the reconstructed $\overline{\overline{C}}$ distribution of Ph 1. The conductivity of the left and right muscle pieces are higher in the x- and y- directions, respectively. Due to a low amount of AR in both muscle pieces the ellipsoids have more spheroidal shape than the elliptical, as shown in the magnified regions of the left and right muscle pieces. The background with isotropic isotropic distribution is presented using white ellipsoids. The main direction of conductivity at each voxel can be determined using the given color map.

3.2.2.4 Conductivity Tensor Reconstruction of the Ph 2

The reconstructed ECDR distributions of the experimental phantom Ph 2 using the proposed dual and single current injections is shown in Figure 3.21. In the reconstructed ECDR distributions for vertical and horizontal current injection patterns the effect of overestimation of ECDR is barely visible in the regions under the current injection electrodes. Similar to Ph 1 the $\overline{\overline{C}}$ distributions are obtained using the reconstructed ECDR distributions in Figure 3.21 and the diffusion tensor data using (1.23). The diagonal components of the reconstructed $\overline{\overline{C}}$ for the proposed dual and single current injection methods is shown in Figure 3.22. Also, the mean values of the reconstructed $\overline{\overline{C}}$ distributions in different regions of Ph 2 and the calculated AR of the muscle piece are given in Table 3.5. The ellipsoid plot of the reconstructed $\overline{\overline{C}}$ for Ph 2 is shown in Figure 3.23. The red color of the ellipsoids inside the muscle piece shows a higher conductivity in the x-direction. Also, the ellipsoids are more prolated in Figure 3.23 in comparison with the muscle pieces in Figure 3.20. This difference indicates a higher anisotropy in the bovine muscle in Ph 2 in comparison with chicken muscles in Ph 1. The difference between the reconstructed conductivities along and perpendicular to the muscle fibers is better perceived visually using the ellipsoid plot. The results of the reconstructed ECDR and $\overline{\overline{C}}$ distributions of the simulated and experimental data using the dual and a single current DT-MREIT are discussed in Chapter 4: Section 4.2.

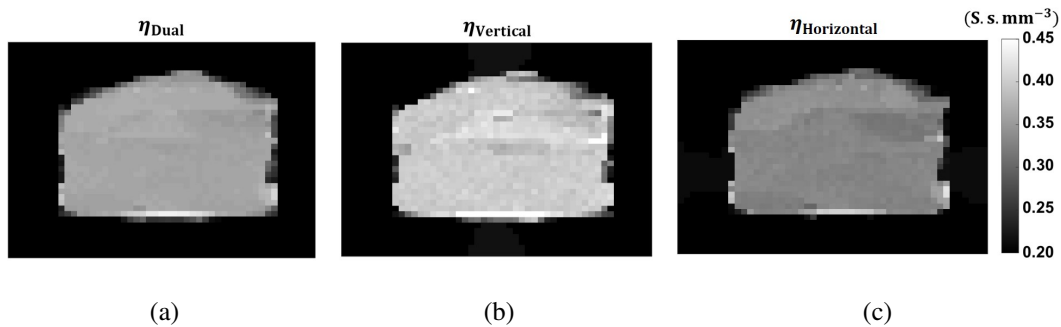


Figure 3.21: The reconstructed ECDR distribution of Ph 2 using the method with (a) dual (η_{Dual}) and single: (b) vertical (η_{Vertical}), and (c) horizontal ($\eta_{\text{Horizontal}}$) current injection patterns. The effect of ECDR overestimation is barely visible in the regions near to the current injection electrodes in the reconstructed η_{Vertical} and $\eta_{\text{Horizontal}}$.

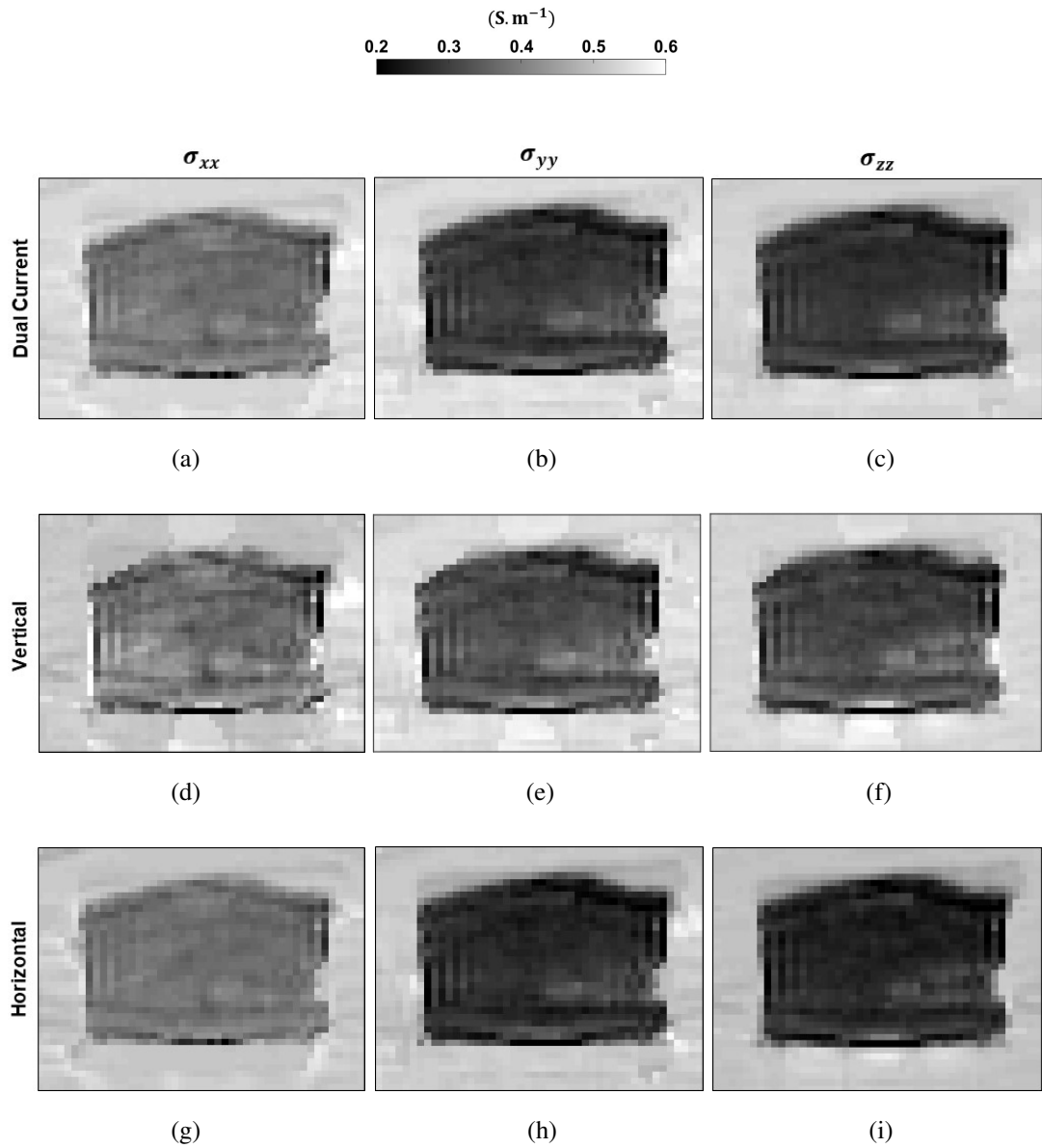


Figure 3.22: The diagonal components of the reconstructed $\overline{\overline{C}}$ (σ_{xx} , σ_{yy} and σ_{zz}) of the experimental phantom Ph 2 using the proposed DT-MREIT method with (a)-(c): Dual, (d)-(f): vertical, and (g)-(i): horizontal current injections.

Table 3.5: The mean values of the reconstructed \overline{C} (σ_{xx} , σ_{yy} and σ_{zz}) in different regions of Ph 2 for dual, vertical and horizontal current injections. The \overline{C} distributions are reconstructed using the proposed methods in (2.66) and (2.68) for a single and dual current injection DT-MREIT methods. The AR of the muscle piece is calculated as the ratio of conductivity in the direction parallel to the muscle fibers and the conductivity in the perpendicular direction ($\frac{\sigma_{xx}}{\sigma_{yy}}$).

Method	Region	σ_{xx} (S m ⁻¹)	σ_{yy} (S m ⁻¹)	σ_{zz} (S m ⁻¹)	AR ($\frac{\sigma_{xx}}{\sigma_{yy}}$)
Dual	Muscle	0.43 ± 0.03	0.24 ± 0.05	0.24 ± 0.05	1.79 ± 0.60
	Background	0.49 ± 0.02	0.52 ± 0.02	0.51 ± 0.02	-
Vertical	Muscle	0.45 ± 0.05	0.25 ± 0.06	0.25 ± 0.05	1.80 ± 0.55
	Background	0.54 ± 0.03	0.54 ± 0.02	0.53 ± 0.04	-
Horizontal	Muscle	0.41 ± 0.04	0.23 ± 0.06	0.23 ± 0.05	1.78 ± 0.50
	Background	0.55 ± 0.02	0.57 ± 0.03	0.55 ± 0.03	-

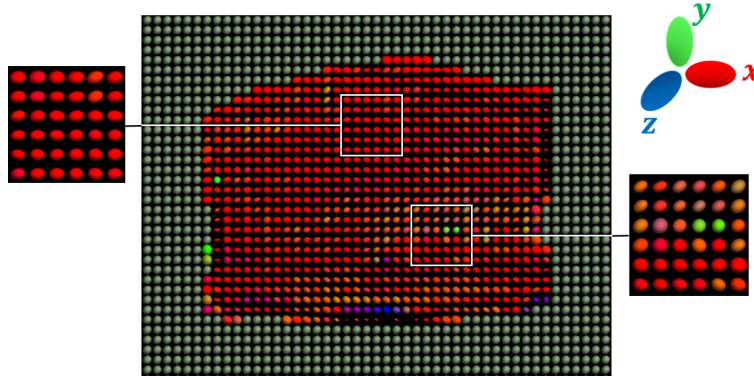


Figure 3.23: The ellipsoid plot of the reconstructed \overline{C} distribution of Ph 2. The conductivity of the muscle piece is higher in the x- direction than the other two perpendicular directions. A higher anisotropy in the bovine muscle piece cause more prolated ellipsoids. Two regions of the muscle with the high and relatively low AR are magnified in the left and right side of the figure, respectively. The background with isotropic distribution is presented using white spheres. The main direction of conductivity at each voxel can be determined using the given color map.

3.3 The Experimental Results of the Multi-Contrast Imaging Pulse Sequence

In this section, the experimental results of the multi-contrast imaging pulse sequence proposed in Section 2.6 is presented. The proposed pulse sequence and the associated reconstruction methods in Section 2.6 and the results reported in this section are presented in [137].

3.3.1 Multi-Contrast Data Acquisition of the Experimental Phantom

3.3.1.1 The Reconstructed Diffusion Tensor Distribution

The DW-SE pulse sequence with simultaneous current injection proposed in Section 2.6 (Figure 2.8) is used with parameters given in Table 2.5 to acquire the experimental data from the biological tissue phantom in Figure 2.9. The diagonal components of reconstructed $\overline{\overline{D}}$ for the horizontal and vertical current injections also the no current case are shown in Figure 3.24. The $\overline{\overline{D}}$ distribution for no current case is reconstructed from the DW images obtained in six flow encoding directions in (2.74) and a T_2 -weighted image. For diffusion tensor images with current injection in the vertical and horizontal directions, the magnitudes of six complex images acquired with I^+ and application of diffusion encoding gradient and one complex image acquired with I^+ but without diffusion encoding gradient application are used, as shown in Figure 3.24(d)-(i). On the other hand, the same data set exists for the current injection with negative polarity (I^-) for both vertical and horizontal current patterns. Hence, $\overline{\overline{D}}$ distribution of the experimental phantom can be solved twice for each current injection pattern, and these two tensor distributions can be averaged to increase the SNR level of the acquired $\overline{\overline{D}}$ by a factor of $\sqrt{2}$. The colored FA map of the experimental phantom is calculated from the reconstructed $\overline{\overline{D}}$ for no current case, as shown in Figure 3.25. The red and blue colors of the calculated colored FA map show that the main direction of diffusion (direction of muscle fibers) for the right and left muscle pieces is in the x- and z- directions, respectively. The mean values of the reconstructed $\overline{\overline{D}}$ in different regions of the experimental phantom is given in Table 3.6. It is seen that the reconstructed diffusion in the background with isotropic distribution is very close to the diffusion coefficient of water at room temperature ($D = 2.23 \times 10^{-3} \text{ mm}^2\text{s}^{-1}$),

which shows that the diffusion coefficient is solved correctly using the data acquired from the proposed multi-contrast imaging pulse sequence. On the other hand, the reconstructed $\overline{\overline{D}}$ in Figure 3.24 and Table 3.6 show a weak anisotropy for both muscle pieces. The mean calculated AR for the left and right muscle pieces is in the order of $\frac{\sigma_{xx}}{\sigma_{yy}} = 1.14$ and $\frac{\sigma_{zz}}{\sigma_{xx}} = 1.13$, respectively.

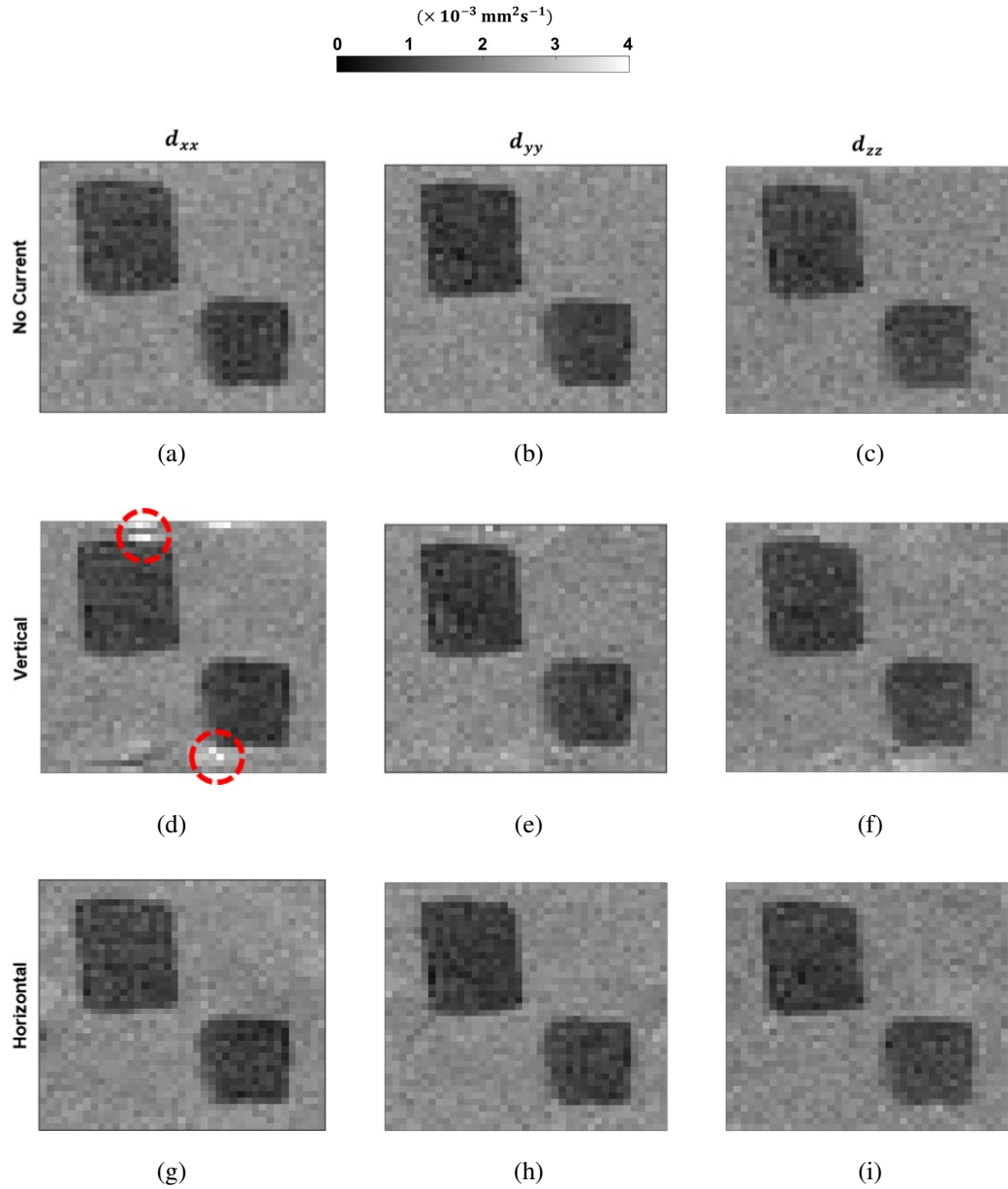


Figure 3.24: The reconstructed $\overline{\overline{D}}$ of the experimental phantom without current injection: (a) d_{xx} , (b) d_{yy} , (c) d_{zz} ; with vertical current injection (I_V^+): (d) d_{xx} , (e) d_{yy} , (f) d_{zz} ; with horizontal current injection (I_H^+): (g) d_{xx} , (h) d_{yy} , (i) d_{zz} . Minor artifacts nearside the muscle pieces in the diffusion tensor distributions obtained with I_V^+ are indicated with red circles.

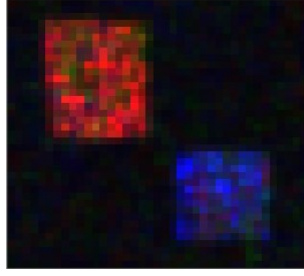


Figure 3.25: The coloured FA map of the experimental phantom calculated from the reconstructed $\overline{\overline{D}}$ for no current case. The red and blue colours in the left and right muscle pieces show that the diffusion is higher in the x- and z-directions, respectively.

3.3.1.2 The Measured MHD Flow Velocity Distribution

The MHD flow velocity distributions (\overline{v}) are calculated from the extracted $\phi_{MHD_{gd}}$ using (2.76) for the vertical and horizontal current injection patterns, as shown in Figure 3.26. The 2D arrow plot of the \overline{v} distributions (\overline{v}_V and \overline{v}_H) are shown in Figure 3.27. The MHD flow for vertical current injection is dominant in the horizontal (x-) direction, as shown in Figure 3.27(a). Conversely, for the horizontal current injection pattern, MHD flow is dominant in the vertical (y-) direction, as shown in Figure 3.27(b). Also, for both current injection patterns, the \overline{v} is higher under the current injection electrodes due to higher current density in those regions. Figure 3.26 shows that there is a four-times difference of the maximum \overline{v} values for the vertical and horizontal current injection patterns.

3.3.1.3 Current-Induced \tilde{B}_z and the Estimated Current Density Distributions

The \tilde{B}_z distributions of the injected current in the vertical and horizontal directions are reconstructed using (2.77) and shown in Figure 3.28(a) and (d), respectively. By injecting $I = 10$ mA current into the imaging phantom, the maximum measured \tilde{B}_z is in the order of 150 nT near the electrodes. The corresponding \overline{J}_p distributions for the vertical and horizontal current injection patterns are estimated as explained in Section 2.2 and shown in Figure 3.28. Also, the 2D vector plot of the estimated \overline{J}_{pV} and \overline{J}_{pH} are shown in Figure 3.29(a) and (b), respectively.

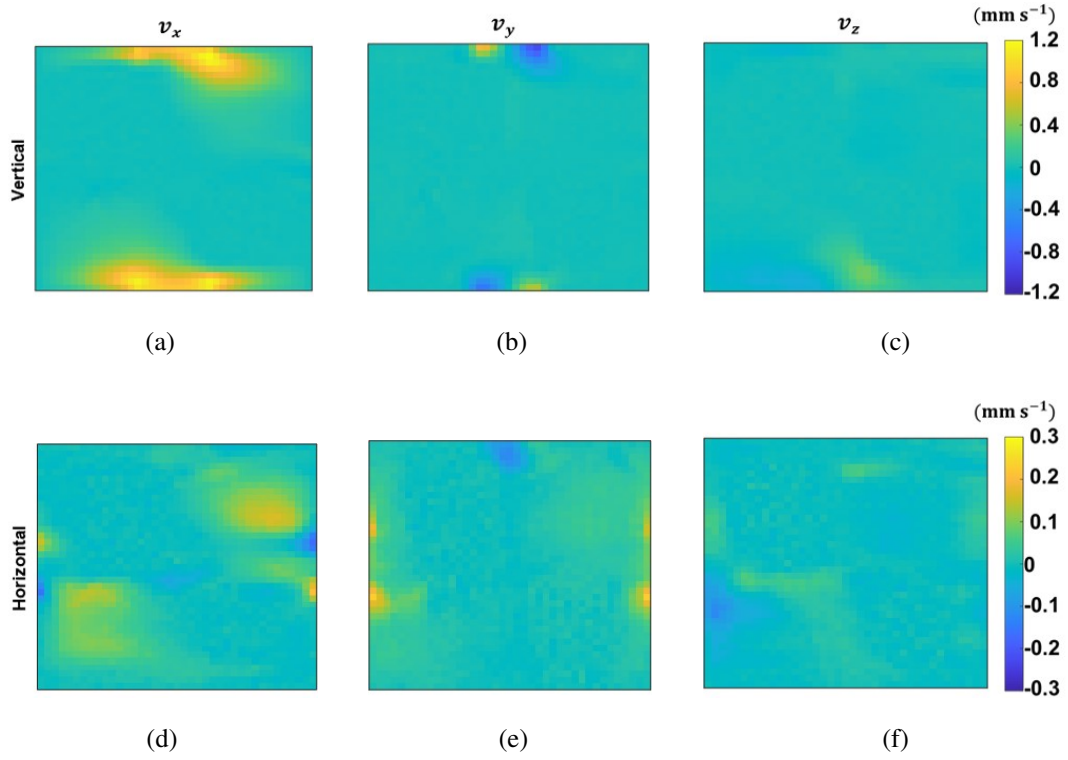


Figure 3.26: The MHD flow velocity distributions of the experimental phantom with the vertical current injection (\bar{v}_V): (a) v_{xV} , (b) v_{yV} , (c) v_{zV} . The MHD flow velocity distributions of the experimental phantom with the horizontal current injection (\bar{v}_H): (d) v_{xH} , (e) v_{yH} , (f) v_{zH} .

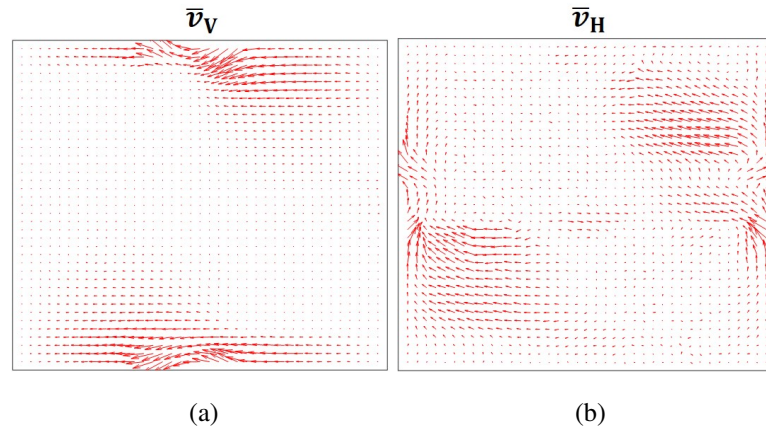


Figure 3.27: 2D arrow plot of the reconstructed MHD flow velocity, \bar{v} , distribution for the vertical and the horizontal current injection patterns. (a) \bar{v}_V (b) \bar{v}_H .

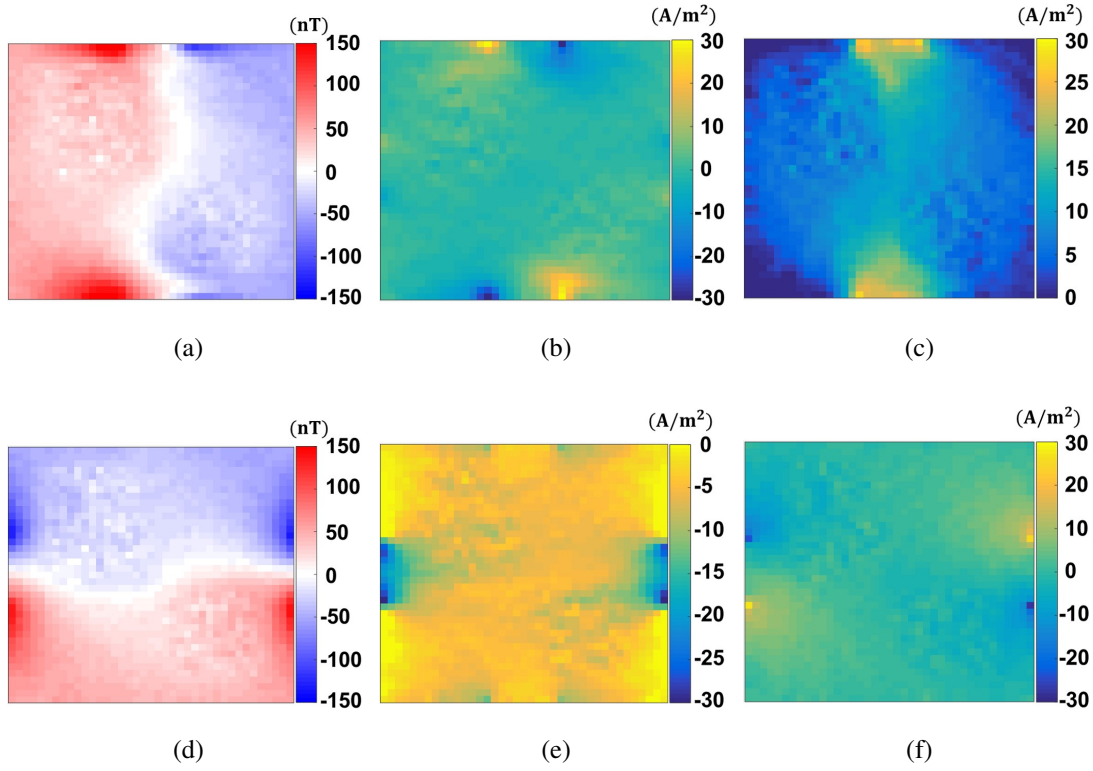


Figure 3.28: (a) The measured \tilde{B}_z distribution of the experimental phantom for vertical current injection in synchrony with the proposed pulse sequence, \tilde{B}_{z_V} , and the corresponding estimated (b) J_{px_V} and (c) J_{py_V} . (d) The measured \tilde{B}_z distribution for horizontal current injection, \tilde{B}_{z_H} , and the corresponding estimated (e) J_{px_H} (f) J_{py_H} .

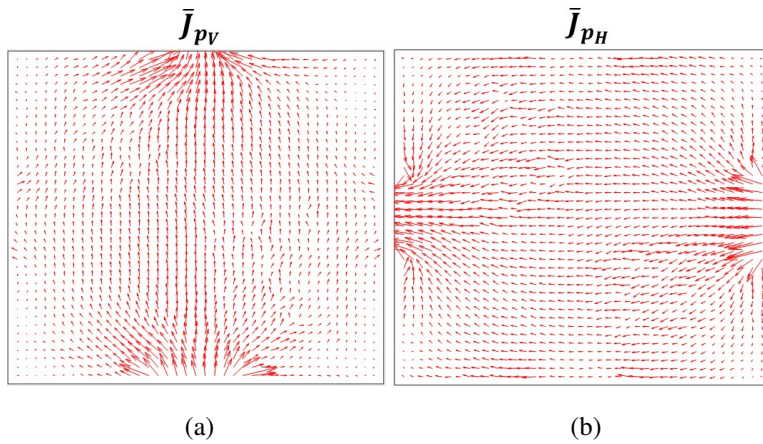


Figure 3.29: 2D arrow plot of the estimated \bar{J}_p for the vertical and the horizontal current injection patterns. (a) \bar{J}_{p_V} (b) \bar{J}_{p_H} .

3.3.1.4 The Reconstructed Conductivity Tensor Distribution

The ECDR distribution of the experimental phantom is reconstructed using the proposed dual current injection method in (2.68) from the acquired $\overline{\overline{D}}$ and the estimated $\overline{\overline{J}}_p$ for the two current injection patterns, as shown in Figure 3.30(a). The $\overline{\overline{C}}$ distribution of the imaging phantom is reconstructed using the acquired $\overline{\overline{D}}$ in Figure 3.24 and the reconstructed ECDR in Figure 3.30(a), as shown in Figure 3.30(b)-(c). The mean values of the reconstructed $\overline{\overline{C}}$ in different regions of the experimental phantom is given in Table 3.6.

The experimental results of the proposed multi-contrast imaging pulse sequence and the associated reconstruction methods are discussed in Chapter 4: Section 4.3.

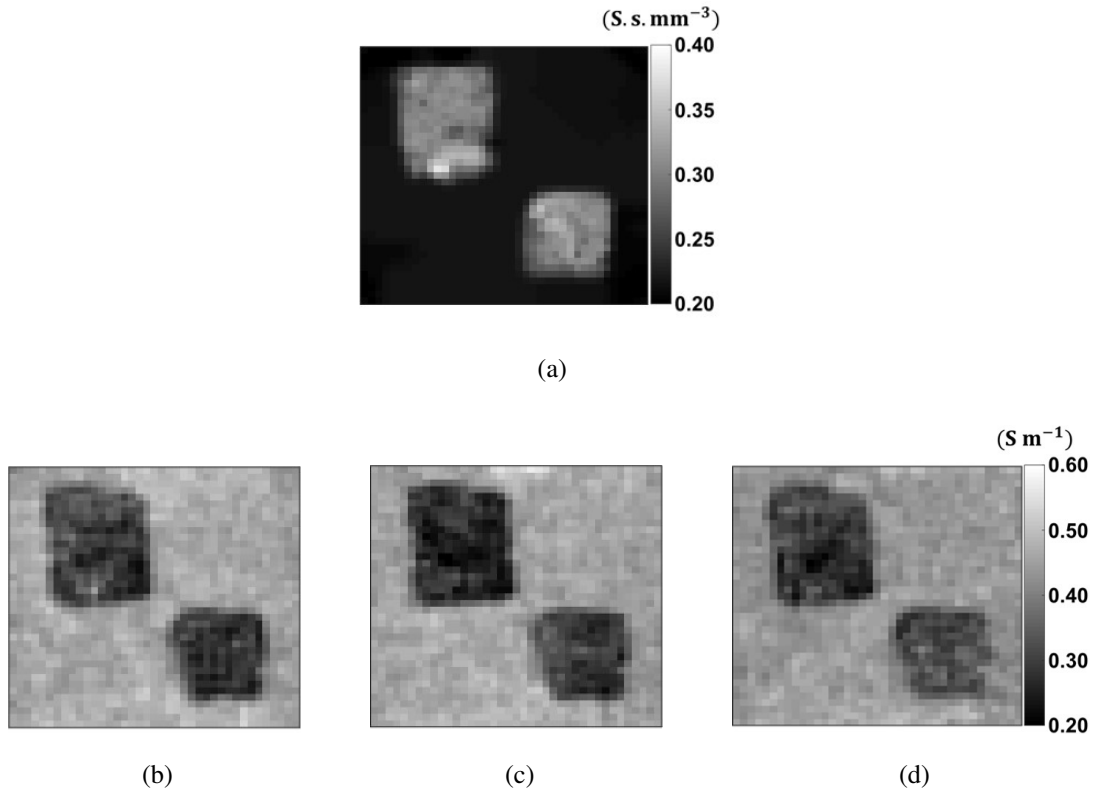


Figure 3.30: (a) The reconstructed ECDR distribution using the proposed dual current DT-MREIT in (2.68). The diagonal components of the reconstructed $\overline{\overline{C}}$ (b) σ_{xx} , (c) σ_{yy} and (d) σ_{zz} of the experimental phantom.

Table 3.6: The mean values of the reconstructed \overline{D} and \overline{C} in different regions of the experimental phantom in Figure 2.9 using the proposed multi-contrast imaging method.

Region	$d_{xx} (\times 10^{-3} \text{mm}^2 \text{s}^{-1})$	$d_{yy} (\times 10^{-3} \text{mm}^2 \text{s}^{-1})$	$d_{zz} (\times 10^{-3} \text{mm}^2 \text{s}^{-1})$
Left	1.14 ± 0.25	1.00 ± 0.27	1.05 ± 0.26
Right	1.03 ± 0.26	1.09 ± 0.26	1.16 ± 0.21
Background	2.17 ± 0.12	2.16 ± 0.12	2.10 ± 0.12
Region	$\sigma_{xx} (\text{S m}^{-1})$	$\sigma_{yy} (\text{S m}^{-1})$	$\sigma_{zz} (\text{S m}^{-1})$
Left	0.33 ± 0.05	0.29 ± 0.06	0.30 ± 0.05
Right	0.31 ± 0.06	0.32 ± 0.06	0.35 ± 0.04
Background	0.52 ± 0.02	0.53 ± 0.02	0.51 ± 0.03

CHAPTER 4

DISCUSSIONS OF THE RESULTS

In this chapter, the results from different proposed methods reported in Chapter 3 are discussed. In Section 4.1, the analytical and the experimental results of the proposed ICNE-ME-FLASH pulse sequence and its SNR and total acquisition time analysis are discussed in detail. Furthermore, the strengths and the limitations also important contributions of the proposed methods in MRCDI and DT-MREIT data acquisitions are determined. In Section 4.2, the simulated and experimental results of the proposed dual and single current DT-MREIT reconstruction algorithms are discussed and compared to the literature methods. It has also been suggested that the proposed methods can increase the clinical application of DT-MREIT. In Section 4.3, the experimental results of the proposed multi-contrast imaging pulse sequence and the associated reconstruction algorithms to acquire multiple data simultaneously and the limitations are discussed. Also, current application options are proposed to control the current dependent contrasts obtained from multi-contrast imaging pulse sequence. Finally, an EPI-based multi-contrast imaging pulse sequence is proposed to reduce the total scan time and increase the method's clinical practicality, which will be the subject of future studies.

4.1 SNR and Total Scan Time Analysis of the ICNE-ME-FLASH Pulse Sequence

All analytical analyses are performed, considering the relaxation parameters of the human brain WM tissue. However, the analyses can be applied to other biological tissues with different conductivity and MR relaxation parameters. The results obtained

for the analytical model are validated using a homogeneous saline-filled phantom with the mean conductivity and relaxation parameters of the human brain WM.

By using higher N_{EX} , motion artifact in the phase encoding direction can be reduced in the same way that multiple N_{EX} increase the SNR. But, using a higher N_{EX} especially in a multi gradient echo pulse sequence can produce extra ΔB_0 due to the intensive utilization of gradients resulting in an increased sensitivity to field inhomogeneities. Also, intensive utilization of gradients causes the temperature elevation induced around metallic prosthesis and remarkable heating of the RF shield due to the emerging eddy currents. This situation occurs especially when a higher number of N_{EX} is used with small T_R , which causes a train of successive gradient pulses using multi gradient pulse sequences such as ICNE-ME-FLASH as at the point (III) in Figure 3.2(a) with $T_R(\text{ms})/N_{EX}/\alpha = 86/25/23$ for $K = 1$.

The total acquisition time is almost identical at several points for each K as given in Figure 3.2, but the corresponding N_{EX} varies significantly. For instance, in Figure 3.2(a), the minimum acquisition time is obtained for point (III). However, there exists another point with $T_R(\text{ms})/N_{EX}/\alpha = 555/4/53$ that provides the same SNR level at almost the same acquisition time. The time difference between these two points is less than 3%. For $N_{PE} = 64$, this results in only a 4 sec longer total acquisition time, which is negligible. Moreover, the larger the T_R , the lower the frequency, which results in better estimation of DC anisotropic conductivity distribution in the low-frequency conductivity imaging methods. Furthermore, using a lower N_{EX} may provide a crucial benefit in the clinical application of current density and conductivity imaging. In MRCDI data acquisition, a high N_{EX} results in more electrical current exposure of the intended tissue. For example, for the parameter set (III) in Figure 3.2(a) with $N_{EX} = 25$ the electrical current is applied six times more than the parameter set (I) with $N_{EX} = 4$ while these two parameter sets result in \tilde{B}_z with the same SNR and total acquisition time. Therefore, the tissue heating due to the current injection will be higher using a higher N_{EX} . Hence, instead of just finding the minimum acquisition time, one may search for suboptimal points that provide similar acquisition times with smaller N_{EX} and longer T_R values for the same SNR level, as shown in the flowchart of Figure 3.4(b).

SSFP pulse sequences such as SSFP-FID, SSFP-Echo, and b-SSFP are used in MR-CDI data acquisition [23,27]. In SSFP pulse sequences, the magnetization precessing freely between consecutive RF excitation pulses without being exposed to RF. Such a steady-state of the magnetization is built-up when $T_R \ll T_1$ and $T_R < T_2$. Besides the rapid imaging and high SNR provided by SSFP pulse sequences, there are some practical restrictions in MRCDI applications. For instance, the b-SSFP pulse sequence suffers from high off-resonance sensitivity, and the acquired signal is a function of the local magnetic field. Also, the spatial signal homogeneity is a function of T_R . Increasing T_R causes degradation of the image quality and increases the banding artifacts in areas of high local field offsets [87]. Therefore, to acquire high SNR images with the least possible artifacts, low T_R with high N_{EX} values are preferred. However, using a high N_{EX} is not always desirable due to the reasons addressed above. Therefore, the proposed ICNE-FLASH and ICNE-ME-FLASH pulse sequences and the SNR analysis may enhance the clinical practicality of MRCDI and DT-MREIT methods.

The results in Figure 3.6 and Table 3.2 show the estimated $s_{\tilde{n}_j}$ and $s_{\tilde{n}_w}$ of the measured \tilde{B}_z^j and \tilde{B}_z^{comb} with different K values using the ICNE-ME-FLASH pulse sequence. The estimated $s_{\tilde{n}_j}$ and $s_{\tilde{n}_w}$ for three parameter sets with $K = 1$ is about 1 nT and 0.4 nT, respectively. Therefore, theoretically, the current-induced B_z information with the amplitudes higher than 0.4 nT can be measured using the ICNE-ME-FLASH pulse sequence when $K = 1$. The Equi-magnetic field contour plot of the simulated current-induced B_z (\hat{B}_z) of the FE model in Figure 2.7 is shown in Figure 4.1.

For $I = 0.1 - 2$ mA current injection (with $I = 0.1$ mA increments) into the FE model in Figure 2.7, the percentage area of the associated \hat{B}_z distributions that is below the estimated $s_{\tilde{n}_w}$ for $K = 0.5, 1, 2$ (Table 3.2) is shown in Figure 4.2(a). It is seen that, for $I = 2$ mA current injection $\hat{B}_z < s_{\tilde{n}_w}$ in the less than 4.7%, 2.3% and 1.2% area of the associated \hat{B}_z distribution for $K = 0.5, 1,$ and 2 the, respectively.

For $I = 0.1$ mA, about 97 % of the associated \hat{B}_z distribution is below the estimated $s_{\tilde{n}_w}$ for $K = 0.5$. This value for $K = 1$ and 2 is in the order of 60 % and 24 %, respectively. Therefore, the minimum measurable current inside the experimental phantom in Figure 2.1, with less than 10 % error for $K = 1$ and 2 can be estimated as $I = 0.4$

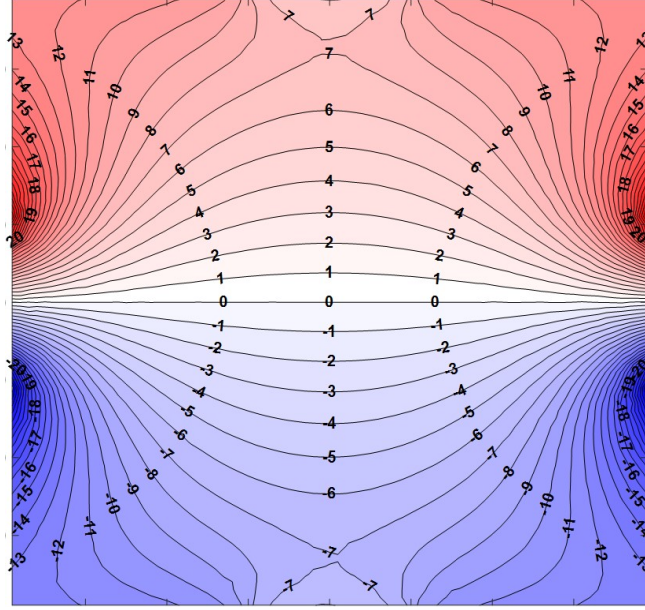


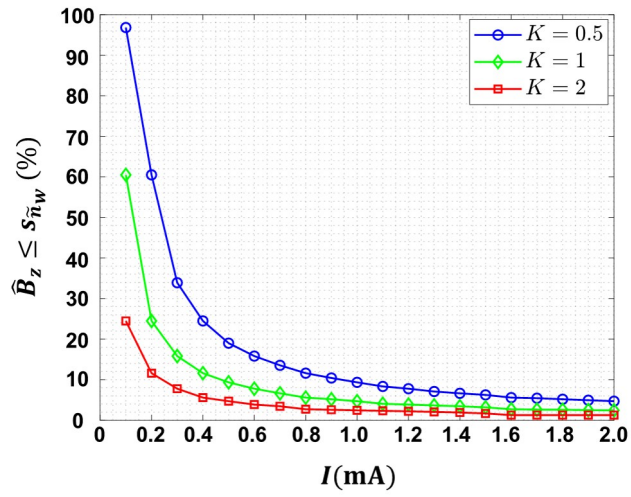
Figure 4.1: Equi-magnetic field contours of the simulated \hat{B}_z of the FE model in Figure 2.7. The conductivity of the liquid material filled in the model is $\sigma = 0.35 \text{ S m}^{-1}$ similar to the experimental phantom in Figure 2.1. $I = 2 \text{ mA}$ current is injected in the horizontal direction. The number on each contour line show the amplitude of the \hat{B}_z in nT.

and 0.2 mA, respectively. The $|\hat{B}_z|$ distribution of $I = 0.2 \text{ mA}$ current injection and the estimated $s_{\tilde{n}_w}$ for $K = 2$ is shown in Figure 4.2(b). Note that, the T_{Total} to acquire \tilde{B}_z^{comb} with $K = 2$ is about 19 minutes, where this time is about 5 minutes for $K = 1$, as given in Table 3.2. Clearly, the minimum measurable current with lower error is accessible with higher K values at the expense of longer acquisition times. Furthermore, the \tilde{B}_z distribution is also dependent on the electrical properties and the geometry of the imaging object, and the current injection electrodes.

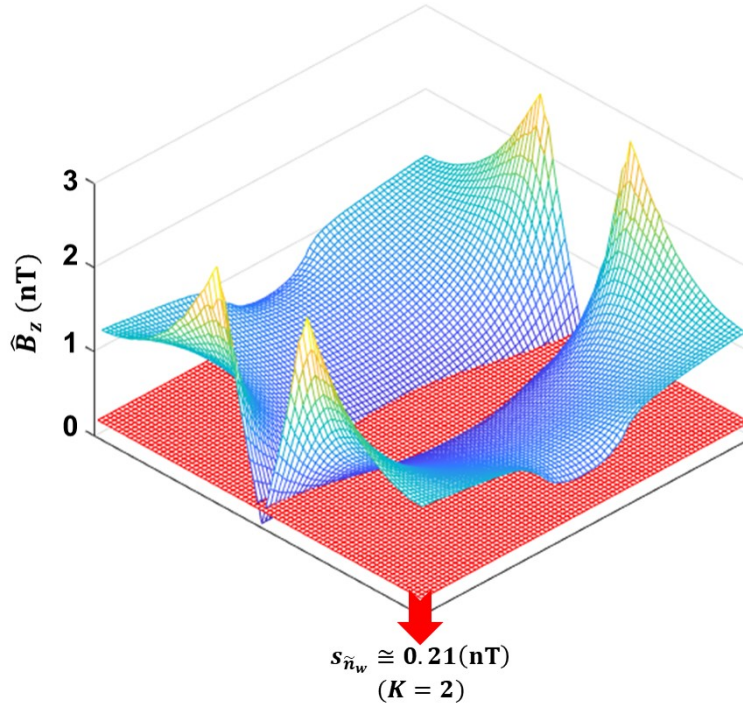
For the FLASH (or ME-FLASH) pulse sequence, the signal intensity can be maximized for a given T_R and T_1 using the Ernst angle (α_E). The steady-state signal amplitude in (2.4) can be calculated according to the Ernst angle [87] as:

$$\alpha_E = \cos^{-1}\left(e^{-\frac{T_R}{T_1}}\right) \quad (4.1)$$

In the proposed SNR analysis, it is claimed that a predetermined SNR level by choosing an appropriate K can be achieved with the minimum acquisition time using the parameters obtained from (2.10) and (2.13) for a given N_{EX} . If these parameters do



(a)



(b)

Figure 4.2: (a) The percentage area of the \hat{B}_z distribution below the estimated noise level ($\hat{B}_z \leq s_{\hat{n}_w}$) for $K = 0.5, 1, 2$ and $I = 0.1 - 2$ mA interval. (b) $|\hat{B}_z|$ distribution of $I = 0.2$ mA current injection (mesh plot) and the estimated $s_{\hat{n}_w}$ for $K = 2$ (red plane).

not satisfy (4.1), then a higher SNR level corresponding to a higher K value can be achieved with the same acquisition time by changing α_t into α_E . Consequently, N_{EX} may be decreased to achieve the desired SNR level. Therefore, the total acquisition time is reduced. Here, it is shown that the parameters obtained with the proposed procedure in (2.10) and (2.13) satisfy (4.1).

From (2.13) we have:

$$\cos \alpha_t = \frac{N_{EX} - K^2}{N_{EX} + K^2} \quad \text{and} \quad \sin \alpha_t = \frac{2K \sqrt{N_{EX}}}{N_{EX} + K^2} \quad (4.2)$$

Inserting (4.2) into (2.10) results in:

$$T_R = T_1 \ln \frac{N_{EX} - K^2}{N_{EX} + K^2} = -T_1 \ln \cos \alpha_t. \quad (4.3)$$

Hence,

$$\alpha_t = \alpha_E = \cos^{-1}(e^{-\frac{T_R}{T_1}}). \quad (4.4)$$

Therefore, it is seen that the calculated α_t satisfies the Ernst angle.

The MHD flow inside the experimental phantom during MRCDI experiments is estimated using the simulation model in Figure 2.7, and the \bar{v} distributions are shown in Figure 3.11. The results show that a shorter T_R value prevents the decreasing of \bar{v} from T_R to T_R and results in a faster steady-state with a higher amplitude. The effect of \bar{v} on the acquired \tilde{B}_z in the absence of flow encoding gradients is estimated using 3.3, as shown in Figure 3.12.

Considering the calculated $\varepsilon_{MHD B_z}$ distribution of the simulation model with $I = 2$ mA current injection and three different T_R , it is seen that the MHD-based distortion in the acquired B_z reduces by increasing T_R . The maximal MHD-based distortion occurs near the current injection electrodes due to higher \bar{v} in those regions, which is in the order of $\varepsilon_{MHD B_z}^{max} \approx 1.6$ nT for $T_R = 86$ ms. This value is in the order of the estimated noise for the acquired \tilde{B}_z distribution of the experimental phantom for multiple echoes of ICNE-ME-FLASH. Therefore, it can be said that the amount of MHD-based distortion in the acquired \tilde{B}_z images due to MHD flow can be neglected in MRCDI applications, especially when high T_R 's are used.

To summarize, using the proposed analysis, the optimum ICNE-ME-FLASH sequence parameters are estimated to achieve the desired SNR level in the shortest

acquisition time or the highest SNR in the given total scan time. Also, the proposed method provides different sets of sequence parameters (i.e., T_R , N_{EX} , α) to achieve the desired SNR level in almost the same acquisition time. Hence, alternative strategies can be adopted in determining sequence parameters instead of only using a high N_{EX} to increase the SNR level.

4.2 The Dual and a Single Current DT-MREIT Methods

One of the most successful methods to reconstruct the \overline{C} distribution of the biological tissues is DT-MREIT. Providing high quality (high SNR) \overline{J} distributions in a clinically acceptable time using the proposed ICNE-ME-FLASH pulse sequence could enhance the clinical applicability of DT-MREIT. All DT-MREIT methods reconstruct the \overline{C} distribution using \overline{D} data and the \overline{J}_p of the externally injected current in at least two linearly independent directions.

To further reduce the total scan time of DT-MREIT, reconstructing \overline{C} with the least possible current injection patterns may provide a critical advantage in the clinical applications. Therefore, the proposed single current DT-MREIT provides a significant advantage in this regard by reducing the total acquisition time, the number of current injection cables, and the contact electrodes to half.

The reconstructed ECDR values of the simulation model background using the proposed dual and a single current DT-MREIT and the method proposed in [69] show almost the same accuracy, as shown in Table 3.3 and Figure 3.14. This situation is expected because the reconstructed absolute values of ECDR distributions with all of these methods depend on a known ECDR value in the background. The inhomogeneities in the reconstructed ECDR distribution in Figure 3.14(a)-(d) using the method in [69] have smooth boundaries. However, boundaries are not smoothed in the reconstructed ECDR distributions using the proposed methods in (2.66) and (2.68) due to the piecewise constancy enforcement of TV regularization instead of the smoothing enforcement of traditional regularization methods like Tikhonov and Truncated SVD [121]. The $\|\nabla\eta\|$ information of the reconstructed ECDR using the dual and single current injections methods for noiseless case are shown in Figure 4.3.

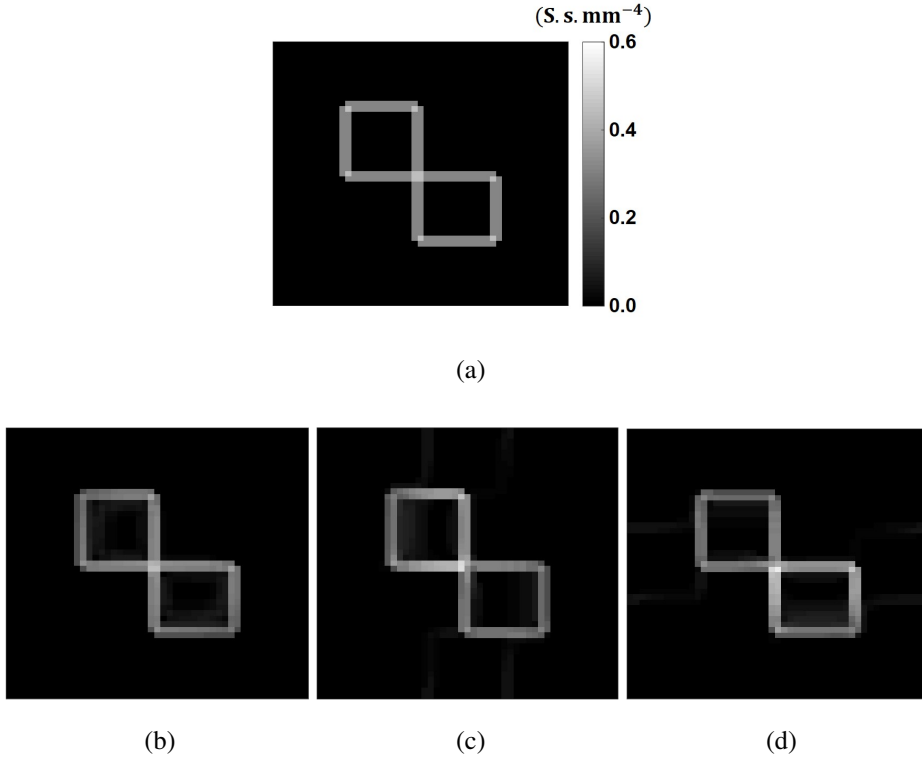


Figure 4.3: (a) The true $\|\nabla\eta\|$ distribution of the simulated ECDR in Figure 2.4. The $\|\nabla\eta\|$ distribution of the reconstructed ECDR using the proposed DT-MREIT method with (b) dual, (c) vertical, and (d) horizontal current injection patterns.

As mentioned in Section 2.4.3, the ECDR values under the current injection electrodes are overestimated using (2.60) and (2.64). Instead, an adaptive regularization scheme is utilized in (2.66) and (2.68). As a result of this modification, in the ECDR distribution obtained with dual current injections in Figure 3.14(e), the overestimation under the current injection electrodes are completely removed. Nevertheless, this effect is still barely visible in the results obtained with single current injections in Figures 3.14(i) and (m), although it is strongly suppressed. The more successful artefact elimination for the dual current injection case may arise from the fact that (2.68) includes the information coming from both directions, which causes an averaging effect.

The current density distributions of the vertical and the horizontal current injections

for the simulation model are shown in Figure 3.13. The current density values near the corner regions are lower than any other region due to the cubic geometry of the simulation model and the experimental phantom. However, the reconstructed ECDR distributions do not show any divergent characteristics on those regions, although the adaptive regularization is applied to each pixel in the imaging region. Similarly, if the conductivity of one of the embedded inhomogeneities is set to a low value, it results in a low current density distribution in that region. In this case, an accurate fit is expected since both sides of the linear system of equations in (2.57) and (2.63) are weighted by the reciprocal of the current density magnitude.

It is notable to say that the proposed adaptive regularization scheme may cause incorrect reconstructions if the medium includes abrupt changes in the current density due to abrupt changes in the conductivity even though the diffusion is approximately constant. Though it is not likely to encounter such a situation in brain tissue, it is possible to apply the adaptive regularization only to the regions under the current injection electrodes by simple modifications of (2.65) and (2.67).

Although the reconstructed ECDR distributions for a single current injection in Figure 3.14(i) and (m) are very similar to the results of dual current injections, some contrast gradients are observed in the inhomogeneity objects, in the direction perpendicular to the current injection. In comparison, there is not such a contrast gradient in the direction parallel to the current injection. This is because the off-diagonal elements of the 3×3 diffusion tensors in the simulation model are assigned as zero. Hence, the inverse of the diffusion tensors can be calculated as the reciprocals of the diagonal elements. Noting the z-component of the current density (J_{pz}) can be assumed negligible for transversal current injections, (2.56) can be expressed as:

$$\frac{\partial \ln \eta}{\partial x} \left(\frac{1}{d_{yy}} J_{py} \right) - \frac{\partial \ln \eta}{\partial y} \left(\frac{1}{d_{xx}} J_{px} \right) = \frac{\partial}{\partial x} \left(\frac{1}{d_{yy}} J_{py} \right) - \frac{\partial}{\partial y} \left(\frac{1}{d_{xx}} J_{px} \right) \quad (4.5)$$

In the vertical current injection, the x-component of the current density is almost zero ($J_{px} \approx 0$) everywhere except for the pixels close to the current injection electrodes, as shown in Figure 3.13(b). Therefore, for the pixels far from the current injection electrodes (4.5) can be expressed as:

$$\frac{\partial \ln \eta}{\partial x} \left(\frac{1}{d_{yy}} J_{py} \right) \approx \frac{\partial}{\partial x} \left(\frac{1}{d_{yy}} J_{py} \right) \quad (4.6)$$

By considering (4.6), it is seen that the information related to the variation of ECDR along the y -direction (i.e. $\frac{\partial \ln \eta}{\partial y}$) is missing in the pixels far from the electrodes. This situation is the main reason for the errors of the reconstructed ECDR values of the inhomogeneities in Table 3.3 for single current injection cases. Nevertheless, this problem does not exist for experimentally acquired data in general since the cross-correlations in the diffusion tensors of biological tissues are non-zero. Other than the model-based overestimation artefacts, the reconstructed ECDR distributions for the dual and single current injections are very similar [31].

Figure 3.14(e-p) shows that the proposed methods for dual and single current injections are quite successful in dealing with noisy data reconstruction. This is mainly due to the denoising effect of the TV regularization, which is caused by the sparse reconstructions of the solution gradients. The artefacts under the current injection electrodes due to the overestimation of the ECDR distribution become less visible in the lower SNR cases. It is known that the choice of an appropriate regularization parameter depends highly on the SNR level of the measured data [119]. Hence, in the reconstruction of each image in Figure 3.14, a different regularization parameter is utilized. Higher noise levels require much stronger regularizations, and increasing the regularization parameter causes even more suppression of the overestimation artefacts. In Figure 3.14(a-d), the background of the reconstructed ECDR distributions is getting more erroneous as the SNR decreases even though the method in [69] includes high smoothing effects.

The choice of TV regularization results in the preservation of boundaries and significant denoising in the background regions. However, the main assumption of TV regularization is the piecewise constant reconstruction of the solution. One may argue that in some situations, the structural information (here the conductivity) may change smoothly. In such a scenario, it is possible to replace TV regularization with Generalized Tikhonov regularization [121] to deal with this situation. However, some advantages of TV regularization will be lost. Hence, for in vivo applications, it is promising to propose a combined regularization scheme to take the advantage of both regularization methods [31].

Considering the RMSE vs. SNR plots of the reconstructed conductivity images of the

simulation model using the dual and single current injections shown in Figure 3.15, it is seen that the RMSE values in different regions are less than 15% for SNR levels above 35 dB. One interesting observation in Figure 3.15(d) is that the RMSE value of the left inhomogeneity in SNR = 30dB in the vertical current injection case is approximately 5% larger than the RMSE values of the right inhomogeneity in Figure 3.15(e) for the same current pattern. Such a difference also exists in the horizontal current injection, but this time the RMSE values of the right inhomogeneity in Figure 3.15(h) are larger than the RMSE values of the left inhomogeneity in Figure 3.15(g), again approximately 5%. The possible cause is that the higher conductivity in the direction of the current injection provides higher SNR levels locally. This situation exists for the right and left inhomogeneities in the vertical and horizontal current injections, respectively. Consistently, such a situation does not exist for the dual current injection case. In the case of reconstructing background conductivity distribution, both proposed methods demonstrate good noise performance with RMSE levels lower than 10% for all SNR levels given in Figure 3.15. The RMSE values in all three directions are the same due to isotropic conductivity distribution of the background.

As seen in Figures 3.18 and 3.21, the proposed methods in (2.66) and (2.68) reconstruct the ECDR distribution of the experimental phantoms Ph 1 and Ph 2 for dual and single current injections with a high accuracy except for the overestimation artefact under the current injection electrodes, which are barely visible in the single current injection cases. The fact that these artefacts are better suppressed in the dual current injection case, as explained in Section 3.2.1.1, is the averaging of information coming from two separate current injections using (2.68). Also, using relatively high regularization parameters for much stronger regularization of the noisy experimental data cause a strong suppression of the overestimation artefacts in the reconstructed ECDR distributions using the vertical and horizontal current injections.

The reconstructed ECDR values for the right inhomogeneity of Ph 1 is slightly lower than the left inhomogeneity, as seen in Figure 3.18 for the dual, vertical, and horizontal current injection patterns. The MD distribution of the tissue phantom Ph 1 is shown in Figure 2.5(c). The mean values of the right and left inhomogeneities in the MD distribution are 1.30×10^{-3} and $1.15 \times 10^{-3} \text{ mm}^2 \text{ s}^{-1}$, respectively, which shows a slightly higher diffusion of the right inhomogeneity than the left. Also, consider-

ing the current density distributions of the Ph 1 in Figure 3.16, there is no such an increase in the J_{px} and J_{py} values of the right inhomogeneity in comparison with the left. Consequently, it can be said that for the same amount of anisotropic conductivity, diffusion is higher for the right inhomogeneity. In other words, the relation between the magnitudes of the conductivity and diffusion is different for the two pieces of chicken muscle. However, this difference is not reflected in the reconstructed conductivity of the right piece since multiplying a slightly higher diffusion of the right inhomogeneity to the somewhat low reconstructed ECDR provides anisotropic conductivity almost similar to the left inhomogeneity.

The anisotropy ratio between the diagonal components of the reconstructed $\overline{\overline{C}}$ for Ph 1 is low and in the order of $AR = 1.1 - 1.22$, as given in Table 3.4. This low AR is better visualized using the ellipsoid plot in Figure 3.20. For the left inhomogeneity, the conductivity in the x-direction is slightly dominant. However, the ellipsoids have more spheroidal shape than the elliptical, as shown in the magnified region of the left muscle piece. In the case of right muscle piece, the conductivity is higher in the y-direction. Also, the AR is slightly higher in comparison with the left piece.

The reconstructed mean values of the background with isotropic distribution are consistent with the assigned conductivity value of the saline solution (0.5 S m^{-1}), which indicates that the proposed methods reconstruct the conductivity values of the background successfully.

Despite the low AR of the chicken muscle, the reconstructed conductivities along the muscle fibers for the two inhomogeneities are higher than the other two perpendicular directions. Likewise, the reconstructed conductivity values orthogonal to the muscle fibers are also close to each other for the dual and single current injections. Therefore, in the case of low AR values the proposed methods could provide good estimation of the $\overline{\overline{C}}$. Figure 3.18(b) and (c) show that background regions of the reconstructed ECDR distributions are almost constant at each image except for the overestimation artefacts. This shows that the TV regularization is a valid choice for the phantom geometry in this study. This situation also enhanced the background SNR of the reconstructed conductivity images since $\overline{\overline{C}}$ is the multiplication of reconstructed ECDR distribution with the already noisy $\overline{\overline{D}}$ data.

The results of the reconstructed $\overline{\overline{C}}$ for Ph 2 in Figure 3.22 and Table 3.5 show a higher conductivity in the x-direction of the bovine muscle than the two other perpendicular directions. Furthermore, the reconstructed conductivity values orthogonal to the muscle fibers are also close to each other, as expected. The calculated $AR = 1.7 \pm 0.6$ shows a stronger anisotropy in comparison with the chicken muscles in Ph 1. The ellipsoid plot of the reconstructed $\overline{\overline{C}}$ of Ph 2 in Figure 3.23 better visualizes this stronger anisotropy.

Considering the results in Figures 3.18-3.23 and Tables 3.4-3.5, it can be inferred that the proposed methods with dual and single current injections provide acceptable estimations of $\overline{\overline{C}}$ of the experimental phantoms.

In MRCDI experiments with a single current injection, the total scan time of the ICNE-ME-FLASH pulse sequence to acquire \tilde{B}_z^{comb} distribution with $K = 2$ and $K = 1.5$ SNR levels is about 19 and 27 minutes for Ph 1 and Ph 2, respectively. The same procedure with two current injections lasts twice as much. To increase the SNR level and the resolution of the acquired current density images in the clinical applications, a higher number of N_{EX} and N_{PE} are required, demanding longer scan times. Therefore, the time gained by a single current injection becomes even more significant. Consequently, the reduction in the number of the current injection cables, the contact electrodes, and the total scan time could lead to the routine use of DT-MREIT in clinical practice.

4.3 Multi Physics Multi-Contrast Imaging

The results of the proposed multi-contrast imaging method of the experimental phantom in Figure 2.9 are shown in Figures 3.24-3.30. The proposed multi-contrast imaging pulse sequence in Figure 2.8 using the parameters given in Table 2.5 provides $\overline{\overline{D}}$, \tilde{B}_z and the MHD flow velocity (\bar{v}) information simultaneously. The $\overline{J_p}$ and $\overline{\overline{C}}$ are then estimated and reconstructed from the measured \tilde{B}_z and the acquired $\overline{\overline{D}}$. The mean values of the reconstructed $\overline{\overline{D}}$ for the left and right inhomogeneities in Table 3.6 show the amount of mean diffusion anisotropy in the muscle pieces. The colored FA map in Figure 3.24 shows that the main direction of diffusion for the left and right

muscle pieces is in the x- and z- directions, respectively.

The reconstructed $\overline{\overline{D}}$ distributions using the data sets with and without current injection are almost identical except for some minor artifacts seen just nearside the muscle pieces in the diffusion tensor distributions obtained with current injection, especially in the image with vertical current injection pattern in Figure 3.24(d) (artifacts are encircled by the red circles). As stated before, the MHD flow causes a coherent motion of the medium particles. These artifacts emerge due to the disruption in the coherent motion of liquid particles colliding the muscle pieces. When liquid particles under the effect of MHD flow collide with an obstacle, the motion behavior of the particles is no longer a coherent motion. In the voxels beside the obstacle, the particles show random motion characteristics like the Brownian motion of water molecules due to self-diffusion. The 2D arrow plot of the reconstructed $\overline{\overline{v}}_v$ is shown in Figure 3.27(a). Therefore, the voxels in these regions are brighter in the reconstructed $\overline{\overline{D}}$ distributions of vertical current injection. The same phenomenon is observed under the current injection electrodes of the reconstructed $\overline{\overline{D}}$ due to very high MHD flow, which causes disruption of the coherent motion in those regions and affects the magnitude signal like diffusion. However, by injecting current pulses with $I = 10$ mA amplitude and despite the obstacles with sharp edges, these artifacts appear just in a couple of pixels nearside the muscle pieces.

The η and the $\overline{\overline{C}}$ distributions are reconstructed using the proposed dual-current DT-MREIT method. The mean values of the reconstructed $\overline{\overline{C}}$ for the left and right pieces in Table 3.6 show a conductivity anisotropy similar to the acquired $\overline{\overline{D}}$ which is expected since the $\overline{\overline{C}}$ and $\overline{\overline{D}}$ share eigenvectors in a porous medium as given in (1.23).

To acquire MHD flow information, the MR signal is acquired twice with opposing current injection polarities and diffusion encoding directions in (2.74). Hence, $\overline{\overline{D}}$ can be reconstructed twice with these two data sets. Using the average of these two $\overline{\overline{D}}$ distributions enhances the SNR by a factor of $\sqrt{2}$.

The \overline{v} distribution for both vertical and horizontal current injections are calculated from the extracted $\phi_{MHD_{g_d}}$ using (2.76), as shown in Figures 3.26. One important observation is that the maximum values of \overline{v} distributions in the vertical current injection (\overline{v}_v) are almost four times larger than those for the horizontal current injection

profile (\bar{v}_H), although the injected current pulses for both cases have the same amplitude and duration.

One reason for this difference in the reconstructed \bar{v} distributions may arise from the placement of the muscle pieces, which affects the flow dynamics differently in the vertical and horizontal current injection patterns. Figure 3.24 shows a gap between the two muscle pieces in the vertical current injection pattern. Therefore, the electrical current can flow directly between the current injecting electrodes without forming a significant component in the z-direction. Equation (2.69) shows that the current density component that flows in the z-direction (J_z) will not produce Lorentz force (\bar{F}) hence cause a decrease in the \bar{v} distribution. Since there is no such apparent gap between the muscle pieces for horizontal current injection pattern, a significant component of the current density is in the z-direction, which causes a four-times reduction of \bar{F} and consequently \bar{v}_H distributions in comparison with \bar{v}_V .

Another factor, may cause this difference is the effect of gravity on the fluid particles. For horizontal current injection, the flow velocity is dominant in the vertical direction. Therefore, the vertical motion of the fluid particles due to Lorentz force can be affected by gravity. In other words, the gravity itself (or the frictional forces between fluid and phantom such as adhesion) may be acting as an opponent to the Lorentz force for the horizontal current injection. Considering the results obtained, it can be said that the proposed multi-contrast imaging pulse sequence, together with the proposed data acquisition scheme and reconstruction methods, can form the basis of the magnetic resonance multi-physics multi-contrast imaging.

It is notable to say that by managing the simultaneous current injection during multi-contrast data acquisition, it possible to control the contrasts related to the injected current. Figure 4.4 demonstrates the proposed multi-contrast pulse sequence with a dual current application scheme. Application of current pulses before and after the flow encoding gradients makes it possible to manage the amount of the accumulated phase due to the \tilde{B}_z and the \bar{v} . The accumulated phase due to the \tilde{B}_z can be increased by applying current pulses with opposite polarities before and after flow encoding gradients. Current application with the same duration and magnitude but with opposite polarities on either side of the 180° RF pulse causes a twofold phase accumulation

compared to the single current application scheme in Figure 2.8. On the other hand, injecting current pulses with opposite polarities before and after flow encoding gradients eliminates the MHD flow velocity since the emerging force due to interaction between \bar{J} and B_0 take opposite directions at each T_R .

One may argue that the injected current with opposite polarity after applying flow encoding gradients does not affect the MHD flow distribution since the MHD flow is already encoded to the MR signal by flow encoding gradients before applying the second current pulse. However, note that the \bar{v} increases gradually during the imaging process from the first excitation through a steady-state level. By reaching the steady-state, \bar{v} is no longer changes. Reversing the current polarity after the flow encoding gradients at each T_R prevents the formation of the steady-state for \bar{v} . Conversely, by applying electrical current pulses with the same polarities on either side of the 180° RF pulse, the accumulated phase associated with the injected current before and after flow encoding gradients cancel out each other. However, the MHD-based phase increases resulting in a fast reach to the steady-state with a higher amplitude. Therefore, different current application topologies can be used according to the purpose of the experiment. Also, the amplitude and duration (I and T_C) of the injected current before and after the flow encoding gradients need not be the same. For instance, the current injection after the flow encoding gradients can be prolonged to the end of the readout gradient as it is done in the ICNE method to increase the accumulated phase to the injected current.

The total acquisition time to acquire the multi-contrast distributions using the proposed pulse sequence with the parameters in Table 2.5 is about 15 min, which is a clinically acceptable scan time. Nevertheless, to provide high-quality (high SNR) images in the clinical application, the total scan time will increase. Therefore, by expanding the multi-contrast imaging method to a pulse sequence with a high acquisition speed like the SS-SE-EPI, the total acquisition time will reduce considerably. However, high-speed EPI based pulse sequences suffer from off-resonance related artifacts and distortions, as explained in Section 2.3, and correction methods are required to acquire distortion-free data. Therefore, the effects of these corrections on each contrast must be examined carefully. Specially, for the contrasts which are reconstructed from the acquired MR phase data.

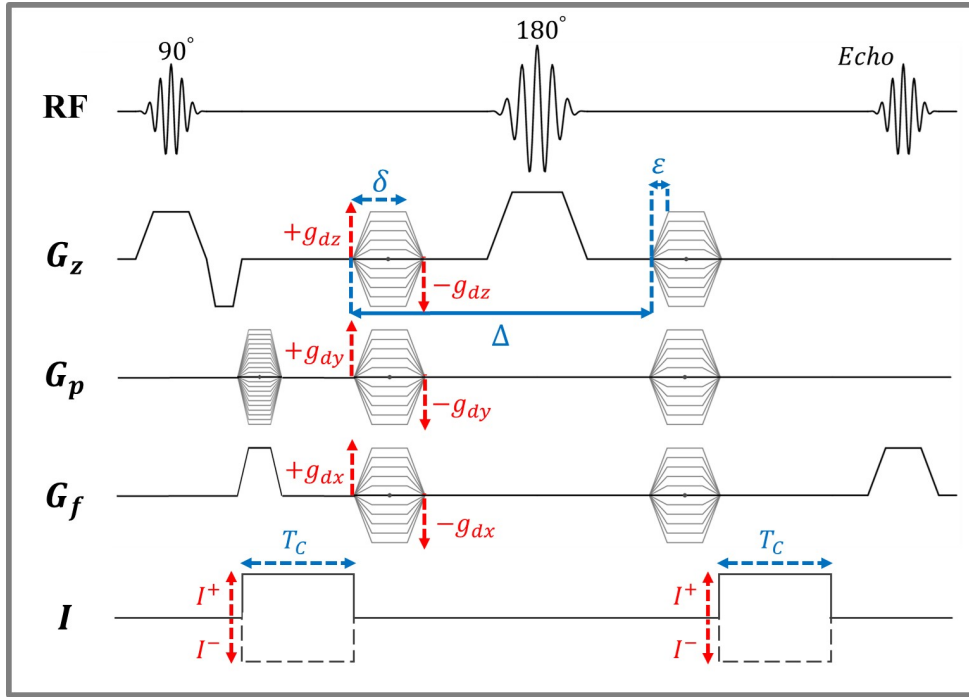


Figure 4.4: The schematic diagram of the multi-contrast imaging pulse sequence with a dual current injection scheme. g_d 's are the magnitudes of the diffusion encoding gradients. I and T_C are the amplitude and the duration of the injected current, respectively. Δ , δ and ϵ are defined in Section 1.3. G_z , G_p and G_f are the slice selection, phase encoding, and frequency encoding gradients, respectively.

The initial design of such a multi-contrast EPI based pulse sequence is shown in Figure 4.5. As explained in Section 2.3 the relatively long readout period of the EPI based pulse sequences prolongs T_E and forces a narrow BW per pixel in the phase encoding direction. A narrow BW results in a high sensitivity to the off-resonance related factors such as chemical shift and field inhomogeneity effects, resulting in significant geometric distortions and phase errors [34, 138]. A method is proposed in [139] to remove the geometric distortions and phase errors that cause pixel shifts proportional to local resonance offsets. Also, the Nyquist ghost artifacts due to the time-reversal asymmetry between the even and odd echoes result in SNR reduction and degradation of the image quality [140, 141] must be corrected in the EPI-based multi-contrast imaging pulse sequence.

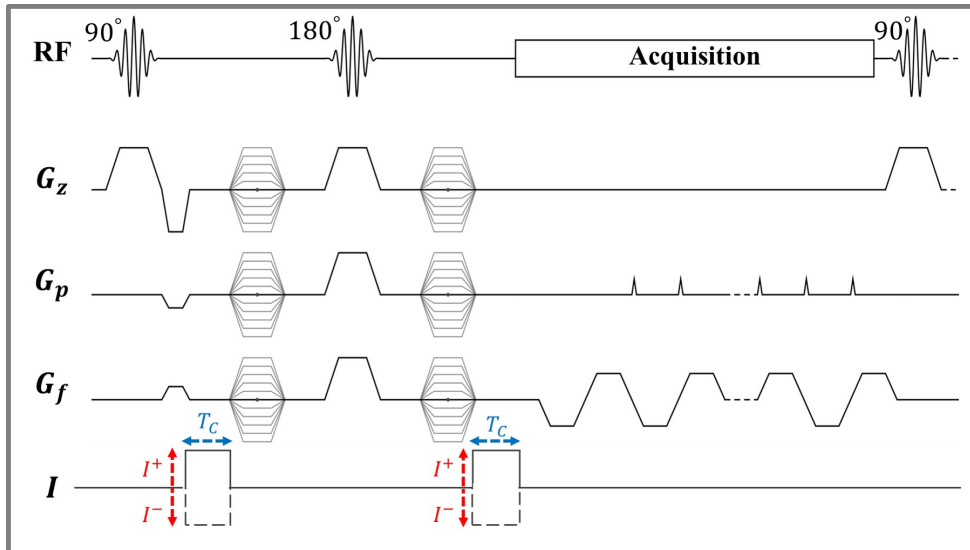


Figure 4.5: The schematic diagram of the EPI based multi-contrast imaging pulse sequence.

CHAPTER 5

CONCLUSION

Tissue-dependent factors, and safety concerns limit the current injection duration and its amplitude in the in vivo applications of MRCDI and DT-MREIT. On the other hand, the clinical applicability of these methods is highly dependent on the sensitivity of the acquired current-induced \tilde{B}_z images. Since the FLASH is an efficient pulse sequence to acquire high SNR images per measurement time, the combination of the ICNE technique with the FLASH is proposed in this study for the MRCDI and DT-MREIT data acquisitions. Also, by developing the ICNE-ME-FLASH pulse sequence, it is possible to take the advantages of combining the multiple echoes to achieve \tilde{B}_z^{comb} distribution with a higher SNR than the one achievable with a single echo acquisition.

Furthermore, a new analysis is developed for ICNE-ME-FLASH to use the proposed sequence more efficiently and determine its limits. Using the proposed analysis, the optimum ICNE-ME-FLASH sequence parameters are estimated to achieve the desired SNR level in the shortest acquisition time or the highest SNR in the given total scan time. Also, the proposed method provides different sets of sequence parameters (i.e., T_R , N_{EX} , α) to achieve the desired SNR level in almost the same acquisition time. Hence, alternative strategies can be adopted in determining sequence parameters instead of only using a high number of N_{EX} to increase the SNR level. Using a lower N_{EX} provides a crucial benefit in the clinical application of MRCDI and DT-MREIT. In MRCDI data acquisition, a high N_{EX} results in injecting more current to the tissue. For example, \tilde{B}_z distributions with SNR= 30 dB are acquired from the imaging phantom in a total time of 5 minutes with $N_{EX} = 4$ and 25. The electrical current is applied six times more with $N_{EX} = 25$, which causes a higher electri-

cal exposure of the intended tissue and consequently a temperature elevation. Using the ICNE-ME-FLASH pulse sequence and the results of the proposed SNR and total acquisition time analysis, the \tilde{B}_z^{comb} distributions of the experimental phantom associated with $I = 200$ and $400 \mu\text{A}$ current injection is measured with the estimated SNR of 13 dB in the total scan times less than 19 and 5 minutes, respectively.

The calculated ε_{MHDB_z} distributions of the simulation model with $I = 2$ mA current injection for three different T_R show that the effect of MHD flow on the acquired \tilde{B}_z in the absence of flow encoding gradients is in the order of 1.6 nT for $T_R = 86$ ms, which is four times the estimated $s_{\tilde{n}_w}$ for $K = 1$ (SNR = 30 dB). But for $T_R = 555$ ms the calculated $\varepsilon_{MHDB_z} = 0.5$ nT which is in the order of $s_{\tilde{n}_w}$ for $K = 1$. Therefore, utilizing a lower N_{EX} could reduce the effect of MHD flow on the acquired \tilde{B}_z distributions of the imaging objects with low dynamic viscosity.

It is known that the intensive utilization of the gradient pulses cause spatial and temporal variations of the MR main magnetic field (ΔB_0), which is consistent with the resistive heating of the magnet structures. On the other hand, the interaction of the rapidly switched gradient fields with other MR scanner structures, especially when an intensive number of gradient pulses are used, causes emerging high eddy currents. The emerging eddy currents generate magnetic fields, which cause problems in the acquired MR signal. Also, a remarkable temperature increase occurs due to eddy current heating of the RF shield.

In this study, it is shown that the intensive utilization of the gradients in the MRCDI experiments using the ICNE-ME-FLASH pulse sequence with high N_{EX} and short T_R values results in a shift in the mean of the additive Gaussian noise of the measured \tilde{B}_z^j distributions. The amount of ΔB_0 shift and the noise mean slip during 50 consecutive MRCDI experiments using ICNE-ME-FLASH with $N_E = 9$, $N_{EX} = 4$ and $T_R = 136$ is calculated as 10 nT for the imaging phantom with $I = 2$ mA current injection. By increasing the N_{EX} value to 32 the estimated ΔB_0 (noise mean) increases to 70 nT. Therefore, the sequence parameter sets with low N_{EX} which are provided using the proposed SNR and total acquisition time analysis, could prevent the formation of extra ΔB_0 shifts and the temperature elevation during MRCDI experiments with ICNE-ME-FLASH pulse sequence.

The ICNE-ME-FLASH pulse sequence also is used in the DT-MREIT data acquisition to provide \bar{J} distributions of the biological tissue phantoms. The estimated \bar{J} along with the acquired \bar{D} data is used to reconstruct the \bar{C} distributions of the imaging phantoms using the proposed reconstruction algorithms with dual and single current injection.

The proposed single current DT-MREIT reconstructs the conductivity tensor distributions of the simulated data with SNR of 35 dB with the RMSE error less than 10 % in different regions of the simulation model. In the case of experimental data, the proposed single current DT-MREIT reconstructed the \bar{C} distributions of the two biological tissue phantoms from the acquired \tilde{B}_z^{comb} distribution with the estimated SNR of 36 dB and 32 dB with RMSE value less than 5 % in comparison with the proposed dual current DT-MREIT.

Reconstructing the \bar{C} distribution by only a single current injection increase the clinical practicality of DT-MREIT by reducing the total acquisition time, the number of cables, and contact electrodes. For instance, the total acquisition time for the MRCDI experiment of the Ph 1 in Figure 2.5 to acquire \tilde{B}_z^{comb} with SNR=36 dB is about 19 minutes for each current injection pattern. The total scan time of the MRCDI experiment lasts twice as much for two current injections, which is not a clinically acceptable scan time. All these improvements in the pulse sequence and the reconstruction algorithms of MRCDI and DT-MREIT methods increase the clinical potential of the current density and conductivity imaging.

In this study, for the first time, a pulse sequence is designed and implemented to combine the DTI and MRCDI data acquisitions. Combining DTI and MRCDI data acquisitions cause emerging a third contrast: the MHD flow velocity (\bar{v}) distribution. Therefore, five different contrasts, i.e., \bar{D} , \tilde{B}_z , \bar{J} , \bar{C} and \bar{v} can be extracted individually from the acquired signal using the proposed reconstruction method for each contrast.

A DW-SE pulse sequence with simultaneous current injection is used for multi-contrast imaging to avoid geometric distortions and artifacts associated with the emerging eddy currents in the acquired signal of the EPI-based DTI pulse sequences such as the SS-SE-EPI. Since four-fifth of the multiple contrasts are reconstructed from the

acquired MR phase images, intensive corrections of the phase images are required if EPI-based pulse sequences are utilized. The total scan time to acquire multi-contrast data from the biological tissue phantom in Figure 2.9 with the estimated SNR of 24 dB is about 15 minutes using the sequence parameters in Table 2.5. Considering the tissue dependent factors which limits the amplitude of the injected current to a few mA, to increase the SNR, a higher N_{EX} value must be utilized, which increases the total scan time drastically. Therefore, using EPI-based pulse sequences to acquire high SNR multi-contrast data in a clinically acceptable scan time is inevitable. Therefore, further studies will focus on implementing the EPI-based multi-contrast imaging pulse sequence and the associated reconstruction methods.

REFERENCES

- [1] A. J. Surowiec, S. S. Stuchly, J. R. Barr, and A. Swarup, “Dielectric properties of breast carcinoma and the surrounding tissues,” *IEEE Transactions on Biomedical Engineering*, vol. 35, no. 4, pp. 257–263, 1988.
- [2] W. T. Joines, Y. Zhang, C. Li, and R. L. Jirtle, “The measured electrical properties of normal and malignant human tissues from 50 to 900 MHz,” *Medical physics*, vol. 21, no. 4, pp. 547–550, 1994.
- [3] D. Holder, “Detection of cerebral ischaemia in the anaesthetised rat by impedance measurement with scalp electrodes: implications for non-invasive imaging of stroke by electrical impedance tomography,” *Clinical Physics and Physiological Measurement*, vol. 13, no. 1, p. 63, 1992.
- [4] M. A. Fallert, M. S. Mirotznik, S. W. Downing, E. B. Savage, K. R. Foster, M. E. Josephson, and D. K. Bogen, “Myocardial electrical impedance mapping of ischemic sheep hearts and healing aneurysms.,” *Circulation*, vol. 87, no. 1, pp. 199–207, 1993.
- [5] P. Hömmen, J.-H. Storm, N. Höfner, and R. Körber, “Demonstration of full tensor current density imaging using ultra-low field MRI,” *Magnetic resonance imaging*, vol. 60, pp. 137–144, 2019.
- [6] A. Roy, B. Baxter, and B. He, “High-definition transcranial direct current stimulation induces both acute and persistent changes in broadband cortical synchronization: a simultaneous tDCS-EEG study,” *IEEE Transactions on Biomedical Engineering*, vol. 61, no. 7, pp. 1967–1978, 2014.
- [7] P. C. Miranda, M. Lomarev, and M. Hallett, “Modeling the current distribution during transcranial direct current stimulation,” *Clinical neurophysiology*, vol. 117, no. 7, pp. 1623–1629, 2006.

- [8] T. Wagner, F. Fregni, S. Fecteau, A. Grodzinsky, M. Zahn, and A. Pascual-Leone, “Transcranial direct current stimulation: a computer-based human model study,” *Neuroimage*, vol. 35, no. 3, pp. 1113–1124, 2007.
- [9] T. Neuling, S. Wagner, C. H. Wolters, T. Zaehle, and C. S. Herrmann, “Finite-element model predicts current density distribution for clinical applications of tDCS and tACS,” *Frontiers in psychiatry*, vol. 3, p. 83, 2012.
- [10] P. Limousin, P. Krack, P. Pollak, A. Benazzouz, C. Ardouin, D. Hoffmann, and A. L. Benabid, “Electrical stimulation of the subthalamic nucleus in advanced parkinson’s disease,” *New England Journal of Medicine*, vol. 339, no. 16, pp. 1105–1111, 1998.
- [11] M. D. Johnson, H. H. Lim, T. I. Netoff, A. T. Connolly, N. Johnson, A. Roy, A. Holt, K. O. Lim, J. R. Carey, J. L. Vitek, *et al.*, “Neuromodulation for brain disorders: challenges and opportunities,” *IEEE Transactions on Biomedical Engineering*, vol. 60, no. 3, pp. 610–624, 2013.
- [12] K. S. Utz, V. Dimova, K. Oppenländer, and G. Kerkhoff, “Electrified minds: transcranial direct current stimulation (tdcs) and galvanic vestibular stimulation (gvs) as methods of non-invasive brain stimulation in neuropsychology—a review of current data and future implications,” *Neuropsychologia*, vol. 48, no. 10, pp. 2789–2810, 2010.
- [13] D. Miklavčič, N. Pavšelj, and F. X. Hart, “Electric properties of tissues,” *Wiley encyclopedia of biomedical engineering*, 2006.
- [14] J. Liu, Y. Wang, U. Katscher, and B. He, “Electrical properties tomography based on B_1 maps in MRI: Principles, applications, and challenges,” *IEEE Transactions on Biomedical Engineering*, vol. 64, no. 11, pp. 2515–2530, 2017.
- [15] M. S. George, S. H. Lisanby, and H. A. Sackeim, “Transcranial magnetic stimulation: applications in neuropsychiatry,” *Archives of general psychiatry*, vol. 56, no. 4, pp. 300–311, 1999.
- [16] C. Pappone, S. Rosanio, G. Oreto, M. Tocchi, F. Gugliotta, G. Vicedomini, A. Salvati, C. Dicandia, P. Mazzone, V. Santinelli, *et al.*, “Circumferential

radiofrequency ablation of pulmonary vein ostia: a new anatomic approach for curing atrial fibrillation,” *Circulation*, vol. 102, no. 21, pp. 2619–2628, 2000.

- [17] G. Scott, M. Joy, R. Armstrong, and R. Henkelman, “Sensitivity of magnetic-resonance current-density imaging,” *Journal of Magnetic Resonance (1969)*, vol. 97, no. 2, pp. 235–254, 1992.
- [18] H. H. Eroğlu, M. Sadighi, and B. M. Eyüboğlu, “Induced current magnetic resonance electrical conductivity imaging with oscillating gradients,” *IEEE Transactions on Medical Imaging*, vol. 37, no. 7, pp. 1606–1617, 2018.
- [19] U. Mikac, F. Demšar, K. Beravs, and I. Serša, “Magnetic resonance imaging of alternating electric currents,” *Magnetic resonance imaging*, vol. 19, no. 6, pp. 845–856, 2001.
- [20] C. Park, B. I. Lee, O. Kwon, and E. J. Woo, “Measurement of induced magnetic flux density using injection current nonlinear encoding (ICNE) in MREIT,” *Physiological Measurement*, vol. 28, no. 2, p. 117, 2006.
- [21] A. S. Minhas, E. J. Woo, and S. Y. Lee, “Magnetic flux density measurement with balanced steady state free precession pulse sequence for MREIT: a simulation study,” in *2009 Annual International Conference of the IEEE Engineering in Medicine and Biology Society*, pp. 2276–2278, IEEE, 2009.
- [22] Y. Han, Z. Meng, W. Jeong, Y. Kim, A. Minhas, H. Kim, H. Nam, O. Kwon, and E. Woo, “MREIT conductivity imaging of canine head using multi-echo pulse sequence,” in *J. Phys. Conf. Ser.*, vol. 224, pp. 7541–7556, 2010.
- [23] H. Lee, W. C. Jeong, H. J. Kim, E. J. Woo, and J. Park, “Alternating steady state free precession for estimation of current-induced magnetic flux density: A feasibility study,” *Magnetic Resonance in Medicine*, vol. 75, no. 5, pp. 2009–2019, 2016.
- [24] H. Lee, C. H. Sohn, and J. Park, “Current-induced alternating reversed dual-echo-steady-state for joint estimation of tissue relaxation and electrical properties,” *Magnetic Resonance in Medicine*, vol. 78, no. 1, pp. 107–120, 2017.
- [25] T. DeMonte, R. Yoon, D. Jorgenson, and M. Joy, “A system for in-vivo cardiac defibrillation current density imaging in a pig,” in *Proceedings of the 25th*

Annual International Conference of the IEEE Engineering in Medicine and Biology Society (IEEE Cat. No. 03CH37439), vol. 1, pp. 175–178, IEEE, 2003.

- [26] T. I. Oh, W. C. Jeong, J. E. Kim, S. Z. Sajib, H. J. Kim, O. I. Kwon, and E. J. Woo, “Noise analysis in fast magnetic resonance electrical impedance tomography (MREIT) based on spoiled multi gradient echo (SPMGE) pulse sequence,” *Physics in Medicine & Biology*, vol. 59, no. 16, p. 4723, 2014.
- [27] C. Göksu, K. Scheffler, P. Ehses, L. G. Hanson, and A. Thielscher, “Sensitivity analysis of magnetic field measurements for magnetic resonance electrical impedance tomography (MREIT),” *Magnetic resonance in medicine*, vol. 79, no. 2, pp. 748–760, 2018.
- [28] V. E. Arpinar, M. J. Hamamura, E. Degirmenci, and L. Muftuler, “MREIT experiments with 200 μ A injected currents: a feasibility study using two reconstruction algorithms, smm and harmonic B_z ,” *Physics in Medicine & Biology*, vol. 57, no. 13, p. 4245, 2012.
- [29] A. Haase, J. Frahm, D. Matthaei, W. Hanicke, and K.-D. Merboldt, “FLASH imaging. rapid NMR imaging using low flip-angle pulses,” *Journal of Magnetic Resonance (1969)*, vol. 67, no. 2, pp. 258–266, 1986.
- [30] G. Helms and P. Dechent, “Increased snr and reduced distortions by averaging multiple gradient echo signals in 3D FLASH imaging of the human brain at 3T,” *Journal of Magnetic Resonance Imaging: An Official Journal of the International Society for Magnetic Resonance in Medicine*, vol. 29, no. 1, pp. 198–204, 2009.
- [31] M. Sadighi, M. Şişman, B. C. Açıkgöz, H. H. Eroğlu, and B. M. Eyüboğlu, “Low-frequency conductivity tensor imaging with a single current injection using DT-MREIT,” *Physics in Medicine & Biology*, vol. 66, no. 5, 2021.
- [32] D. Le Bihan, J. F. Mangin, C. Poupon, C. A. Clark, S. Pappata, N. Molko, and H. Chabriat, “Diffusion tensor imaging: concepts and applications,” *Journal of Magnetic Resonance Imaging: An Official Journal of the International Society for Magnetic Resonance in Medicine*, vol. 13, no. 4, pp. 534–546, 2001.

- [33] D. Le Bihan, “Molecular diffusion nuclear magnetic resonance imaging.,” *Magnetic resonance quarterly*, vol. 7, no. 1, p. 1, 1991.
- [34] M. A. Bernstein, K. F. King, and X. J. Zhou, *Handbook of MRI pulse sequences*. Elsevier, 2004.
- [35] D. McClymont, I. Teh, and J. E. Schneider, “The impact of signal-to-noise ratio, diffusion-weighted directions and image resolution in cardiac diffusion tensor imaging—insights from the ex-vivo rat heart,” *Journal of Cardiovascular Magnetic Resonance*, vol. 19, no. 1, pp. 1–10, 2017.
- [36] B. Kincses, T. Spisák, P. Faragó, A. Király, N. Szabó, D. Veréb, K. Kocsis, B. Bozsik, E. Tóth, L. Vécsei, *et al.*, “Brain MRI diffusion encoding direction number affects tract-based spatial statistics results in multiple sclerosis,” *Journal of Neuroimaging*, 2020.
- [37] K. V. Mardia, *Multivariate analysis*. Academic Press London; New York, 1979.
- [38] W. Van Hecke, L. Emsell, and S. Sunaert, *Diffusion tensor imaging: a practical handbook*. Springer, 2015.
- [39] L. Minati and W. P. Węglarz, “Physical foundations, models, and methods of diffusion magnetic resonance imaging of the brain: A review,” *Concepts in Magnetic Resonance Part A: An Educational Journal*, vol. 30, no. 5, pp. 278–307, 2007.
- [40] J. D. Tournier, S. Mori, and A. Leemans, “Diffusion tensor imaging and beyond,” *Magnetic resonance in medicine*, vol. 65, no. 6, p. 1532, 2011.
- [41] W. Wu and K. L. Miller, “Image formation in diffusion MRI: a review of recent technical developments,” *Journal of Magnetic Resonance Imaging*, vol. 46, no. 3, pp. 646–662, 2017.
- [42] P. Mukherjee, J. Berman, S. Chung, C. Hess, and R. Henry, “Diffusion tensor mr imaging and fiber tractography: theoretic underpinnings,” *American journal of neuroradiology*, vol. 29, no. 4, pp. 632–641, 2008.

- [43] A. L. Benabid, P. Pollak, D. Hoffmann, C. Gervason, M. Hommel, J. Perret, J. De Rougemont, and D. Gao, “Long-term suppression of tremor by chronic stimulation of the ventral intermediate thalamic nucleus,” *The Lancet*, vol. 337, no. 8738, pp. 403–406, 1991.
- [44] M. D. Johnson, H. H. Lim, T. I. Netoff, A. T. Connolly, N. Johnson, A. Roy, A. Holt, K. O. Lim, J. R. Carey, J. L. Vitek, *et al.*, “Neuromodulation for brain disorders: challenges and opportunities,” *IEEE Transactions on Biomedical Engineering*, vol. 60, no. 3, pp. 610–624, 2013.
- [45] B. M. Eyüboğlu, “Magnetic resonance electrical impedance tomography,” in *Wiley Encyclopedia of Biomedical Engineering* (M. Akay, ed.), vol. 4, pp. 2154–2162, Hoboken: Wiley-Interscience, 2006.
- [46] E. J. Woo and J. K. Seo, “Magnetic resonance electrical impedance tomography (MREIT) for high-resolution conductivity imaging,” *Physiological measurement*, vol. 29, no. 10, p. R1, 2008.
- [47] S. H. Oh, B. I. Lee, E. J. Woo, S. Y. Lee, M. H. Cho, O. Kwon, and J. K. Seo, “Conductivity and current density image reconstruction using harmonic B_z algorithm in magnetic resonance electrical impedance tomography,” *Physics in Medicine & Biology*, vol. 48, no. 19, p. 3101, 2003.
- [48] B. I. Lee, S. H. Oh, E. J. Woo, S. Y. Lee, M. H. Cho, O. Kwon, J. K. Seo, J.-Y. Lee, and W. S. Baek, “Three-dimensional forward solver and its performance analysis for magnetic resonance electrical impedance tomography (MREIT) using recessed electrodes,” *Physics in Medicine & Biology*, vol. 48, no. 13, p. 1971, 2003.
- [49] C. Göksu, K. Scheffler, H. R. Siebner, A. Thielscher, and L. G. Hanson, “The stray magnetic fields in magnetic resonance current density imaging (MR-CDI),” *Physica Medica*, vol. 59, pp. 142–150, 2019.
- [50] C. Park, O. Kwon, E. J. Woo, and J. K. Seo, “Electrical conductivity imaging using gradient B_z decomposition algorithm in magnetic resonance electrical impedance tomography (MREIT),” *IEEE Transactions on Medical Imaging*, vol. 23, no. 3, pp. 388–394, 2004.

- [51] Y. Z. Ider and Ö. Birgül, "Use of the magnetic field generated by the internal distribution of injected currents for electrical impedance tomography (mr-eit)," *Turkish Journal of Electrical Engineering & Computer Sciences*, vol. 6, no. 3, pp. 215–226, 2000.
- [52] O. Kwon, E. J. Woo, J. R. Yoon, and J. K. Seo, "Magnetic resonance electrical impedance tomography (MREIT): simulation study of J-substitution algorithm," *IEEE Transactions on Biomedical Engineering*, vol. 49, no. 2, pp. 160–167, 2002.
- [53] H. S. Khang, B. I. Lee, S. H. Oh, E. J. Woo, S. Y. Lee, M. H. Cho, O. Kwon, J. R. Yoon, and J. K. Seo, "J-substitution algorithm in magnetic resonance electrical impedance tomography (MREIT): phantom experiments for static resistivity images," *IEEE transactions on medical imaging*, vol. 21, no. 6, pp. 695–702, 2002.
- [54] O. Kwon, J. Y. Lee, and J. R. Yoon, "Equipotential line method for magnetic resonance electrical impedance tomography," *Inverse Problems*, vol. 18, no. 4, p. 1089, 2002.
- [55] N. Zhang, "Electrical impedance tomography based on current density imaging," Master's thesis, Dept. Elect. Eng., Univ. of Toronto, Toronto, 1992.
- [56] S. Y. Lee, C. U. Mun, *et al.*, "Impedance tomography using internal current density distribution measured by nuclear magnetic resonance," *Journal of Biomedical Engineering Research*, vol. 15, no. 4, pp. 413–418, 1994.
- [57] Y. Z. Ider and Ö. Birgül, "Use of the magnetic field generated by the internal distribution of injected currents for electrical impedance tomography (MR-EIT)," *Turkish Journal of Electrical Engineering & Computer Sciences*, vol. 6, no. 3, pp. 215–226, 2000.
- [58] Y. Z. Ider, S. Onart, and W. R. Lionheart, "Uniqueness and reconstruction in magnetic resonance-electrical impedance tomography (MR-EIT)," *Physiological measurement*, vol. 24, no. 2, p. 591, 2003.
- [59] M. S. Özdemir, B. M. Eyüboğlu, and O. Özbek, "Equipotential projection-

- based magnetic resonance electrical impedance tomography and experimental realization,” *Physics in Medicine & Biology*, vol. 49, no. 20, p. 4765, 2004.
- [60] J. K. Seo, J.-R. Yoon, E. J. Woo, and O. Kwon, “Reconstruction of conductivity and current density images using only one component of magnetic field measurements,” *IEEE Transactions on Biomedical Engineering*, vol. 50, no. 9, pp. 1121–1124, 2003.
- [61] K. Jeon, A. S. Minhas, Y. T. Kim, W. C. Jeong, H. J. Kim, B. T. Kang, H. M. Park, C.-O. Lee, J. K. Seo, and E. J. Woo, “MREIT conductivity imaging of the postmortem canine abdomen using coreha,” *Physiological measurement*, vol. 30, no. 9, p. 957, 2009.
- [62] H. J. Kim, Y. T. Kim, A. S. Minhas, W. C. Jeong, E. J. Woo, J. K. Seo, and O. J. Kwon, “In vivo high-resolution conductivity imaging of the human leg using MREIT: the first human experiment,” *IEEE transactions on medical imaging*, vol. 28, no. 11, pp. 1681–1687, 2009.
- [63] H. J. Kim, W. C. Jeong, Y. Kim, A. Minhas, T. Lee, C. Lim, H. Park, J. K. Seo, and E. Woo, “In vivo conductivity imaging of canine male pelvis using a 3T MREIT system,” in *Journal of Physics: Conference Series*, vol. 224, p. 012020, IOP Publishing, 2010.
- [64] E. J. Woo, “High-resolution MREIT using low imaging currents,” in *2011 Annual International Conference of the IEEE Engineering in Medicine and Biology Society*, pp. 7025–7028, IEEE, 2011.
- [65] L. A. Geddes and L. E. Baker, “The specific resistance of biological material—a compendium of data for the biomedical engineer and physiologist,” *Medical and biological engineering*, vol. 5, no. 3, pp. 271–293, 1967.
- [66] J. K. Seo, H. C. Pyo, C. Park, O. Kwon, and E. J. Woo, “Image reconstruction of anisotropic conductivity tensor distribution in MREIT: computer simulation study,” *Physics in Medicine & Biology*, vol. 49, no. 18, p. 4371, 2004.
- [67] E. Degirmenci and B. M. Eyuboglu, “Image reconstruction in magnetic resonance conductivity tensor imaging (MRCTI),” *IEEE transactions on medical imaging*, vol. 31, no. 3, pp. 525–532, 2011.

- [68] E. Degirmenci and B. M. Eyuboglu, “Practical realization of magnetic resonance conductivity tensor imaging (MRCTI),” *IEEE transactions on medical imaging*, vol. 32, no. 3, pp. 601–608, 2012.
- [69] O. I. Kwon, W. C. Jeong, S. Z. Sajib, H. J. Kim, and E. J. Woo, “Anisotropic conductivity tensor imaging in MREIT using directional diffusion rate of water molecules,” *Physics in Medicine & Biology*, vol. 59, no. 12, p. 2955, 2014.
- [70] W. Ma, T. P. DeMonte, A. I. Nachman, N. M. Elsaid, and M. L. Joy, “Experimental implementation of a new method of imaging anisotropic electric conductivities,” in *2013 35th Annual International Conference of the IEEE Engineering in Medicine and Biology Society (EMBC)*, pp. 6437–6440, IEEE, 2013.
- [71] D. S. Tuch, V. J. Wedeen, A. M. Dale, J. S. George, and J. W. Belliveau, “Conductivity tensor mapping of the human brain using diffusion tensor MRI,” *Proceedings of the National Academy of Sciences*, vol. 98, no. 20, pp. 11697–11701, 2001.
- [72] M. Sekino, K. Yamaguchi, N. Iriguchi, and S. Ueno, “Conductivity tensor imaging of the brain using diffusion-weighted magnetic resonance imaging,” *Journal of applied physics*, vol. 93, no. 10, pp. 6730–6732, 2003.
- [73] W. C. Jeong, S. Z. Sajib, N. Katoch, H. J. Kim, O. I. Kwon, and E. J. Woo, “Anisotropic conductivity tensor imaging of in vivo canine brain using DT-MREIT,” *IEEE Transactions on Medical Imaging*, vol. 36, no. 1, pp. 124–131, 2016.
- [74] M. Chauhan, A. Indahlastari, A. K. Kasinadhuni, M. Schär, T. H. Mareci, and R. J. Sadleir, “Low-frequency conductivity tensor imaging of the human head in vivo using DT-MREIT: First study,” *IEEE transactions on medical imaging*, vol. 37, no. 4, pp. 966–976, 2017.
- [75] M. Zaitsev, J. Maclaren, and M. Herbst, “Motion artifacts in MRI: a complex problem with many partial solutions,” *Journal of Magnetic Resonance Imaging*, vol. 42, no. 4, pp. 887–901, 2015.

- [76] S. Z. Sajib, O. I. Kwon, H. J. Kim, and E. J. Woo, “Electrodeless conductivity tensor imaging (CTI) using MRI: basic theory and animal experiments,” *Biomedical engineering letters*, vol. 8, no. 3, pp. 273–282, 2018.
- [77] T. Stegemann, M. Heimann, P. Düsterhus, and M. Schulte-Markwort, “Diffusion tensor imaging (DTI) and its importance for exploration of normal or pathological brain development,” *Fortschritte der Neurologie-psychiatrie*, vol. 74, no. 3, pp. 136–148, 2006.
- [78] R. Trivedi, R. K. Rathore, and R. K. Gupta, “Clinical application of diffusion tensor imaging,” *The Indian Journal of Radiology & Imaging*, vol. 18, no. 1, p. 45, 2008.
- [79] M. Balasubramanian, R. V. Mulkern, W. M. Wells, P. Sundaram, and D. B. Orbach, “Magnetic resonance imaging of ionic currents in solution: the effect of magnetohydrodynamic flow,” *Magnetic resonance in medicine*, vol. 74, no. 4, pp. 1145–1155, 2015.
- [80] T. S. Tenforde, “Magnetically induced electric fields and currents in the circulatory system,” *Progress in Biophysics and Molecular Biology*, vol. 87, no. 2-3, pp. 279–288, 2005.
- [81] J. W. Krug and G. Rose, “Magnetohydrodynamic distortions of the ECG in different MR scanner configurations,” in *2011 Computing in Cardiology*, pp. 769–772, IEEE, 2011.
- [82] D. Stüb, J. Roessler, K. O’Brien, C. Hamilton-Craig, and M. Barth, “ECG triggering in ultra-high field cardiovascular MRI,” *Tomography*, vol. 2, no. 3, p. 167, 2016.
- [83] H. H. Eroğlu, M. Sadighi, and B. M. Eyüboğlu, “Magnetohydrodynamic flow imaging of ionic solutions using electrical current injection and MR phase measurements,” *Journal of Magnetic Resonance*, vol. 303, pp. 128–137, 2019.
- [84] A. S. Minhas, M. Chauhan, F. Fu, and R. Sadleir, “Evaluation of magnetohydrodynamic effects in magnetic resonance electrical impedance tomography at ultra-high magnetic fields,” *Magnetic resonance in medicine*, vol. 81, no. 4, pp. 2264–2276, 2019.

- [85] S. Benders, B. F. Gomes, M. Carmo, L. A. Colnago, and B. Blümich, “In-situ MRI velocimetry of the magnetohydrodynamic effect in electrochemical cells,” *Journal of Magnetic Resonance*, vol. 312, p. 106692, 2020.
- [86] V. Denolin, C. Azizieh, and T. Metens, “New insights into the mechanisms of signal formation in rf-spoiled gradient echo sequences,” *Magnetic Resonance in Medicine: An Official Journal of the International Society for Magnetic Resonance in Medicine*, vol. 54, no. 4, pp. 937–954, 2005.
- [87] M. Markl and J. Leupold, “Gradient echo imaging,” *Journal of Magnetic Resonance Imaging*, vol. 35, no. 6, pp. 1274–1289, 2012.
- [88] H. Gudbjartsson and S. Patz, “The rician distribution of noisy MRI data,” *Magnetic resonance in medicine*, vol. 34, no. 6, pp. 910–914, 1995.
- [89] R. Sadleir, S. Grant, S. U. Zhang, B. I. Lee, H. C. Pyo, S. H. Oh, C. Park, E. J. Woo, S. Y. Lee, O. Kwon, *et al.*, “Noise analysis in magnetic resonance electrical impedance tomography at 3 and 11 t field strengths,” *Physiological measurement*, vol. 26, no. 5, p. 875, 2005.
- [90] A. M. El-Sharkawy, M. Schär, P. A. Bottomley, and E. Atalar, “Monitoring and correcting spatio-temporal variations of the MR scanner’s static magnetic field,” *Magnetic resonance materials in Physics, Biology and Medicine*, vol. 19, no. 5, pp. 223–236, 2006.
- [91] P. Blümler, B. Blümich, R. E. Botto, and E. Fukushima, *Spatially resolved magnetic resonance: methods, materials, medicine, biology, rheology, geology, ecology, hardware*. John Wiley & Sons, 2008.
- [92] S. Hidalgo-Tobon, “Theory of gradient coil design methods for magnetic resonance imaging,” *Concepts in Magnetic Resonance Part A*, vol. 36, no. 4, pp. 223–242, 2010.
- [93] L. Zilberti, O. Bottauscio, M. Chiampi, J. Hand, H. S. Lopez, R. Brühl, and S. Crozier, “Numerical prediction of temperature elevation induced around metallic hip prostheses by traditional, split, and uniplanar gradient coils,” *Magnetic resonance in medicine*, vol. 74, no. 1, pp. 272–279, 2015.

- [94] R. Brühl, A. Ihlenfeld, and B. Ittermann, “Gradient heating of bulk metallic implants can be a safety concern in MRI,” *Magnetic resonance in medicine*, vol. 77, no. 5, pp. 1739–1740, 2017.
- [95] H. Graf, G. Steidle, and F. Schick, “Heating of metallic implants and instruments induced by gradient switching in a 1.5-Tesla whole-body unit,” *Journal of Magnetic Resonance Imaging: An Official Journal of the International Society for Magnetic Resonance in Medicine*, vol. 26, no. 5, pp. 1328–1333, 2007.
- [96] J. P. Marques, F. F. Simonis, and A. G. Webb, “Low-field MRI: An MR physics perspective,” *Journal of magnetic resonance imaging*, vol. 49, no. 6, pp. 1528–1542, 2019.
- [97] W. D. Rooney, G. Johnson, X. Li, E. R. Cohen, S.-G. Kim, K. Ugurbil, and C. S. Springer Jr, “Magnetic field and tissue dependencies of human brain longitudinal $1h_2o$ relaxation in vivo,” *Magnetic Resonance in Medicine: An Official Journal of the International Society for Magnetic Resonance in Medicine*, vol. 57, no. 2, pp. 308–318, 2007.
- [98] P. A. Bottomley, T. H. Foster, R. E. Argersinger, and L. M. Pfeifer, “A review of normal tissue hydrogen NMR relaxation times and relaxation mechanisms from 1-100 MHz: dependence on tissue type, NMR frequency, temperature, species, excision, and age,” *Medical physics*, vol. 11, no. 4, pp. 425–448, 1984.
- [99] R. Pohmann, O. Speck, and K. Scheffler, “Signal-to-noise ratio and MR tissue parameters in human brain imaging at 3, 7, and 9.4 tesla using current receive coil arrays,” *Magnetic resonance in medicine*, vol. 75, no. 2, pp. 801–809, 2016.
- [100] M. J. Aminoff, F. Boller, and D. F. Swaab, *Handbook of Clinical Neurology: Basic and Clinical Aspects. The human hypothalamus*, vol. 79. Elsevier, 2003.
- [101] E. Michel, D. Hernandez, and S. Y. Lee, “Electrical conductivity and permittivity maps of brain tissues derived from water content based on T_1 -weighted acquisition,” *Magnetic resonance in medicine*, vol. 77, no. 3, pp. 1094–1103, 2017.

- [102] H. Eroglu, B. Eyüboğlu, and C. Göksu, “Design and implementation of a bipolar current source for MREIT applications,” in *XIII Mediterranean Conference on Medical and Biological Engineering and Computing 2013*, pp. 161–164, Springer, 2014.
- [103] C. Park, B. I. Lee, and O. I. Kwon, “Analysis of recoverable current from one component of magnetic flux density in MREIT and MRCDI,” *Physics in Medicine & Biology*, vol. 52, no. 11, p. 3001, 2007.
- [104] C. Ham, J. Engels, G. Van de Wiel, and A. Machielsen, “Peripheral nerve stimulation during MRI: effects of high gradient amplitudes and switching rates,” *Journal of Magnetic Resonance Imaging*, vol. 7, no. 5, pp. 933–937, 1997.
- [105] E. T. Tan, Y. Hua, E. W. Fiveland, M. E. Vermilyea, J. E. Piel, K. J. Park, V. B. Ho, and T. K. Foo, “Peripheral nerve stimulation limits of a high amplitude and slew rate magnetic field gradient coil for neuroimaging,” *Magnetic Resonance in Medicine*, vol. 83, no. 1, pp. 352–366, 2020.
- [106] W. M. Spees, N. Buhl, P. Sun, J. J. Ackerman, J. J. Neil, and J. R. Garbow, “Quantification and compensation of eddy-current-induced magnetic-field gradients,” *Journal of magnetic resonance*, vol. 212, no. 1, pp. 116–123, 2011.
- [107] O. Bieri, M. Markl, and K. Scheffler, “Analysis and compensation of eddy currents in balanced SSFP,” *Magnetic Resonance in Medicine: An Official Journal of the International Society for Magnetic Resonance in Medicine*, vol. 54, no. 1, pp. 129–137, 2005.
- [108] P. Jezzard and R. S. Balaban, “Correction for geometric distortion in echo planar images from B_0 field variations,” *Magnetic resonance in medicine*, vol. 34, no. 1, pp. 65–73, 1995.
- [109] F. Donato Jr, D. N. Costa, Q. Yuan, N. M. Rofsky, R. E. Lenkinski, and I. Pedrosa, “Geometric distortion in diffusion-weighted MR imaging of the prostate—contributing factors and strategies for improvement,” *Academic radiology*, vol. 21, no. 6, pp. 817–823, 2014.
- [110] G. Barrio-Arranz, R. de Luis-García, A. Tristán-Vega, M. Martín-Fernández, and S. Aja-Fernández, “Impact of MR acquisition parameters on DTI scalar in-

- dexes: a tractography based approach,” *PloS one*, vol. 10, no. 10, p. e0137905, 2015.
- [111] P. Sundgren, Q. Dong, D. Gomez-Hassan, S. Mukherji, P. Maly, and R. Welsh, “Diffusion tensor imaging of the brain: review of clinical applications,” *Neuroradiology*, vol. 46, no. 5, pp. 339–350, 2004.
- [112] E. M. Haacke, R. W. Brown, M. R. Thompson, R. Venkatesan, *et al.*, *Magnetic resonance imaging: physical principles and sequence design*, vol. 82. Wiley-Liss New York:, 1999.
- [113] P. Jezzard and R. S. Balaban, “Correction for geometric distortion in echo planar images from B_0 field variations,” *Magnetic resonance in medicine*, vol. 34, no. 1, pp. 65–73, 1995.
- [114] F. Donato Jr, D. N. Costa, Q. Yuan, N. M. Rofsky, R. E. Lenkinski, and I. Pedrosa, “Geometric distortion in diffusion-weighted MR imaging of the prostate—contributing factors and strategies for improvement,” *Academic radiology*, vol. 21, no. 6, pp. 817–823, 2014.
- [115] J. L. Andersson, S. Skare, and J. Ashburner, “How to correct susceptibility distortions in spin-echo echo-planar images: application to diffusion tensor imaging,” *Neuroimage*, vol. 20, no. 2, pp. 870–888, 2003.
- [116] S. M. Smith, M. Jenkinson, M. W. Woolrich, C. F. Beckmann, T. E. Behrens, H. Johansen-Berg, P. R. Bannister, M. De Luca, I. Drobnjak, D. E. Flitney, *et al.*, “Advances in functional and structural MR image analysis and implementation as fsl,” *Neuroimage*, vol. 23, pp. S208–S219, 2004.
- [117] M. Jenkinson, C. F. Beckmann, T. E. Behrens, M. W. Woolrich, and S. M. Smith, “Fsl,” *Neuroimage*, vol. 62, no. 2, pp. 782–790, 2012.
- [118] B. Sharif and F. Kamalabadi, “Optimal sensor array configuration in remote image formation,” *IEEE transactions on image processing*, vol. 17, no. 2, pp. 155–166, 2008.
- [119] P. C. Hansen, *Discrete inverse problems: insight and algorithms*. SIAM, 2010.

- [120] T. A. Wagner, M. Zahn, A. J. Grodzinsky, and A. Pascual-Leone, “Three-dimensional head model simulation of transcranial magnetic stimulation,” *IEEE Transactions on Biomedical Engineering*, vol. 51, no. 9, pp. 1586–1598, 2004.
- [121] J. L. Mueller and S. Siltanen, *Linear and nonlinear inverse problems with practical applications*. SIAM, 2012.
- [122] COMSOL Multiphysics® v. 5.1. www.comsol.com. COMSOL AB, Stockholm, Sweden.
- [123] C. Gabriel, A. Peyman, and E. H. Grant, “Electrical conductivity of tissue at frequencies below 1 MHz,” *Physics in medicine & biology*, vol. 54, no. 16, p. 4863, 2009.
- [124] D. P. Cistola and M. D. Robinson, “Compact NMR relaxometry of human blood and blood components,” *TrAC Trends in Analytical Chemistry*, vol. 83, pp. 53–64, 2016.
- [125] R. W. Hanks, *Fluid Dynamics (Chemical Engineering)*. Elsevier, 2003.
- [126] M. A. Day, “The no-slip condition of fluid dynamics,” *Erkenntnis*, vol. 33, no. 3, pp. 285–296, 1990.
- [127] A. J. De Crespigny, M. P. Marks, D. R. Enzmann, and M. E. Moseley, “Navigated diffusion imaging of normal and ischemic human brain,” *Magnetic resonance in medicine*, vol. 33, no. 5, pp. 720–728, 1995.
- [128] M. Sadighi, H. H. Eroğlu, and B. M. Eyüboğlu, “Effect of intense utilization of gradients in magnetic resonance current density imaging and its removal,” in *ISMRM & SMRT 27th Annual Meeting & Exhibition*, p. 5068, ISMRM, 2019.
- [129] M. Sadighi, M. Şişman, and B. M. Eyüboğlu, “Optimization of snr and the total acquisition time in MRCDI,” in *ISMRM & SMRT Virtual Conference & Exhibition*, p. 3789, ISMRM, 2021.
- [130] G. J. Stanisz, E. E. Odrobina, J. Pun, M. Escaravage, S. J. Graham, M. J. Bronskill, and R. M. Henkelman, “ T_1 , T_2 relaxation and magnetization transfer in tissue at 3T,” *Magnetic Resonance in Medicine: An Official Journal of*

- the International Society for Magnetic Resonance in Medicine*, vol. 54, no. 3, pp. 507–512, 2005.
- [131] B. J. MacIntosh, S. J. Graham, and P. Eng, “Magnetic resonance imaging to visualize stroke and characterize stroke recovery: a review,” *Frontiers in neurology*, vol. 4, p. 60, 2013.
- [132] P. L. de Sousa, A. Vignaud, S. Fleury, and P. G. Carlier, “Fast monitoring of T_1 , T_2 , and relative proton density (M_0) changes in skeletal muscles using an IR-TrueFISP sequence,” *Journal of Magnetic Resonance Imaging*, vol. 33, no. 4, pp. 921–930, 2011.
- [133] K. Thangavel and E. Ü. SARITAŞ, “Aqueous paramagnetic solutions for MRI phantoms at 3T: A detailed study on relaxivities,” *Turkish Journal of Electrical Engineering & Computer Sciences*, vol. 25, no. 3, pp. 2108–2121, 2017.
- [134] M. Sadighi, M. Şişman, B. C. Açıkgöz, and B. M. Eyüboğlu, “Single current diffusion tensor magnetic resonance electrical impedance tomography: A simulation study,” in *ISMRM & SMRT Virtual Conference & Exhibition*, p. 3233, ISMRM, 2020.
- [135] M. Sadighi, M. Şişman, B. C. Açıkgöz, and B. M. Eyüboğlu, “Experimental realization of single current diffusion tensor magnetic resonance electrical impedance tomography,” in *ISMRM & SMRT Virtual Conference & Exhibition*, p. 0179, ISMRM, 2020.
- [136] S. Z. Sajib, N. Katoch, H. J. Kim, O. I. Kwon, and E. J. Woo, “Software toolbox for low-frequency conductivity and current density imaging using MRI,” *IEEE Transactions on Biomedical Engineering*, vol. 64, no. 11, pp. 2505–2514, 2017.
- [137] M. Sadighi, M. Şişman, and B. M. Eyüboğlu, “Multi-physics multi-contrast magnetic resonance imaging,” in *ISMRM & SMRT Virtual Conference & Exhibition*, p. 1239, ISMRM, 2021.
- [138] M. Chauhan, R. Vidya Shankar, N. Ashok Kumar, V. D. Kodibagkar, and R. Sadleir, “Multishot echo-planar MREIT for fast imaging of conductiv-

- ity, current density, and electric field distributions,” *Magnetic resonance in medicine*, vol. 79, no. 1, pp. 71–82, 2018.
- [139] J. Y. Chiou, C. B. Ahn, L. T. Muftuler, and O. Nalcioglu, “A simple simultaneous geometric and intensity correction method for echo-planar imaging by EPI-based phase modulation,” *IEEE transactions on medical imaging*, vol. 22, no. 2, pp. 200–205, 2003.
- [140] N. k. Chen and A. M. Wyrwicz, “Removal of EPI nyquist ghost artifacts with two-dimensional phase correction,” *Magnetic Resonance in Medicine: An Official Journal of the International Society for Magnetic Resonance in Medicine*, vol. 51, no. 6, pp. 1247–1253, 2004.
- [141] X. Hu and T. H. Le, “Artifact reduction in EPI with phase-encoded reference scan,” *Magnetic resonance in medicine*, vol. 36, no. 1, pp. 166–171, 1996.

CURRICULUM VITAE

PERSONAL INFORMATION

Surname, Name: Mehdi Sadighi

Date and Place of Birth: May 29 1984, Tehran, Iran

Marital Status: Single

Phone: +90 545 214 1116

Email: mehdi.sadighi@metu.edu.tr

Gmail: sadighi.mehdi@gmail.com

EDUCATION

Degree	Institution	Year of Graduation
PhD	METU Electrical and Electronics Engineering	2021
MS	METU Electrical and Electronics Engineering	2014
BS	Tabriz Azad University Electrical and Electronics Engineering	2009

PUBLICATIONS

Journal Articles

1. M. Sadighi, M. Şişman, B. C. Açıkgöz, H. H. Eroğlu, B. M. Eyüboğlu, "Low-Frequency Conductivity Tensor Imaging with a Single Current Injection Using DT-MREIT," *Physics in Medicine & Biology*, vol. 66, no. 5, 055011, 2021.
2. H. H. Eroğlu, M. Sadighi, B. M. Eyüboğlu, "Magnetohydrodynamic flow imaging of ionic solutions using electrical current injection and MR phase measurements," *Journal of Magnetic Resonance*, vol. 303, pp. 128-137, 2019.
3. H. H. Eroğlu, M. Sadighi, B. M. Eyüboğlu, "Induced Current Magnetic Resonance Electrical Conductivity Imaging with Oscillating Gradients," *Transactions on Medical Imaging*, vol. 37, no. 7, pp. 1606-1617, 2018.

Conference Papers

1. M. Sadighi, M. Şişman, B. M. Eyüboğlu, "Multi-Physics Multi-Contrast Magnetic Resonance Imaging," in *ISMRM & SMRT Virtual Conference & Exhibition*, #1239, ISMRM, 2021.
2. M. Sadighi, M. Şişman, B. M. Eyüboğlu, "Optimization of SNR and the total acquisition time of the current-induced magnetic flux density B_z in MRCDI," in *ISMRM & SMRT Virtual Conference & Exhibition*, #3789, ISMRM, 2021.
3. M. Şişman, M. Sadighi, B. M. Eyüboğlu, "Simultaneous Magnetic Resonance Magnetohydrodynamic Flow Velocity and Diffusion Tensor Imaging," in *ISMRM & SMRT Virtual Conference & Exhibition*, #1257, ISMRM, 2021.
4. M. Şişman, M. Sadighi, H. H. Eroğlu, B. M. Eyüboğlu, "Experimental Evaluation of Spin Echo based Magnetic Resonance Magnetohydrodynamic Flow Velocimetry," in *ISMRM & SMRT Virtual Conference & Exhibition*, #1256, ISMRM, 2021.
5. M. Sadighi, M. Şişman, B. C. Açıkgoz, B. M. Eyüboğlu, "Single Current Diffusion Tensor Magnetic Resonance Electrical Impedance Tomography: A Simulation Study," in *ISMRM & SMRT Virtual Conference & Exhibition*, #3233, ISMRM, 2020.
6. M. Sadighi, M. Şişman, B. C. Açıkgoz, B. M. Eyüboğlu, "Experimental Realization of Single Current Diffusion Tensor Magnetic Resonance Electrical Impedance Tomography," in *ISMRM & SMRT Virtual Conference & Exhibition*, #0179, ISMRM, 2020.
7. M. Sadighi, H. H. Eroğlu, B. M. Eyüboğlu, "Effect of Intense Utilization of Gradients in Magnetic Resonance Current Density Imaging and its Removal," in *27th Annual Meeting of the International Society for Magnetic Resonance in Medicine*, #5068, ISMRM, 2019, Montreal, Canada.
8. H. H. Eroğlu, M. Sadighi, B. M. Eyüboğlu, "Magnetohydrodynamic Flow Imaging Using Spin-Echo Pulse Sequence," in *27th Signal Processing and Communications Applications Conference (SIU)*, IEEE, 2019, pp. 1-4, Sivas, Turkey.
9. M. Sadighi, S. F. Oktem, B. M. Eyüboğlu, "Diffusion Tensor Magnetic Resonance

Electrical Impedance Tomography versus Magnetic Resonance Conductivity Tensor Imaging," in *26th joint annual meeting ISMRM & ESMRMB*, #5086, ISMRM, 2018, Paris, France.

10. H.H. Eroğlu, M. Sadighi, and B.M. Eyüboğlu " Low frequency magnetic resonance conductivity imaging by means of oscillating gradient fields." in *26th joint annual meeting ISMRM & ESMRMB*, 2018, Paris, France.

11. K. Sümser, N. Naji, M. Sadighi, H. H. Eroğlu, B. M. Eyüboğlu, "MRI-SPAMM Based Magnetic Resonance Electrical Impedance Tomography," in *24th Annual Meeting of the International Society for Magnetic Resonance in Medicine*, #1940, ISMRM, 2016, Singapore.

12. N. Naji, H. H. Eroğlu, K. Sümser, M. Sadighi, B. M. Eyüboğlu, "Enhancing Induced Current Magnetic Resonance Electrical Impedance Tomography (ICMREIT) Image Reconstruction," in *Proc. 12th IASTED Int. Conf. Biomed. Eng. BIOMED*, pp. 832-834, 2016, Innsbruck.

13. H. H. Eroğlu, M. Sadighi, K. Sümser, N. Naji, B. M. Eyüboğlu, "Experimental Realization of Induced Current Magnetic Resonance Current Density Imaging," in *Proc. IEEE Int. Conf. EMBC*, pp. 614-617, 2015, Milano.

14. C. Göksu, M. Sadighi, H. H. Eroğlu, B. M. Eyüboğlu, "Realization of Magnetic Resonance Current Density Imaging at 3 Tesla," in *Proc. IEEE Int. Conf. EMBC*, pp. 1115-1118, 2014, Chicago.

15. M. Sadighi, C. Göksu, and M. Eyüboğlu, "J-based Magnetic Resonance Conductivity Tensor Imaging (MRCTI) at 3 T," in *Proc. IEEE Int. Conf. EMBC*, pp. 1139-1142, 2014, Chicago.

PATENT APPLICATIONS

1. B. M. Eyübođlu, H. H. Erođlu, M. Sadighi, "An induced current magnetic resonance electrical impedance tomography (ICMREIT) pulse sequence based on monopolar slice selection gradient pulses." European Patent Office (EPO) Application, application no. EP18163817.2, 2018.
2. B. M. Eyübođlu, H. H. Erođlu, M. Sadighi, "Induced current magnetic resonance electrical impedance tomography (ICMREIT) pulse sequence based on monopolar slice selective gradient pulses." Turkish Patent Institute (TPE) Application, application no. P17/0601, 2017.
3. B. M. Eyübođlu, H. H. Erođlu, M. Sadighi, K. Sümser, N. Naji, "Induced current magnetic resonance electrical impedance tomography (ICMREIT) pulse sequence based on bipolar slice selective gradient pulses." Turkish Patent Institute (TPE) Application, application no. P16/0494, 2016.
4. B. M. Eyübođlu, K. Sümser, H. H. Erođlu, M. Sadighi, N. Naji, "Spin tagged magnetic resonance current density and electrical impedance imaging pulse sequence." Turkish Patent Institute (TPE), patent no. TR 2015 13995 B, 2015.

AWARDS

Magna Cum Laude Merit Award at the 2020 ISMRM & SMRT Virtual Conference & Exhibition, August 2020.

GRANTS

Scholarship: Simultaneous Magnetic Resonance Diffusion and Conductivity Tensor Imaging, 116E157, The Scientific and Technological Research Council of Turkey (TÜBİTAK).

Scholarship: Induced Current Magnetic Resonance Electrical Impedance Tomography (ICMREIT), 113E979, The Scientific and Technological Research Council of Turkey (TÜBİTAK).

Scholarship: Design and Implement an MRI Compatible Current Source, The Scientific and Technological Research Council of Turkey (TÜBİTAK).

FOREIGN LANGUAGES

English: Proficient

Turkish: Fluent

Persian: Native

COMPUTER SKILLS:

- Programming Language: C++
- Scientific Languages and Tools: MATLAB, COMSOL Multiphysics, IDEA (Integrated Development Environment for Applications), FSL (FMRIB Software Library)